12-2017

A Wide Area Hierarchical Voltage Control for Systems with High Wind Penetration and an HVDC Overlay

Yidan Lu
University of Tennessee, Knoxville, ylu16@vols.utk.edu

To the Graduate Council:

I am submitting herewith a dissertation written by Yidan Lu entitled "A Wide Area Hierarchical Voltage Control for Systems with High Wind Penetration and an HVDC Overlay." I have examined the final electronic copy of this dissertation for form and content and recommend that it be accepted in partial fulfillment of the requirements for the degree of Doctor of Philosophy, with a major in Electrical Engineering.

Kevin Tomsovic, Major Professor

We have read this dissertation and recommend its acceptance:

Yilu Liu, Fangxing Li, Suzanne Lenhart

Accepted for the Council:
Carolyn R. Hodges

Vice Provost and Dean of the Graduate School

(Original signatures are on file with official student records.)

A Wide Area Hierarchical Voltage Control for Systems with High Wind Penetration and an HVDC Overlay

A Dissertation Presented for the

Doctor of Philosophy

Degree

The University of Tennessee, Knoxville

Yidan Lu

December 2017

Acknowledgements

I would like to express my greatest gratitude to my major supervisor Dr. Kevin Tomsovic for all the guidance and support he offered to me during my PhD study. He has not only supervised my study and research but also encouraged the improvement of my personality. I would never have made this achievement without his contribution.

Meanwhile, I would like to show appreciation to my committee members: Dr. Yilu Liu and Dr. Fangxing (Fran) Li and Dr. Suzanne Lenhart, who have profoundly participated in my 6-year PhD life and provided me with the best insights on my research topics. Their advice on my dissertation has greatly helped improving its quality and given me many enlightening ideas for future research work.

Then, I need to thank my parents for their precious support. They are the first ones who inspired my passion on pursuing an advanced degree in power system and without them; I would not have the courage to overcome the hardship on the way.

Last but not the least, I would like to say thank you to my then-companion Dr. Kumaraguru Prabakar, who has helped me all the way through the tedious formatting procedure of PhD dissertation. Though our paths have inevitably parted, he would always remain a good friend of mine.

Abstract

The modern power grid is undergoing a dramatic revolution. On the generation side, renewable resources are replacing fossil fuel in powering the system. On the transmission side, an AC-DC hybrid network has become increasingly popular to help reduce the transportation cost of electricity. Wind power, as one of the environmental friendly renewable resources, has taken a larger and larger share of the generation market. Due to the remote locations of wind plants, an HVDC overlay turns out to be attractive for transporting wind energy due to its superiority in long distance transmission of electricity.

While reducing environmental concern, the increasing utilization of wind energy forces the power system to operate under a tighter operating margin. The limited reactive capability of wind turbines is insufficient to provide adequate voltage support under stressed system conditions. Moreover, the volatility of wind further aggravates the problem as it brings uncertainty to the available reactive resources and can cause undesirable voltage behavior in the system. The power electronics of the HVDC overlay may also destabilize the gird under abnormal voltage conditions. Such limitations of wind generation have undermined system security and made the power grid more vulnerable to disturbances.

This dissertation proposes a Hierarchical Voltage Control (HVC) methodology to optimize the reactive reserve of a power system with high levels of wind penetration. The proposed control architecture consists of three layers. A tertiary Optimal Power Flow computes references for pilot bus voltages. Secondary voltage scheduling adjusts primary control variables to achieve the desired set points. The three levels of the proposed HVC scheme coordinate to optimize the voltage profile of the system and enhance system security. The proposed HVC is tested on an equivalent Western Electricity Coordinated Council (WECC) system modified by a multi-terminal HVDC overlay. The effectiveness of the proposed HVC is validated under a wide range of operating conditions. The capability to manage a future AC/DC hybrid network is studied to allow even higher levels of wind.

Table of Contents

List of Tables

List of Figures

1. Introduction

The modern power grid is undergoing dramatic revolutions. On the generation side, generators powered by renewable resources are constantly replacing conventional thermal units due to growing concerns of environmental pollution with fossil fuels. Wind, as a favored renewable resource, is taking a larger and larger share of the generation portfolio. Meanwhile, new development of power conversion equipment has eased deployment of DC transmissions. The DC links built in parallel with the AC transmission lines are evolving into an overlay structure for transportation of renewable energy.

The participation of HVDC overlay and wind generation into the already meshed AC transmission grid can jeopardize power system stability and security and subject voltage control to deficiency of VAR resources, uncertainty of the supply end, interference from DC converters and increased transient voltage sags. Thus, new wide area voltage control strategies considering the impact from more high levels, say more than 20%, of wind and HVDC overlay transmission has grown in significance.

1.1 Background of Wind Energy

For two millennia, wind powered machines have ground grain and pumped water. The utilization of wind resources for production of electricity started around 1887, when the first windmill is built to power the lighting of Prof. James Blyth's holiday cottage [1]. With development of energy transmission system through the 20th century, the infrastructure for wind develops from small stations suitable for farms or residence to large utility-scale power plants for grid interconnection.

1.1.1 Wind Power Potential

Today, wind energy is favored as a major renewable alternative for thermal generations as it is widely distributed and rich in resources. Generated via flows of air initiated by uneven solar heating, wind energy is available in most countries around the world. Fig. 1.1 shows the global wind speed distribution at the height of 80m, which is close to the average hub height (82.4m) of the wind turbines installed in US during 2014 [2].

A survey completed by a group of Harvard researchers in 2009 indicates that an annual supply of energy equals to 840 PWh can be harvested by a globally distributed array of onshore wind turbines with capacity factor (CF) higher than 20% [3]. A further investigation using NREL data suggested that the US alone has an average onshore wind resource potential around 10,400 GW [4]. This is equivalent to an energy annual supply of 91 PWh. Considering the 2013 U.S. annual electricity consumption as 3,868 TWh [5], full

utilization of the wind resource potential would mean generation of electric power equal to at least 23 times the 2013 annual electricity consumption.

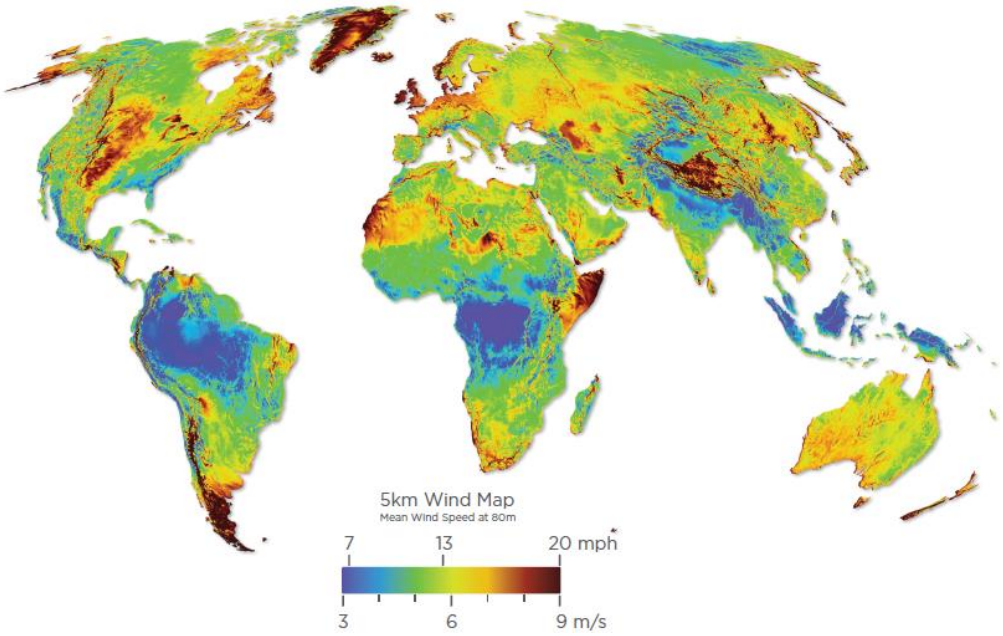

Fig. 1.1 Wind Speed Distribution Map

Higher utilization of wind energy would undoubtedly reduce CO_2 emission and suppress greenhouse effects. Moreover, with the 20% wind energy scenario planned by the Department of Energy (DOE) to be realized by 2030 [6], wind energy is highly encouraged and the rise in wind penetration in has become and unavoidable.

The sizes and numbers of wind farms grew rapidly with new technologies in late 20^{th} century. By the end of 2015, the global cumulative installed wind capacity has reached 432.5 GW as displayed in Fig. 1.2 [7]. Out of all countries with wind capacity installation, China and U.S. ranked the first two with 145.1 GW and 74.5 GW in total installed capacity, respectively [8]. In the U.S., the wind capacity continues to increase [9]. However, with unsatisfactory efficiency increases and increase in customer demand at the same time, the current wind penetration in the U.S remains below 5% [10], far from the goals issued by DOE aiming at 20% wind penetration by year 2030. The reactive power impact due to wind unit characteristics also plays a big role in retarding the growth in wind energy utilization by jeopardizing the overall voltage stability and security. Therefore, a wide area voltage control scheme to alleviate those impacts will be necessary to boost the participation of wind energy in the generation portfolio.

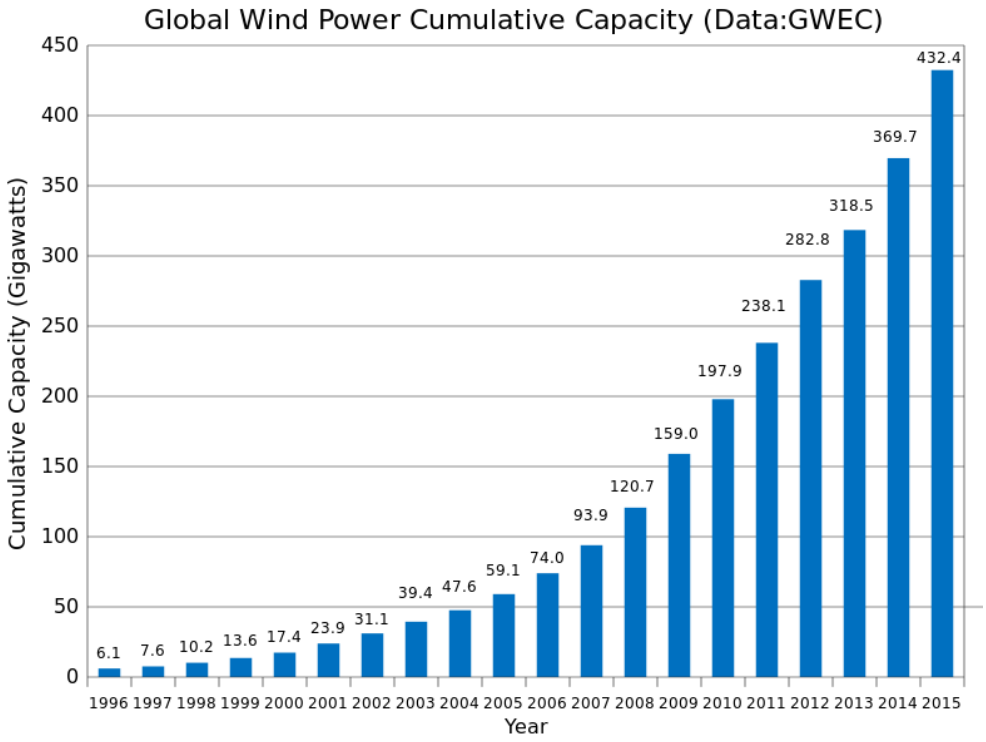

Fig. 1.2 Global Wind Power Cumulative Capacity

1.1.2 Infrastructure of Current Wind Utilization

Many different types of wind turbines have been deployed to harness wind energy. The earliest fixed speed turbines were introduced due to robustness in operation and cost-efficiency for mass production. Later on, these were gradually replaced by variable speed turbines to enable a higher rate of energy capture as the variable speed turbines can operate under a wider range of wind speeds [11]. Depending on the need for operation flexibility, these wind turbines can be connected to the grid via a partial or a full-scale power converter. The full scale converter can perform smooth grid connection over the entire speed range; however, incur higher costs and higher loss in the power electronics since full ratings of the rotating machine are passing through the converter [12].

Today, the Doubly Fed Induction Generator (DFIG) with a partial scale power converter holds over 60% of market share [13] due to its overall satisfactory performances in both power capture and cost efficiency. A multi-stage gearbox is equipped with the DFIG to compensate the differences between its speed range and a common turbine. As the partial scale converter is highly subject to overcurrent under grid disturbances, crowbar protection is enabled to short circuit rotor current during grid disturbance to ensure fault ride-though capability of a DFIG [14]. Fig. 1.3 shows the structure of a DFIG based wind

turbine. Hundreds of such wind turbines are aggregated into wind farms and then interconnected into the transmission grid.

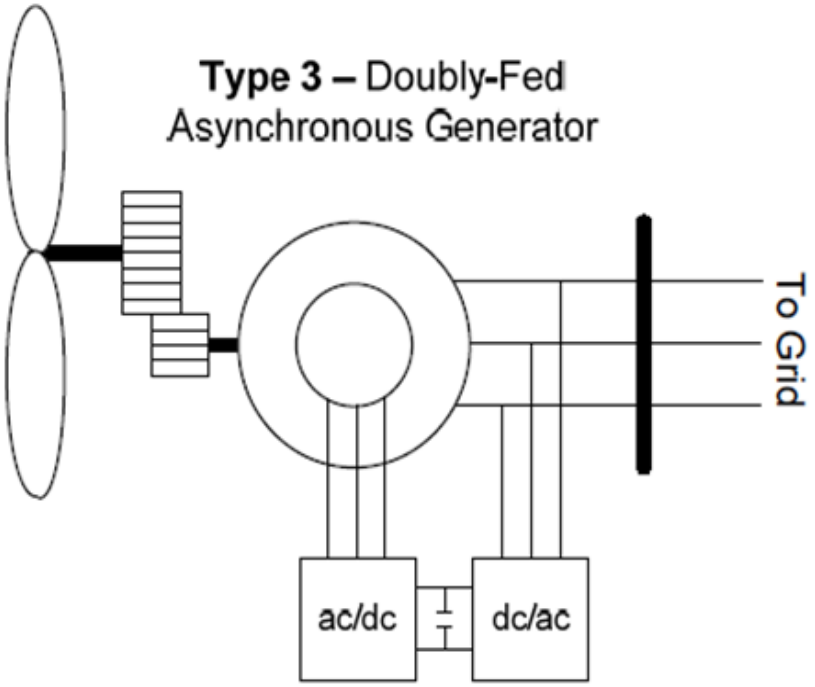

Fig. 1.3 DFIG Wind Turbine Structure

The AC-DC converters shown in the graph partially decouples wind turbines from the grid and therefore reduces the total inertia of power grid [15]. This can amplify grid frequency instability phenomena [16]. Accounting for the reactive capability of DFIG, the power electronics typically allow a power factor of 0.95 lagging to 0.90 leading [12]. However, the grid order issued by FERC [17] requires most of the DFIG aggregated wind farms to have a power factor maintained within leading/lagging 0.95 before grid connection.

The above device characteristics have contributed to various issues for systems with high numbers of wind units, especially when more than 5% of conventional generation is replaced by wind power. These issues include reduced reserve in dynamic VAR and poor damping performance in inter-area oscillations. This can affect power system security and raise the requirements for more robust and intelligent wide area voltage control strategies that can assess and enhance the performance of power system in real time.

1.2 Background of High Voltage Direct Current (HVDC) Utilization

Since the first commercial installation of High Voltage Direct Current (HVDC) to connect the island of Gotland to the Swedish mainland in 1954[18], the significance of HVDC lines and cables has been growing for the bulk transmission system. Taking advantage of the superiorities in energy transfer efficiency, operational adaptability and control flexibility, HVDC is widely applied for long distance power transportation [19], interconnection of asynchronous power grids and coordinated control to enhance system damping performances [20, 21]. With 30-40% lower power loss compared with AC lines at the same voltage levels [20], the application of HVDC has been moved from regional parallel implementation to international overlays. The interactions between HVDC and wide area system controls are inevitable and must be considered when deploying control strategies. Fig. 1.4 shows the typical cost comparison curve between the AC and DC transmissions with respect to transmission distance [21].

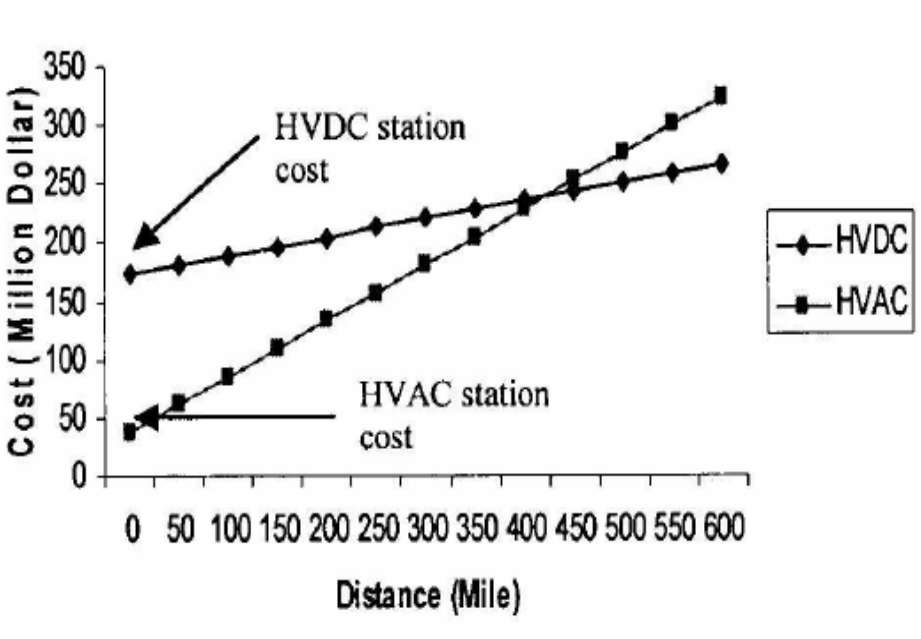

Fig. 1.4 HVDC and HVAC Transmission System Cost Comparison

1.2.1 Architecture of HVDC Transmission

HVDC consists of the power conversion system and DC conductors. There are basically two types of HVDC configurations: the monopolar type with only one conductor and earth or metal used for current path return; the bipolar type where two conductors are installed for completion of the current path. Fig. 1.5 illustrates the basic configurations of the two types of the HVDC.

The length of conductor can be thousands of kilometers for long distance DC transmission or as short as several meters for back-to-back HVDC application. For any of the HVDC configurations, electrical power is changed from AC to DC in the rectifier and from DC to AC in the inverter.

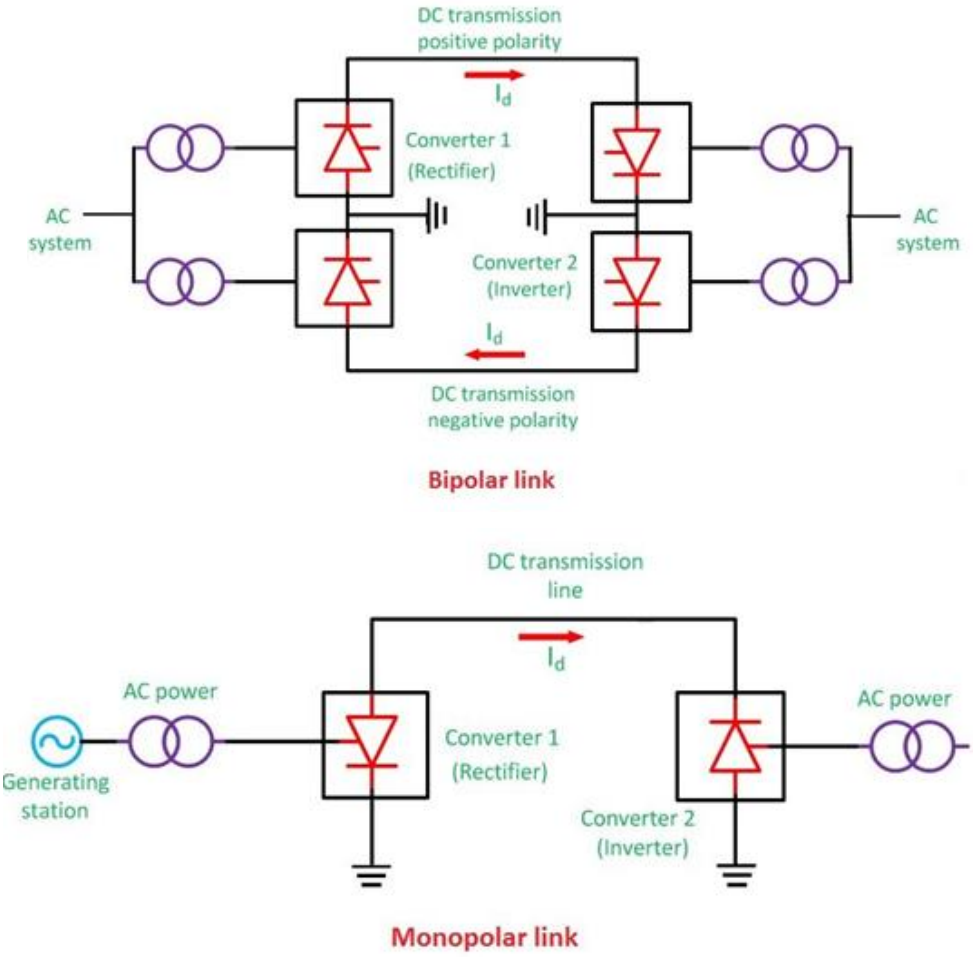

Fig. 1.5 Two Types of HVDC configurations

With developments in power electronics and material science, revolutions in HVDC converters have taken place to enhance the overall functionality of this architecture. The elements in power converters have evolved from mercury arc valves to thyristor switches. Compared with the mercury arc valve, the thyristor provides predictable performance with higher degree of confidence and serves as a key factor for the general acceptance of Lines-commutated Converters (LCC/CSC) HVDC in power transmission [24]. The economic advantages of HVDC in long distance and high rated power transportation are broadly utilized to transfer renewable energies from distant locations to load centers.

In order to meet the need for growing interactions among multiple suppliers and end users, the multi-terminal HVDC structure [22] as shown in Fig. 1.6 [23, 24] has recently been developed. This structure lays the foundation for construction of meshed HVDC overlay grids and greater flexibility and reliable operation of HVDC.

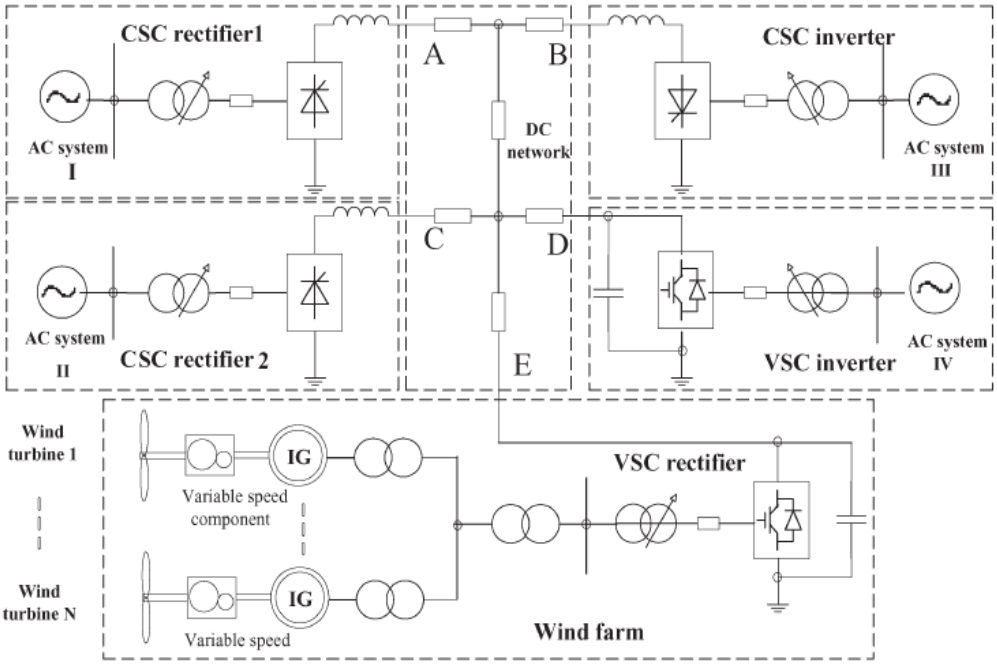

Fig. 1.6 4-terminal 800kV HVDC Configuration

1.2.2 Application of HVDC Transmission

During the 60 years since the first commercial deployment of HVDC scheme, great advances in HVDC technologies and economic opportunities in HVDC have been achieved. Today, DC transmission is functioning in parallel with AC transmission to mitigate flow congestions. The Pacific intertie, for example, transports over 3100 MW of power from the Pacific Northwest to California through an 855-mile long DC link [28], greatly relieving the stress and providing security margin on the three AC lines that form the California to Oregon Intertie (COI).

DC transmission is also used in a back to back connection form to link systems operated in different frequencies or asynchronously. The primary systems (WECC, EI, and ERCOT) of the U.S. power grid are interconnected with back-to-back HVDC for small power transfers. Those back to back HVDC connections have enabled energy transfer among three different regions of the North America Power Grid while enhanced the strength of the system to stand against large disturbances. By the end of 2014, the multi-

terminal HVDC (MTDC) has only a few field applications outside of the four terminal bipolar layouts in WECC Pacific Intertie [25] and Canada Nelson River [26] as listed in Table 1.1.

Table 1.1 List of Current Multi-terminal HVDC Field Applications

Name	Commission Year	Location	Terminal Number	DC Voltage Level	Rated Power
Sardinia–mainland Italy link [27]	1987	Italy	3	±200KV	200MW
Hydro Quebec-New England Transmission [28]	1992	Canada-United States	5	±500KV	2250MW
Shin-Shinano 3-terminal HVDC [29]	2000	Japan	3	±10.6KV	153MW
Nan'ao HVDC [30]	2013	China	3	±160KV	200MW
Zhoushan HVDC [31]	2014	China	5	±200KV	1000MW
South-West Link [32]	2014	Sweden	3	±300KV	1440MW
Tres Amigas Superstation HVDC [33]	2016	United States	3	±345KV	5000MW
North East- Agra Multi-terminal UHVDC Links [34]	2016	India	4	±800KV	6000MW

More multi-terminal HVDC projects are still in planned for future regional and international deployment [35-37]. While the previously discussed characteristics of traditional HVDC [38] has gained general acceptance on the positive impacts for grid performance, the wide area multi-terminal HVDC overlay structure to accommodate renewable energy expansion in future grid has been planned by multiple organizations [39]. Research on interaction and coordination between HVDC overlay and wide area voltage control hold great significance, as the impact analysis and possible remedies are necessary before the commissioned service of a meshed HVDC overlay grid. This dissertation will explore the influence of

HVDC overlay on the effectiveness of a proposed wide area voltage control and discuss approaches to make use of the HVDC characteristics to enhance the performance of the voltage control strategy.

1.3 Overview of General Wide Area Voltage Control

Wide area voltage control first appeared in the secondary voltage regulation scheme in France [40], where a three level hierarchical structure was developed. The fast and random variations were compensated by the local primary and automatic actions in the generation Automatic Voltage Regulator (AVR). Then the slow variations were picked up by a secondary (regional level) and tertiary (national level) regulations [41]. This hierarchical structure has passed along the history and been applied to conventional power systems to optimize reactive distribution and increase system loadability to avoid voltage collapse [42].

1.3.1 The Hierarchical Architecture of Wide Area Voltage Control

Wide area voltage control is often set up as a hierarchical structure and may contain two or three levels. For most of power systems, a tertiary level is included for nationwide optimal reactive power dispatch as illustrated in Fig. 1.7 [43].

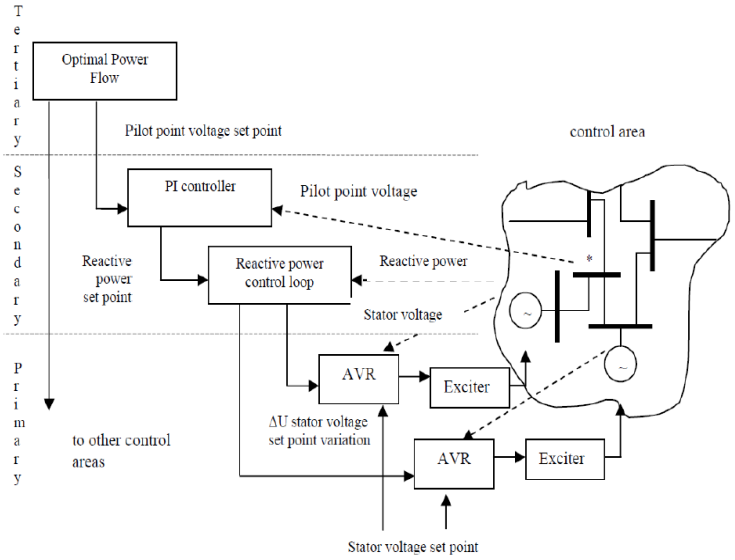

Fig. 1.7 Hierarchical Structure of Wide Area Voltage Control

In this control scheme, the system is divided into different control areas, and control actions are performed to regulate the voltage of one particular point in each area. This point, with ability to represent the voltage evolutions throughout the area is referred to as the pilot bus [44]. The pilot bus is usually located

at the most central position with respect to all controlling nodes in that area [45]. However, with the increasingly meshed character of power systems, coupling between neighboring control areas are inevitable and coordination among different control areas need to be realized [46]. Fig 1.8 shows the general wide area control strategy [47].

The tertiary level procedure can be automatically completed within one hour. At this level, the voltage control is treated in a static and centralized fashion where OPF algorithms are used to manage the reactive flows across the entire system. This procedure calculates the pilot bus voltages and references other control variables for regulation at the secondary level.

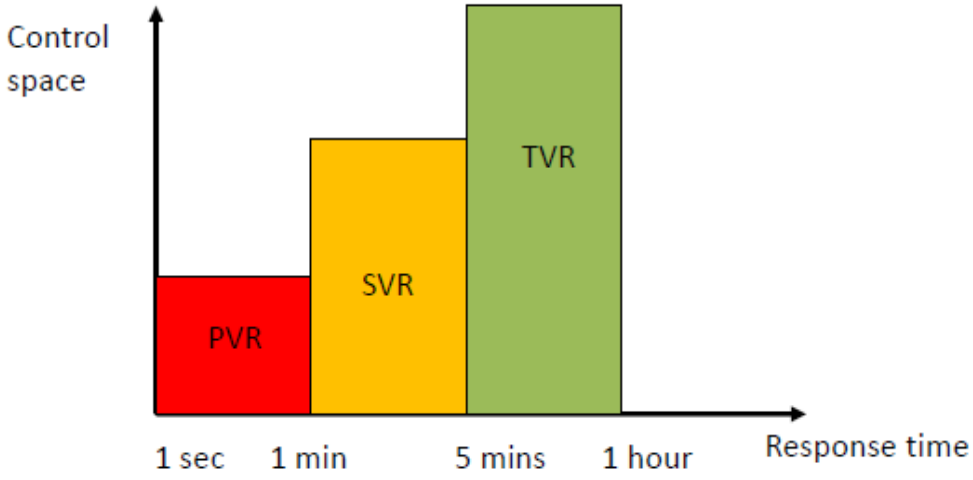

Fig. 1.8 Response Time and Responsible Region for each Control

Secondary level regulation is often performed at an interval of several minutes. At this level, the reactive outputs of generators within each area are adjusted to maintain the voltages on the pilot buses. Other controllable variables, such as, tie line flows and inter-area exchanges can be included to manage the interactions among each area. The desired reactive power output for each unit is calculated at this level and the set-points on unit stator voltage variance will be sent to primary controls. The secondary level control procedure is carried out with only regional information. Without burdening the central processor and system operator, the secondary level control can respond quickly to dynamic phenomena and maintain the system at a desired operating condition.

The primary level control responds to signals from the upper levels within seconds. Mainly consisting of the generator AVRs, the primary level control maintains the generator stator voltages at the desired value according to command from the secondary level. Control actions at this level are completed within each power station.

The traditional wide area voltage control has successfully improved stability margin under static constraints in conventional power systems; however, with increased participation of the renewable generation and HVDC transmission as well as growth in system loading, the traditional wide area voltage control face challenges. The replacement of large portions of conventional generators by DFIG units drains VAR resources and the intermittent reactive outputs induce additional variation to the secondary and primary controls. Growing system loading further exhausts system VAR reserves and can weaken ability to withstand disturbances. The above changes in the power system have made the current wide area voltage control inadequate to adapt to the security requirement under massive wind integration. Moreover, the coordination with DC transmission must be involved for future deployment of wide area voltage control.

1.3.2 Wide Area Voltage Control in Future Power Grid

With deployment of a full-topology node-breaker model in the control center and a high-frequency solution of state estimation simplifies system monitoring, there remain issues to address for applying HVC in future power grid.

1) Reactive deficiency and uncertainty from high wind penetration

Due to the limitations of DFIG [48, 49] and the grid order requirements [17], the reactive capability in systems with high wind penetration is undermined. This can lead to insufficient VAR supply under disturbances and contributes to voltage and frequency sags that trigger unwanted relay actions. The variability in wind power further brings uncertainty in reactive outputs from wind farms. As increases in wind power participation in the generation market, the deficiency and unpredictability of reactive resources becomes more of a concern and regulations on conventional units are insufficient to compensate the reactive shortages. Therefore, the future wide area voltage control scheme needs to encourage wind farm participation in system wide reactive management.

2) Dynamic constraints for online security analysis

Based on recommendations from North America Electric Reliability Council (NERC) for improving system situation awareness [50], online Dynamic Security Assessment (DSA) tools are deployed to evaluate system robustness against N-1 disturbances. This has laid the foundation and raised requirements for wide area voltage control to improve system security in real-time. Therefore, the Western Electricity Coordination Council (WECC) issued planning standards concerning system transient behaviors and post contingency voltage stability [51, 52] are to be coordinated with the tertiary OPF for future wide area voltage control.

3) Coordination with HVDC overlay

With DFIG units gradually replacing conventional generators, the total system inertia has been reduced. Such systems are subject to faster frequency dynamics and larger frequency deviation under disturbances

[16]. With increasing in wind penetration and system loading, the reduction in inertia can amplify oscillatory instability [53]. Adoption of damping controllers [54] and multi-band Power System Stabilizers (PSS) [55, 56] has been proved capable for current power system with less than 5% of wind penetration. At levels of more than 20% wind in the near future, such measures appear not to be adequate. The advantages of HVDC transmission can be utilized to provide extra damping for stressed systems with high wind generation. With multiple projects for HVDC overlay [39] on-going, it is important to study the coordination between HVDC and wide area voltage control and explore approaches to fully utilize the DC transmissions for system security.

1.4 Overview of Dissertation

1.4.1 Innovations

In order to address above requirement for future wide area voltage control, a wide area voltage control scheme is proposed in the dissertation. The main innovations include:

1) Data-driven formulation of tertiary OPF

With the need to restore capacity utilization on the critical WECC path, the OPF objective is to maximize the security margin. The security margin here is represented by the difference between COI base flow and transfer limit. The WECC planning standards concerning the most severe transient violations are translated to dynamic constraints in the tertiary regulation procedure. Numerical simulations are processed to archive data to allow pattern recognition of system transient behaviors and the COI transfer limit with respect to load flow solutions. The formulation is based on pattern recognition using the system variables to approximate the OPF objective and constraints. This is the first time where data based pattern recognition is used for wide area voltage control and allows online DSA. Archived State Estimation (SE) solutions and stability limit analysis results can be directly fed into the data for the proposed control.

2) Revised secondary control loop

The hierarchical architecture of the traditional wide area voltage control is preserved in the dissertation. However, in order to accommodate to today's highly meshed power system where regional reactive power control is subject to interactions with other areas, we added an additional loop to estimate the COI transfer limit at each cycle of the regional dispatch. In this loop, the estimated transfer limit will be calculated using SE solutions of voltages and the difference with the reference will be minimized during the regional dispatch. In this way, coordination among different control areas is realized and the proposed control is able to take action to support inter-area exchanges of the system. Since full-topology operational models supporting high frequency SE solutions are now deployed in North American power grids [57], there should be no additional communication requirements or model upgrades for the tertiary control center in the field

application of the proposed HVC. Fig. 1.9 shows the logical architecture of the wide area voltage control proposed in this dissertation.

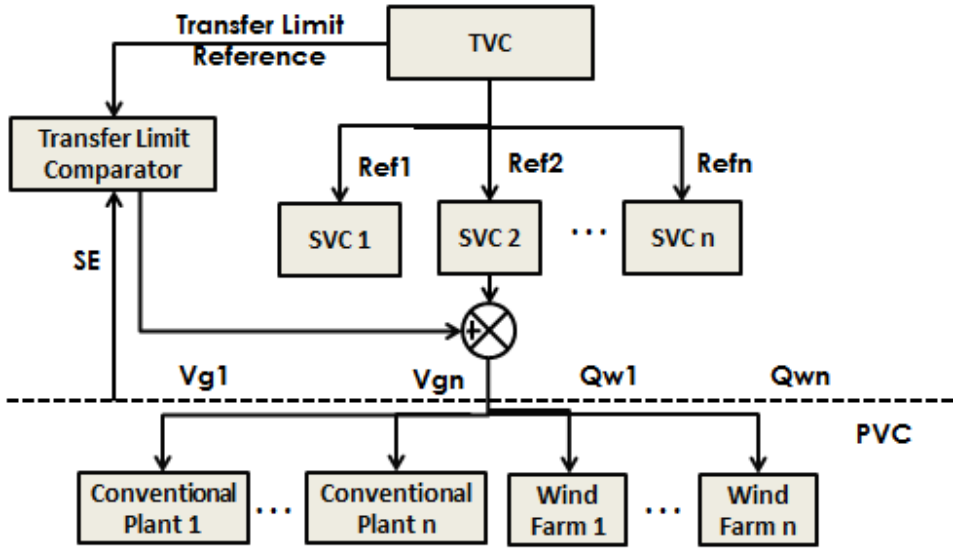

Fig. 1.9 Logical Structure of Proposed Hierarchical Wide Area Voltage Control

To encourage the participation of wind farms for system wide reactive power support, the output signal of the secondary level control is no longer unit stator voltage variance but the desired voltages at Point of Interconnection (POI) of each power plant. The primary level control now includes wind farm Automatic Voltage Control (AVC) to eliminate the voltage fluctuation caused by random wind variations. These enhancements encourage self-adjustment of wind turbines according to the given reactive references and fully utilize the already limited reactive resources in the system.

1.4.2 Main Contributions

The contributions of the dissertation can be summarized as follows:

1) Creation of an Equivalent WECC system with High Wind Levels and HVDC Overlay

Built as a test system for validation of the proposed control, this equivalent test system has wind farms and HVDC overlay to mimic the structure and operating conditions of future grid. The simulated response of the test system can provide helpful information to guide future grid operation and the regulation results presented can serve as reference for future field deployment of the designed controls.

2) Wide Area Voltage Control with Supply Variability

This dissertation proposes an effective wide area voltage control scheme with VAR deficiency and uncertainty from the wind used. The VAR deficiency is addressed at the tertiary level of the proposed

control, where the optimal allocation of reactive reserve is achieved by an OPF to best eliminate transient violations and improve security margins. The output uncertainty and variability are targeted at the secondary and primary level procedure, where wind farm AVC minimize the de-stabilizing impact of random wind variations through a coordinated regulation strategy encouraging wind plant participation in system wide reactive ancillary services. This allows the proposed control strategy to make the best use of all available VAR resources in the system to enhance performances with more than 20% of wind penetration.

3) Dynamic Security Constraints in Wide Area Voltage Control

In addition to static voltage limits and load flow equations, the planning standards for the transient behaviors of the system are embedded in the tertiary level OPF for the first time in wide area voltage control. With N-1 contingency analysis processed by transient simulations, the proposed control scheme attempts to ensure dynamic security constraints are respected. With the dynamic response confined within an acceptable range by the proposed control scheme, the fault ride-through capability of the system is improved. The capacity utilization reduced by high wind penetration can be restored without while protecting against voltage collapse and cascading element outages. The real time capability provided by its hierarchical architecture allows the proposed control strategy to act as a kernel for the future online dynamic security enhancement tools.

4) Analysis of Capability of Wide Area Voltage Control

The feasibility region of the proposed control strategy regarding system loading and wind levels is explored. With less manageable reactive reserve in the system, the proposed scheme has fewer resources dispatchable to achieve control objectives without violating voltage limits. Thus, the performance is weakened in scenarios where high wind penetration arises under either high or low load scenarios. Such situations are subject to either static reactive overabundance or dynamic VAR shortage, both of which restrict the re-allocation of plant-level reactive output enabled by the control scheme. This work explores the stand-alone capability of the wide area voltage control in dealing with various system conditions and provide references to future researches on the coordination of voltage control with other reactive resources.

This work uses an interior point method to solve the OPF and a sensitivity-based pilot bus selection method to enhance control efficiency. Those methods realize the implementation of the proposed control on the test system. Moreover, this research makes use of the damping provided by HVDC links to mitigate oscillations in scenarios with simultaneous occurrence of high wind and high loading. This approach can expand the feasibility region of the proposed wide area voltage strategy and secure power systems with very high wind levels. Cases are evaluated with wind greater than 35% (the expected penetration level in US power grid to reach by year 2050 [10]). The studies on the coordination between the proposed voltage control and HVDC overlay provide an alternative for future system operation and planning in an AC-DC hybrid power grid.

1.5 Scope of the Work

This dissertation focuses on the key aspects of the proposed HVC with regard to wind uncertainty, involvement of dynamic constraints and the coordination of HVDC overlay. The feasibility regions of this control scheme with and without the help of DC links are explored with the boundary conditions. Techniques applied to ensure load flow convergence in scenario studies are introduced. The regression approaches to map load flow solutions to dynamic constraints and security margin are also addressed. A multi-terminal HVDC overlay structure is built on top of a 197-bus equivalent WECC system. This equivalent WECC system serves as the test bed with year round scenarios constructed according to the WECC 240 bus hourly loading profile [58]. Variations of load and generation follow the trends of the archived data in the loading profile while the short term fluctuation of wind outputs mimic the 5-min real data record published on ERCOT webpage [59]. Details on this AC-DC hybrid WECC reduced system are elaborate with planning standards applied for evaluation of security on this reduced system.

The dissertation is organized as follows: the second chapter serves as a literature review of the methodology, implementation and test system preparation for wide area voltage control. The third chapter describes the methodology of proposed wide area voltage control together with the mathematic formulation of hierarchical Security Constrained Optimal Power Flow (SCOPF) problem. The fourth chapter focuses on customization and device integration during the procedure of test system model development. Chapter 5 and 6 present the control implementation and testing results analysis respectively. Chapter 7 provides the discussion on possible methods to expand the feasibility region of the proposed control and explore ways to enable coordination between HVC and HVDC overlay in cases with ultra-high wind penetration. The conclusions of this dissertation will be drawn in Chapter 8.

2. Literature Review

2.1 Overview

Voltage control began with manual operations at substations and power plants to meet the requirement given by system operators. Later, a centralized control was proposed to enable alignment between supervisory dispatch and local actions. Subsequently, regional control agents located at pilot nodes within each control area were added as a secondary regulation level to enable faster responses to disturbances while avoiding additional computation burden in the control center. Currently, with the increased complexity of the interconnected power system, the coupling among each control area has grown stronger and interactions among regional agents are inevitable. An adaptive control scheme is proposed to centralize the secondary voltage regulation and adjust regional agents and control area boundaries according to instantaneous system conditions.

Since the deployment of supervisory voltage regulation, the SCOPF has been used to reach the optimized voltage map for a power system under multiple security and economic constraints. With a computation interval ranging between 15 minutes to 1 hour, the SCOPF can adapt to operating condition changes and adjust the voltage profile of the system accordingly. Today with the involvement wind participation, the probabilistic SCOPF formulation has been investigated to avoid infeasible solutions due to grid uncertainty. With increasing concerns of transient violations of the system, blending dynamic security constraints into the SCOPF has become necessary. Since the difficulty in analytically representing those dynamic constraints, numerical formulations using multiple data training and regression approaches are proposed to enhance the accuracy of the formulation. The deployment of online DSA has provided great data resources for offline analysis and studies, which can be taken advantage of to enable the pattern recognitions for formulation of tertiary SCOPF and identification of secondary control agents.

The future power grid will see increasing penetration levels of wind generation as well as HVDC transmission. It may also be more vulnerable to potential dynamic insecurity. Therefore, a voltage control scheme to adapt to this trend is necessary. Both the hierarchical and adaptive schemes are implemented in practical power systems to enable wide area voltage control. Still, none of the field implementations has been reported on a system with more than 10% wind or with HVDC overlays. The use of Dynamic Constrained Optimal Power Flow (DCOPF) into field enforcement of wide area voltage control is neither seen in publications as well. While new control algorithms can address one of the above issues in test-bed simulations, realization of all three has not been seen in published report. Therefore, it is of importance to research wide area voltage control that can adjust to high wind and HVDC penetration as well as consider dynamic constraints for future power grid development.

2.2 The Methodology of Wide Area Voltage Control

The methodology of wide area voltage control includes overall architecture and mathematic formulation. Ever since the utilization of Supervisory Control and Data Acquisition (SCADA) system to enable communications between power plants and control centers in 1960s [60], the remote management on multiple system devices is handled by centralized computations. As the power grid grows in complexity, the discussion on choices between centralized and decentralized schemes has been the focus of many proposed wide area voltage control architectures. Accordingly, different approaches to mathematically represent and solve the SCOPF embedded in the control schemes have been investigated in past years [61]. The efficiency and adaptability of those approaches are analyzed under various power system conditions and practical requirements.

2.2.1 Literature Review on Control Architectures

1) Manual Control Schemes

In early days, control actions were performed manually to maintain equipment terminal voltages and maximize utilization of the transmission system [62]. Devices such as shunt capacitors and transformer tap changers are used for system to achieve a desirable steady-state operating conditions. Static VAR Compensators (SVC) help to hold voltage stable under loading variations [63, 64] while the application of synchronous condensers satisfy the need for large amount of reactive compensation during disturbances. This control scheme offered the only countermeasure to voltage problems before the development of control centers. The performance solely depended on the quality of devices and skills of operators, and thus was subject to device malfunction and human mistakes. This has led to demand in equipment maintenance and personnel training, both of which require high cost.

With the expansion of the power system, the exponential growth in the number of reactive compensation equipment has made manual operation difficult. Additionally, the interaction between compensation devices has negatively impact their performance. Automation and coordination on the operations with reactive compensation equipment is therefore imperative.

2) Two-Level Centralized Control Schemes

A two level centralized voltage control scheme was first studied by J. P. Priet in 1992 [65], where the primary control automatically confined the voltage variation within a pre-defined band while the centralized control maximized the reactive reserve on different generators responsible for voltage control. The centralized regulation was designed to be activated upon the request of the Transmission System Operator (TSO) [66] and was not auto-mobilized. As time goes by, the controllable devices in the scheme has expanded from unit excitation systems to shunt capacitors and transformer tap changers to actuate voltage

regulation at load buse s[67]. Since the proper operation of this two-level centralized control scheme requires close to zero import and export of reactive power among different regions, it is not adequate to manage a meshed and highly coupled power system. A regional control level needs to be added to suppress the inter-area reactive exchanges and alleviate the computation burden at control centers. Meanwhile, due to the increasing variability of current power system, automation and real time execution capability are encouraged for the centralized regulation so as to respond to system variations fast and accurately.

Though no longer suitable for implementations on large power system, this control scheme is still useful for small systems and micro-grids [68], where the system is neither large nor complicated enough and the regional regulation can be avoided without significant impact to control performances.

3) Hierarchical Control Scheme

The hierarchical control scheme consist of three levels, primary generator AVRs, secondary regional agents and the tertiary OPF dispatch at national level. This control scheme was first practiced by France for wide area voltage regulation [40], where three levels of system management with ascending control space and response time from primary to tertiary was realized. Later on, Belgium adopted a similar scheme and add a secondary level of regulation into its original two-level centralized control scheme [69]. In this control scheme, the secondary level regulation enforces the guidelines from tertiary OPF upon primary AVRs within each control area under consideration of current system conditions. The control areas are aggregations of electrically close buses that tend to have similar reactions or sensitivities towards variations of reactive output [45]. As development of power system, many modifications and innovations have been made to the secondary level control layouts regarding to algorithm design and network partitioning.

2.2.2 Literature Review on Structure of Secondary Voltage Regulation

Multiple layouts regarding to the secondary regulation in the hierarchical voltage control has been proposed and pushed to field deployment. There are mainly three types of structures for secondary voltage control that has been practiced by system operators and utilities around the world. Based on the network complexity and communication capability, each type of SVC layout has been customized to adapt to local power grid. For the classical layout of secondary regulation applied to some European power grids in early on, additional features are added for such traditional layout to accommodate evolving system development.

1) Classical Secondary Voltage Control

In this control scheme, regional computation centers are physically placed in geographically separate areas to enforce SVR. The network partitioning was completed offline and recognition of control zones as well as SVR configurations remain fixed throughout the online procedure. Voltage regulation actions issued by different regional agents are independent. The principle of the control was to divide the power network into pre-defined control zones and regulated the voltage profile separately in each zone by automatic

adjustment of AVRs. The voltage profile was regulated by minimizing the difference of between measured and reference voltage at the piloting node of each zone. A proportional integral controller was applied to calculate the required reactive level for each zone. The required amount would then be picked up by units within this control zone proportionally to their capabilities in reactive power provision and generator cooling system [70]. To execute the control, two conditions must be satisfied: 1) sufficient reactive power must be available in the zone; and 2) the electrical distance between two adjacent piloting nodes must be far enough to prevent undesirable interactions, which was generally satisfied in the past when control zones were weakly linked and voltage issues remained a local problem. The classical secondary control layout does not recognize interactions among different control zones, thus is only suitable for unmeshed and weakly coupled systems.

The Belgium power grid adopted this control structure since its high voltage transmission grid subject to wide area voltage control is comparatively simple in connectivity [71]. However, in places such as Italy, certain modifications were essential for desired control performances. Those modifications included: 1) replacement of destabilizing unit reactive power control loop with an autonomous microprocessor based, voltage and reactive power regulator, named REPORT [70, 72, 73]; and 2) Pre-selection of control generators based on unit reactive capability and electrical coupling to pilot nodes. The REPORT system served to amend secondary level commands with consideration of situational demand on local reactive support while the pre-identification of control units assured minimized influences between adjacent control zones. With the assistance of plant-level autocracy enabled by REPORT and pre-selected control generators based on sensitivity analysis, the drawbacks due to isolated secondary regulation can be mitigated.

2) Coordinated Secondary Voltage Control

As increased coupling among theoretically independent zones and excessive reactive demand made on certain units to effectively control pilot node voltages, a coordinated approach to SVR was proposed and experimented in Electricity de France (EDF) [46], where a regional computation center was preserved at each predefined control zone. In this coordinated approach, a set of pilot buses were selected within each control zone and set point values for primary unit controls were computed at a much shorter interval compared to classical SVR, which demands all the control action be finished within 10 seconds. With the effect of each generator on pilot buses represented by a sensitivity matrix, the most sensitive unit could be prioritized to regulate the pilot bus voltages within each control zone while actions of units controlling bus voltages at adjacent control zones will be suppressed to minimize the undesired interactions among each zone [74]. In some literature, even the fluctuations of the inter-area transfer flow are suppressed to shield interference from neighboring control areas [43]. As the coordination of the secondary regulation is represented as a multi-objective optimization problem, this secondary layout allows the control developer to prioritize certain control objectives by assigning larger weighting factors to the corresponding term. This

coordinated secondary voltage control managed to confine actions of regional agents within its own responsible area while preserving flexibility for future development. It is useful and effective in power systems with little structural changes since predefined zone division won't be able to reflect instantaneous connectivity changes caused by element outages nor evolving topology development due to device commissioning. In addition, the application of the coordinated voltage control requires high coverage of high sampling rate measurements in the system to support the shortened control interval.

Currently, this coordinated secondary voltage control was adopted by REE, the company which operates the national power transmission grid in Spain, to incorporate with the current primary generator AVRs for construction of multi-level system management [75-77] and consummation of its voltage control service in ancillary market [78]. As a mature power grid, the Spanish system is meshed but no longer subject to frequent network upgrades. Furthermore, it was proved in a corresponding study [76] that the selection of pilot buses and control units were not severely influenced by variations in operating conditions. In other words, the desired control performance can still be achieved with fixed recognition of control area boundaries under varying operating conditions. Therefore the offline zone division approach is adequate for field implementation in Spain. In the case of communication capabilities, the Spanish power grid has ensured full observability of the whole system with high sampling rate measurements. However, this is not the case in WECC, which is the major grid considered for the proposed hierarchical voltage control. As a one of the biggest power systems depending largely on SCADA units with sampling period longer than 10 seconds [79, 80], the coordinated design of secondary level regulation is prone to time delay in the WECC.

3) Adaptive Secondary Voltage Control

In this layout, in order to respond fast to the topology changes in the system, the physical restriction of a regional computation center as well as the predefined control area recognition was abandoned. Instead, the secondary level of regulation is combined with the tertiary OPF in the central control room with dynamic control area identification where an online network partitioning method was used to divide the system into different control zones. In this method, the log-transformation of sensitivities matrix were recognized as the reactive control space, in which the vector consisting of the sensitivity index of one particular PQ bus voltage with respect to all unit MVAR output variations was regarded as the coordinates of this PQ node. The electricity distances between each PQ node were then described by the Euclidean distances between their coordinates [81]. Consequently, PQ buses with similar sensitivities to generator MVAR variations will have shorter electrical distances. The system will then be clustered into different control zones based on a hierarchical clustering analysis, where nodes close to each other in electrical distance were identified as one group [82, 83]. In this online automatic zone division mechanism, the boundary of control areas as well as participation of controllable units can be modified with evolving system conditions and power grid structural changes can be recognized instantaneously for the wide area voltage control. Meanwhile, the

aggregation of tertiary and secondary level of regulations within one control center would reduce communications and simply the procedure. This communication-friendly feature and adaptive zone partitioning mechanism prove to be the most suitable for meshed power grid located in areas with high population density, where direct access to unit settings from control center is possible and fast structural developments and volatile network changes on electricity systems are common. Therefore, it was first validated in multiple provincial power grid in China [84] and later on implemented as the online Optimal Voltage Control system in Pennsylvania-New Jersey-Maryland Interconnection (PJM) [85, 86], which covers the most populated areas along the US east coast. For the WECC, where utilities own power plants within their service area and are reluctant to share access to unit adjustment with others, this adaptive voltage regulation scheme turns out to be impractical.

4) Summary

A summary of architecture and adaptability of each control scheme is listed in Table 2.1.

Table 2.1 Summary of Different Wide Area Control Schemes

Scheme		PVR	SVR	TVR	Adaptability	Limited By
Manual		Yes	No	No	No longer adaptable	Grid complexity
Centralized		Yes	No	Yes	Adaptable in simple systems	Grid complexity
Hierarchical	Classical	Yes	Yes-isolated	Yes	Adaptable in weakly coupled networks	Grid connectivity
	Coordinated	Yes	Yes-coordinated	Yes	Adaptable mature grids	Communication /grid development
	Adaptive	Yes	Yes-online zone division	Yes	Adaptable in developing grids	Communication /grid deregulation

2.2.3 Literature Review on Security Constrained OPF (SCOPF)

There are many objectives for tertiary OPF. One of the earliest is designed to regulate load bus voltages that were inclined to fluctuations from supply end [87, 88]. This was usually observed in the power grid where the connection between generation and load were simple. Later on economic dispatch and security enhancement were included to enhance electricity market profit and system utilization rate under N-1

contingencies [89]. The past contingency analysis only involved studies on pre-contingency and post-contingency situations. Currently, as the dynamic performances of system elements are more critical, the dynamic constraints need to be included to achieve optimal dispatch objectives. With the development of online DSA [90, 91], many OPF based wide area voltage stability and security enhancement approaches have been introduced [92], and many deterministic and nondeterministic formulations of tertiary optimal dispatches have been developed accordingly.

1) SCOPF formulation based on Energy Function

This is a deterministic formulation of OPF. In order to incorporate dynamic stability constraints in optimal power flow dispatch, the Lyapunov functions [93] are utilized to evaluate the fault-on and post fault trajectories of power system in terms of generator angle deviations. The OPF will then compute the desired system settings based on those evaluations to enhance stability margin under predefined contingencies [94-96]. Lyapunov function based methods supporting those OPFs are categorized as energy function approaches. In those approaches, the Stable Equilibrium Point (SEP) θ_S and the Unstable Equilibrium Points (UEP) θ_u are located for a specified system. When a fault is induced, it injects kinetic energy into the system and drives it away from the SEP. The total energy in the system increases along the fault-on trajectory until fault clearance, then due to the low of the conservation of energy, it stays constant as the system moves towards the UEP and its kinetic energy slowly converts to potential energy. If the kinetic energy at the UEP is still positive, namely the angular speed of the any generator is larger than zero, the system will pass the UEP and become unstable. Therefore, the potential energy at the UEP needs to be larger or equal to the total energy in the system at the fault clearance to ensure stability. The key point in the energy function based methods is to identify the locations of UEPs or the critical potential energy in terms of generator angle deviations. Then the critical potential energy V_{cr} can be obtained as the stability boundary of the system.

There have been three methodologies in locating the UEPs, the first one is called the Lowest energy UEP (LEU) method [97], where the Lyapunov function was directly applied in the post fault trajectory evaluation of power system and all the locations of UEPs are computed to find the lowest critical potential energy. As the result, the computation effort grows exponentially with the dimension of the power system and this method is no longer favored for large scale power grids.

The second approach is called the Potential Energy Boundary Surface (PEBS) method [98]. Instead of looking for the UEP for a specified contingency, it directly estimates the critical potential energy the system possesses at the UEP. In this method, the concept of a boundary consisting all the UEPs are proposed and the derivative of potential energy $V_{PE}(\theta)$ with respect to generator angle θ is monitored along the fault-on trajectory until its product with angle deviation equals to zero as shown in (2-1). This is when the fault-on

trajectory crosses the PEBS and the corresponding potential energy $V_{PE}\left(\theta^*\right)$ at this point presents a good estimation of system stability boundary.

$$-\frac{\partial V_{PE}\left(\theta^*\right)}{\partial\left(\theta^*\right)}\cdot\left(\theta^*-\theta_S\right)=0 \tag{2-1}$$

Though much more computational inexpensive compared to the lowest energy UEP method, the PEBS method only gives conservative results when certain conditions regarding the number of UEPs and behaviors of fault-on trajectories are satisfied [99], otherwise, the accuracy of this method is questionable. Hence the Boundary Controlling Unstable Equilibrium Point (BCU) [100] approach is proposed to avoid the solution inconsistency brought on by the PEBS method. In this approach, when the fault on trajectory reaches the PEBS at $\theta=\theta^*$ corresponding to $t=t^*$, the set of equations below are integrated for $t>t^*$ until $\left\|f\left(\theta\right)\right\|$ reaches the minimum.

$$\dot{\theta}=f\left(\theta\right) \tag{2-2}$$

$$\theta\left(t^*\right)=\theta^* \tag{2-3}$$

Here $f(\theta)$ denotes the post-fault trajectory. This integration will take $\theta(t)$ along the PEBS to the saddle point and eventually find the UEP by solving $f(\theta)=0$ with the saddle point as initial guess. The BCU method has proved to provide conservative estimation of the stability boundary at conditions when the PEBS fails [101]. The BCU method has been adopted in the Bigwood software to support the online stability constrained OPF. Nevertheless, its performances may falter on grid with low damping and high loading [99] if no additional countermeasures are taken. This is exactly the condition of today's power system with massive integration of wind turbines and souring customer demand for electricity.

In general, energy function methods can offer the tertiary OPF an explicit stability boundary in terms of generator angle. Via adoption of stability index, the OPF can maneuver the unit terminal voltages and outputs to achieve desired enhancement of stability margin. However, most security criteria for the transmission grid today focus on load bus voltages. Though enhancement of voltage security in terms of loadability has been realized by energy function based sensitivity analysis [102], there has been little research on using energy function to optimize the transient behaviors of load bus voltages, which is a major focus of this dissertation.

2) SCOPF formulation based on Numerical Integration

As another deterministic expression of the power system transient behaviors, numerical integration of generator swing equations is often used for the power system simulation software. In this method, differential equations regarding to generator parameters such as inertia J, angle θ and accelerating torque T_a are solved at each time step and corresponding bus voltages and phase angles are obtained under algebra constraints.

$$J\frac{d^2\theta}{dt^2} = T_a \tag{2-4}$$

Usually, for security constrained problems with multiple contingencies, a Time Domain (TD) analysis of 20 seconds are required to completely exclude instable situations, which would take much longer than 20 seconds to finish. Hence, OPF based on time-domain analysis is not favored since multiple search steps might be required to find optimal. Efforts have been made to speed up the procedure including discretization of trajectories, conversion of constraints and partition of the SCOPF problems. Capabilities to include wind generation are often realized via stochastic programing with a variable denoting wind forecasting error in the security constrained OPF problem. Usually, this variable is subject to predefined distribution therefore may not 100% represent the actual wind fluctuation. Moreover, such dynamic security constrained OPF has constraints functions mixed with differential and algebraic equations simultaneously, which presents an obstacle in searching for feasible solutions.

a. Discretization of Transient Trajectories

Under N-1 contingency screening, where the trajectories of a perturbed system are discretized at each time step, the first order optimality condition is utilized to get rid of differential terms in the OPF constraints [103, 104]. Researchers from Cornell University applied the trapezoidal rule to integrate the generator angles and speed at each discretized time step [105]. This has greatly simplified the integration procedure of differential equations and allowed OPF solutions with stability constraints under N-1 contingency screening. However, discretization of trajectories may induce errors in calculation that contribute to excessive computation time and non-convergent results. Moreover, the dimension of variables and constraints produced by discretization grow exponentially with the contingency number and simulation time, hence is only suitable for short-period transient studies of small scale power systems.

b. Conversion of Transient Constraints

Another way to incorporate dynamic constraints in to the OPF is to convert the constraints on differential equations into bounds on the initial values of state variables. In order to access this, the swing behaviors of generators are studied and instability regions in terms of rotor angle are established as shown

in Fig. 2.1 [106].

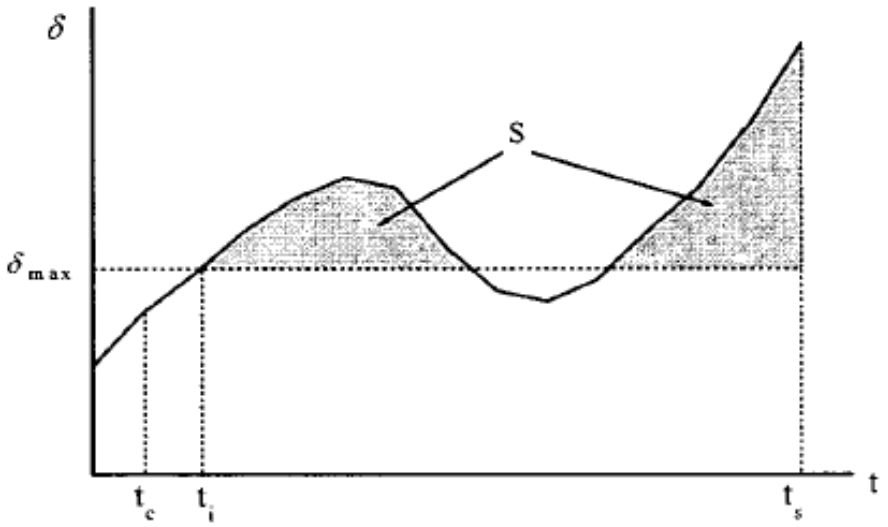

Fig. 2.1 Intuitive Expression of Transient Stability

Hence, the differential equality constraints in the constrained functions are replaced by integral inequality constraints representing the shadowed area, which can be successfully realized for high dimension problem by Euclidean space transformation [107]. Then the Karush Kuhn–Tucker (KKT) conditions for optimality are applied and the search of the optimal point depends only on algebraic expressions since the first and second-order derivatives of integral inequalities don't contain integral signs. OTS problem formulated based on this approach may be subject to premature solutions since with positive damping; the shadowed region in Fig. 10 doesn't have to be zero to ensure stability. After all, the conversion of transient constraints prevented the exponential growth of the OTS problem with system dimensions. However, the calculation of Jacobian and Hessian matrices at each searching step requires a high computational burden, which explains why this approach has not been practiced for OTS with multiple contingencies.

c. Partition of SCOPF Problems

This approach was first practiced in [108], via sensitivity analysis of transient trajectories, the OPF with Transient Stability Constraints (OTS) problem is partitioned into two sub-problems concerning optimal power flow and transient stability respectively. Those two sub-problems are solved in turns at each time step to obtain the optimal operating point under stability constraints. Though subject to pre-mature solutions, this method has freed the solution of stability constrained OPF from the impact of system dimensions and greatly increased solution quality. This methodology was discussed and enhanced in in multiple

publications [109-111]. Reference [112] added reduced order dispatch to the original two sub-problems and made the approach suitable for managing multi-contingency situations on large scale power systems.

All the above numerical integration based OPF formation select a threshold in rotor angle deviation as an index to detect instability according to industrial experiences [113]. This has led to the common drawback in deterministic formulation of security constrained OPF, as it is hard to incorporate the dynamic security standards concerning transient performances on load buses into the generator angle threshold. The violation of such criteria can only be checked via time domain analysis where the transient voltages of the monitored buses are calculated at each iterative step of the generator swing equations. This raises a need for the non-deterministic formulation of OPF for optimization of power system operation solutions in real time considering expectations from end-users.

3) SCOPF formulation based on Pattern Recognition

The pattern recognition [114] method implicitly formulates the OTS constraints and objectives. It is free from the inconvertibility between rotor angle threshold and transient voltage dip limits as well as the overall high computation cost associated with explicit formulations. Thus, it is considered the most suitable approach to enable online operation of security constrained OPF.

There are mainly two categories of pattern recognition techniques when considering system behaviors under multiple contingencies. The first category is formed by the classification approaches, where each input was assigned to a given set of class. A good example of such methods applied in OTS problems is the decision tree methodology [115], which contains the learning process and the training process. In the learning process, the transient performances of system with load and generation variations are evaluated under predefined contingencies. For each of the operating snapshot, there is an evaluation on whether it is secure (stable) or not. Then the training process will classify all the scenarios into two subsets according to the evaluation results, the decision tree is derived to identify the security (stability) region in terms of system pre-contingency attributes [116]. The scenario with all steady state attributes examined strictly inside the stability region can then be a feasible solution of the OTS problem.

The decision tree methodology has proved a tractable description of the relationship between pre-event system attributes and its security (stability) state, which can be used to re-dispatch the unit voltages and outputs for stabilizing the power grid. However, the complexity of the classification procedure will grow with the number of contingencies and security standards, which makes the decision tree based methodologies impractical for large systems subject with multiple security criteria. Another drawback of the decision tree based method is its inability to provide the mapping between security (stability) margin and critical system attributes. This has made the OTS depend on decision tree methodologies less useful in quantitatively enhancing the operating margin of power system.

The second category consists of the regression approaches, where a real-value output was assigned to

each input. The Artificial Neural Analysis (ANN) [117] based analysis is one of the analysis methods that belongs to this category. Due to its capability to handling large amount of data sets with complicated nonlinear relationships, the ANN analysis is often applied for the forecasting of dynamic security margins [118] and assessment of grid vulnerabilities [119] in the power system. Like the classification category of pattern recognition approaches, the ANN analysis contains learning and training procedures. A multi-layer network with autonomous neurons at each layer carries out the training process. The complexity of the network in terms of the number of layers and neurons will highly affect the training result and the computational cost, which would greatly affect the solution of the OTS problem. Usually to resolve this issue, data truncation method like factor analysis is applied.

In practical use, the ANN analysis is superior at implicitly representing complicated nonlinear patterns between inputs and outputs. For other patterns with higher simplicity in mathematic formulation, classical regression methods such as, linear and quadratic regression, may give better performance than ANN. The classical regression presents superiority in handling uncertainties associated with input parameters. The regression category of pattern recognition opens the gate for managing generator settings according to end user expectations, evaluation of the actual situation is necessary to select the most appropriate regression method. Despite the advantages in using regression approaches to deal with dynamic constraints and wind uncertainties, the massive amount of data input remains a problem as it exponentially increases the problem dimension and training time. Besides, certain measures have to be taken to ensure similarity between the training set and the application set, namely the recorded system conditions based on which the projections are trained must be close enough to the actual system conditions where those trained projections are to represent the mappings between system attributes and the corresponding security margins or constraints.

4) Summary

A summary of published methodologies on the formulation of tertiary security constrained OPF for the proposed wide area hierarchical voltage control is listed in this section, where the summaries on characteristics energy function and pattern recognition is displayed in Table 2.2 and the summaries on properties of numerical integration is displayed in Table 2.3.

Table 2.2 Summary of Methodologies on Formulation of Tertiary OPF (Part I)

Methodology	Energy Function			Pattern Recognition	
Category	LEU	PEBS	BCU	Classification	Regression
Explicit Formulation	Yes	Yes	Yes	No	No
Computation Cost	High	Medium	Medium	Low	Low
Susceptibility to System Conditions	Low	High	Medium-need countermeasures	Low	Low
Susceptibility to Problem Dimensions	High	Low	Low	High	Medium-need order reduction
Compatibility with Stability Constraints	Yes	Yes	Yes	Yes	Yes
Compatibility with Security Constraints	No	No	No	Yes	Yes
Security (Stability) Margin Evaluation	Quantitative	Quantitative-on V_{cr}	Quantitative-on V_{cr}	Unquantifiable	Quantitative-on bus voltage
Ability to Handle Uncertainty	Low	Low	Low	High	High
Applicability to Online OTS	No	No	Yes-Commercial	Yes-Research	Yes-Theoretically

It is clear from table 2.2 and 2.3 that tertiary OPF formulated based on pattern recognition is indispensable to incorporate dynamic security standards and handle uncertainties from high wind penetration. Furthermore, the regression category of methods can quantitatively evaluate the security margin in terms of bus voltage, an index directly associated with security standards. Since the use of regression approach in online dynamic and uncertainty constrained voltage control has yet to be seen in in the literature, the dissertation proposes a data training approach based on the regression theorem where the tertiary OPF formulation of the proposed HVC is obtained and the disadvantages associated with regression category of pattern recognition is overcome.

Table 2.3 Summary of Methodologies on Formulation of Tertiary OPF (Part II)

Methodology	Numerical Integration		
Category	Trajectory discretization	Constraints Conversion	Problem Partition
Explicit Formulation	Yes	Yes	Yes
Computation Cost	High	High	Medium
Susceptibility to System Conditions	High-may not converge	Medium-may find sub-optimal value	Low
Susceptibility to Problem Dimensions	High-affected by problem scale	Medium-affected by system scale	Low
Compatibility with Stability Constraints	Yes	Yes	Yes
Compatibility with Security Constraints	No	No	No
Security (Stability) Margin Evaluation	Quantitative-on θ deviation	Quantitative-on on θ deviation	Quantitative-on on θ deviation
Ability to Handle Uncertainty from wind generation	Medium- pre-defined forecasting error	Medium- pre-defined forecasting error	Medium- pre-defined forecasting error
Applicability to Online OTS	Yes-for small system with limited contingency	Yes-for small system	Yes-research

2.3 Practical Implementation of Wide Area Voltage Control

There are basically three major problems associated with the implementation of online wide area voltage control. The first is the selection of pilot buses whose voltages are monitored and benchmarked for the execution of regulation actions. The second is the load flow convergence issue, as the voltage control may not find viable solutions under certain extreme conditions. For this issue, the dissertation provides a clarification of such operating conditions where the proposed voltage control is not applicable and proposes a systematic analytic approach to identify the boundary of its feasible regions. The last problem is the communication requirements for secondary regulation layout such as adaptive SVC, coordinated SVC, devices supporting fast communication are necessary, and the wide area voltage control is vulnerable to communication delays. In the secondary layout of the proposed HVC, frequent inter-level exchange of information is not necessary and communication delay is not a focus in this work.

2.3.1 Literature Review on Pilot Bus Selection

The selection of pilot nodes are generally based on the intuitive idea that such buses must be chosen to be among the strongest ones that ensure both observability and controllability [120], i.e., able to represent the behavior of local control area and impose voltages on other electrically close buses. The design criteria, based on short-circuit capacities and sensitivity matrix computations, also requires that the electrical coupling between pilot nodes to be sufficiently low to decouple dynamic interactions between secondary control loops [72].

There are two mechanisms for pilot bus selection. One mechanism was developed in early stages of secondary voltage regulation when maintaining the stable state of the system was the major task for system operators. It prefers pilot buses to be the most centralized nodes so that all the load bus voltages within this area can be supervised. Subsequently, the secondary voltage regulation became responsible for enhancing the stability margin of the system and certain units are supposed to pick up more responsibility than their peers to counteract system weakness. Under this condition, the level of controllability that pilot buses can impose on the system rises as a new focus and the sensitivity of the load buses to unit actions serves a new criterion for pilot bus selection in the second mechanism.

1) Prioritization of 'Most Central' Nodes

There is an empirical method to identify the most centralized node, where the short circuit power is computed for selected buses as product of rated voltages and short circuit current as shown below

$$S_f = I_{SC} \cdot U_N \tag{2-5}$$

Buses with higher S_f are assumed to have more parallel connections and therefore more electrically close to other buses in this control area. Hence, they will be regarded as candidate pilot buses. Repeated load flow computations are then performed. For each computation, a single voltage source is placed at each of the candidate nodes and the remains of the system are represented by passive impedance. The voltage drop between the candidate node and other buses are then computed and archived. Once the computations for each candidate pilot bus have been completed, the voltage drops associated with each candidate pilot node are compared to nominate the electrically closest point to all other buses as the pilot bus of this control region [45, 121].

Later on, with the increase in the complexity of power network, the central node identification based on intuitive analysis and successive load flow computation is no longer efficient. Electrical de France (EDF) has consequently made an attempt to devise a heuristic method for the determination of the pilot nodes where the electricity distance between buses *i* and *j* is represented as the log-sensitivity of voltages as (2-6) shows

$$D_{ij} = -\log\left(\frac{\partial V_i}{\partial Q_j}\cdot\frac{\partial Q_j}{\partial V_j}\right) = -\log\left(\frac{\partial V_i}{\partial V_j}\right) \tag{2-6}$$

The quantitative concepts of structural observability and controllability [122] can show that the electrical distance between two nodes are independent from disturbances, namely, fixed by system structure. Moreover, a node which controls voltages has a marked influence only in the close vicinity. As a result, a critical distance D_0 above which two nodes are considered decoupled can be obtained. Here, the D_0 be used as a threshold to determine the responsible space of a pilot node and the pilot node are selected to minimize the sum of its electric distances to other buses.

$$\underset{i}{Min}\sum_j D_{ij} \quad s.t.\ D_{ij} \le D_0 \tag{2-7}$$

This pilot bus selection mechanism can determine the "most central" node of a control area where every bus electrically locates within the limit of observability. This allows the strongest supervision of the system but fails to address the control objective in later design of secondary voltage regulation. Hence, a new pilot bus selection mechanism allowing prioritization of sensitive nodes to controllable generators and critical system loads has been proposed and widely implemented in current wide area voltage and reactive regulations.

2) Prioritization of Sensitive Nodes

This type of mechanism emerged when the choices of pilot node needed to consider the sensitivity of load buses with respect to pre-selected control generators to ensure both observability and controllability. With the objective to counteract load disturbances so that to maintain the voltage at pilot nodes, the sensitivity based pilot bus selection is more systematically developed compared with prioritization of most central nodes. Previously, the steady-state sensitivity analysis is a traditional way to study the relationships between controllable variables and state variables of power system [123]. Linearized from the load flow equations, the steady-state sensitivity analysis has been widely applied in the design of wide area voltage supervision and control [124-126]. In this type of analysis, the sensitivity matrices converting reactive injection variations to magnitude changes on voltages were derived [127]

$$\begin{bmatrix} S_{GG} & S_{GL} \\ S_{LG} & S_{LL} \end{bmatrix}\begin{bmatrix} \Delta V_G \\ \Delta V_G \end{bmatrix} = \begin{bmatrix} \Delta Q_G \\ \Delta Q_L \end{bmatrix} \tag{2-8}$$

The sensitivity matrices are then used to maintain the steady-state pilot bus voltage, i.e.,

$$\Delta V_p = -CS_{LL}^{-1}S_{LG}\Delta V_G + CS_{LL}^{-1}\Delta Q_L = 0 \tag{2-9}$$

where C is a matrix denotes the location of pilot buses. Since the number of control units is more than the number of pilot buses, this objective can be achieved via minimizing the actions of n_G control units:

$$Min \sum_{i=1}^{n_G} \Delta V_G^2 \tag{2-10}$$

This objective function can be transformed into the minimizing the trace of a matrix multiplication.

$$\begin{aligned} &\underset{C}{Min}\ \Im(C) = trace\left[P_L \left(I - BFC\right)^T Q_X \left(I - BFC\right)^T \right] \\ &B = -S_{LL}^{-1} S_{LG} \\ &F = \left(CB\right)^T \left(CBB^T C\right)^{-1} \end{aligned} \tag{2-11}$$

In this formulation of pilot bus selection, the weighting matrix Q_x is used to weight the relative importance of maintaining voltage magnitude in a given load bus with respect to other load buses. The covariance matrix P_L is used to denote the coupling among voltage variations of different load buses. By incorporating Q_x and P_L in the objective function, this approach to select pilot bus has ensured controllability by taking into account the grid weakness. By using this approach, system operators will be able to lay on certain pre-selected control units to compensate for the weakness. This optimization problem can be solved via several analytical search methods including the greedy solution, the extended greedy solution and simulated annealing algorithm [120, 128-130].

Steady-state sensitivity analysis is becomes less accurate for highly developed power grids as the impact from unit control actions and variations of loading level can no longer be neglected and balancing of supply and demand via a single reference bus with unlimited power provision and absorption capability is no longer practical. Therefore, a quasi-steady-state sensitivity analysis [131] was proposed where the extended impedance matrix was constructed to enable proportionally distribution of slack generations. Flexibility in bus type switching was made possible to account for the units with AVRs. A statistic based search algorithm[132] implemented in the automatic voltage control of Chinese power grid made use of the quasi-steady-state sensitivity analysis to accurately locate a number of pilot nodes that are most coupled with both control units and monitored buses. Unlike the analytical search algorithms, this statistic based method can determine the quantity of pilot nodes needed for each control area via Principal Component Analysis of sensitivity matrices.

The pilot bus selection shows great adaptability in field application due to the complexity of Chinese power grid and the fast-response secondary control loop that leads to frequent unit adjustment. However, it is too computationally costly for other systems with slower secondary regulations.

3) Summary

A summary of existing pilot bus selection methods can be seen in Table 2.4.

Table 2.4 Summary of Pilot Bus Selection Methods

Mechanism	Approach	Capability	Observation	Adaptability	Drawbacks
Prioritizing central nodes	Short-circuit Capability	High observability Low controllability	Balanced for all nodes	Simple and Small System	Lack of adaptability and controllability
	Electrical Distance	High observability Low controllability	Balanced for all nodes	Monitoring of meshed system	Lack of controllability
Prioritizing sensitive nodes	Linearized Steady-state sensitivity	High observability High controllability	Balanced for all nodes	Maintenance of light-loaded system	Linearization error in stressed system
	Quasi-steady-state sensitivity	High observability High controllability	Balanced for all nodes	Fast regulation of complicated system	Unnecessary Computation for slower regulation

By looking at the table, it is clear that all the published pilot bus selection approaches work with balanced observation on all the buses thus none of them are directly applicable to the proposed HVC as the primary control objective is to enhance system margin represented as COI transfer capability. This means the proposed HVC needs to reinforce system weak parts including three AC lines that forms the COI intertie and the load centers in California by intensified supervision on corresponding bus voltages. The monitoring on voltages of buses located in non-critical areas can be laid back to reduce the burden of observation. Hence the first pilot bus selection approach allowing biased observation is developed by this dissertation, it serves the purpose of the proposed voltage control while being accustomed to the practical situations where the control is applied. That is the system suffers from long periods of intensive loading with high wind penetration and the secondary loop of the control is slow due to lack of communication capabilities in WECC.

2.3.2 Literature Review on Feasibility of Control Strategy

The feasibility proves to be a great concern for any online voltage and reactive power control since it is supposed to deal with a wide range of operating conditions. The feasibility of a wide area voltage control is impacted the load flow solvability and the disturbance resistibility of each scenario. In case of online voltage control with transient contingency screening, the load flow solvability equals to the robustness of state estimation [133] and the disturbance resistibility refers to the ability of a disturbed system to remain secure during the contingency period. While online state estimation can adopt the global convergent methods to achieve solution for almost all cases [134], the disturbance resistibility can only be restored by managing available resources of the system. Thus for voltage control, the reactive resources are managed to mitigate transient voltage dips and speed up system recovery from a contingency. When there is little available reactive resource in the system, the voltage control ceases to have effect and this is the boundary of the feasibility region of the online wide area voltage control. To enhance the performance of the online voltage control, it is crucial to increase the robustness of state estimator and meanwhile explore the feasibility boundaries ahead of control deployment so that extra measures to provide reactive support can be taken to assist the online voltage control under extreme operating conditions.

1) Enhancement of Solvability

The enhancement of solvability differes for online and offline. For online, with the introduction of measurements, there are basically two issues contributing to insolvability of a case: the numerically ill-conditioning problem and large residual due to poorly calibrated measurements. The first issue is resolved successfully with QR factorization and the second one can be addressed enhancing the robustness of online state estimation via applying trust region methods [135]. Although there is no way to ensure a convergent solution for every problem and the online state estimation in industrial application still fails occasionally due to system stress, we can use the adaptive zone division mechanism to mitigate the influence of state estimation failure on the automatic voltage control [136]. However, the adaptive zone division mechanism is only applicable in a highly regulated power system with devices supporting fast and accurate information exchanges, which remains a luxury for most parts of the US power grid.

Hence, the offline practice is to remedy the online state estimation when cases become unsolvable due to overwhelming system stress. In this case, special convergence characteristics of damped Newton method [137, 138] and the concept of normal vector [139] can be used, where the minimum Euclidean distance between the unsolvable point and the boundary of solvability is measured so that corresponding control actions can be taken to drive the system back to solvable region. For a load flow OPF using direct interior point methods, this can also be used to restore solvability, especially for large scale ill-conditioned and voltage problem networks [140] as it is less susceptible to the variations of initial guesses. Both methods in

offline remedies for online state estimation are imperfect. The damped newton method is only practical when the unsolvable point is close to the solvability boundary, otherwise, the large number of control actions will be a headache for implementation. The direct interior point OPF is a nonlinear programing problem and is computationally costly to form and factorize the Hessian matrix [141].

2) Exploration of Feasibility Boundary

The feasibility region of the proposed voltage control disappears when the reactive redundancy is inadequate to help the system through the most critical contingency. Hence, the boundary of feasibility region is related to the transient security limit of the system defined by security standards. A reachability analysis can theoretically link the transient voltage behaviors with unit electric field voltage E_{fd} and therefore determines the secure sets in terms of unit terminal voltages in the system under a specified disturbance. The reachability analysis requires backward search including differential-algebraic equations (DAE) to model continuous bus voltage dynamics. This procedure is computational costly for high-dimensional problems and suffers from non-uniqueness in reverse time trajectories [142]. Thus, the reachability-based security boundary analysis has only been applied in Single Machine Load Bus (SMLB) systems [143, 144]. Another way to describe the feasibility boundary of the online voltage control is to numerically state it via case analysis. In published works, online voltage control has not yet considered dynamic constraints and wind uncertainties, let alone the boundary analysis in terms of wind penetration. In addition, most publications focus on the promising results of their proposed control instead of studying the limitation regarding the control implementation. Hence, this dissertation seeks to address this research area and be the first to illustrate the reachability of a dynamically constrained control designed for uncertainty management.

3) Summary

A summary of existing method to enhance case solvability is listed in Table 2.5.

Table 2.5 Summary of Methods to Enhance Case Solvability

Scenario	Applications	Methods	Objective	Drawbacks
Online	State Estimation	QR-factorization	Solve ill-conditioned cases	No guarantee on convergence
		Trust-region	Solve large residual cases	
Offline	Load-flow Analysis	Damped Newton	Address unsolvable online cases due to stress	Initial input sensitive
		Direct IP OPF	Address unsolvable online cases due to stress	Hard to form and factorize hessian matrix

The proposed HVC aims for online deployment on a system subject to long periods of intensive loading and high wind penetration. Without support for online adaptive zone division, the HVC must feed in cases with convergent load flow results in a timely manner to initialize control actions. However, from Table 2.4, it can be seen that current methods for enhance case solvability are all subject to drawbacks that either result in unsolved cases or contributes to time consuming solutions, which will definitely interfere with the online application of the proposed HVC. Therefore, this dissertation would propose an approach based on intuitive optimal reactive power flow as an offline remedy to fast resolve load-flow divergent cases. Measures like switching in back up units and fixed shunts are taken to allow big enough feasibility region under wind uncertainties and avoid singularity emerging in the hessian matrix. This would greatly reduce the time and computational effort spent in matrix factorization and speed the solution process. The OPF based offline remedy to enhance case solvability can enlighten future online state estimation that supports multiple real time operational studies.

Moreover, this dissertation initializes the search for the feasibility boundary of HVC firstly via enumeration method, where scenarios with extreme operating conditions are studied to intuitively describe the boundaries in terms of loading level and wind penetration. As the study is based on archived data, without dramatic changes in system topology, this intuitive result provides insight for extreme condition alarming in the online deployment of the proposed voltage control. In addition to enumeration, this dissertation also seeks to mathematically formulate the system conditions regarding feasibility boundaries of the HVC by incorporating load flow constraints and unit reactive capability in the reachability analysis. Though only applied in SMLB system, such formulations can be extended to actual bulk systems in future work.

2.3.3 Literature Review on Devices for Control Communications

The communication of online voltage control is usually taken care of by synchrophasors, including Phasor Measurement Units (PMU) and SCADA. PMUs can provide a data reporting rate around 30-60 records per second and are therefore able to accommodate the need for fast communications in the coordinated SVC and adaptive SVC. However there are only 1700 production-grade PMUs deployed across the massive area of US and Canada [145], where existing PMUs suffering from data inaccuracy due to calibration problems and GPS non-synchronism[146]. Such data errors will lead to questionable voltage information that clouds the view of system operators and undermines the effectiveness of online applications [147].

SCADA units, on the other hand, has widely accepted data quality and over 120,000 units strategically placed across US to ensure full observability and adequate redundancy to identify measurement error [148]. However, due to much slower reporting rate, it is not suitable in the fast inter-area or inter-level data

transmissions. Under such condition, an online voltage control tolerable of slower communication is needed for WECC. The proposed hierarchical voltage control can accommodate to such SCADA based communication.

2.4 Literature Review on Test Systems

The planning case of WECC has around eighteen thousand buses, with the operational West Wide System Model around the same size. Both of them contain more than 3000 generators and many electronic devices. It is thus inefficient for validating the proposed research. Hence, a suitable equivalent system of smaller size that preserves critical information is necessary to serve as the test-bed of the proposed voltage control. This equivalent model needs to represent voltage issue as shown in the detailed planning and operational WECC system.

1) Ultra-Simplified WECC Reduced Models

Simplified WECC systems have been constructed for multiple education and research purposes. For instance, the Western System Coordinated Council (WSCC) 9-bus system, where generations and loads are aggregated into three clusters, serves as a simple multi-machine test bed to run the Matlab-based transient stability analysis [149]. The spring-mass representation of WECC [150] that contains major generation/load areas and HVDC critical interties is used to study the propagation behavior of oscillations [151]. Another ultra-simplified WECC equivalent model is the 4-machine system based on coherent region identification and clustering analysis. This model was created with dynamic reduction and served as the WECC part of the first layout of large scale Testbed [152]. Though small in size and simple in structure, those models represented desired properties of the WECC system and serve the research or educational purposes. However, they do not carry enough details of the system for validating the proposed HVC.

2) PTDF-based WECC Reduced Models

To make the equivalent system more detailed for studies and researches, a Power Flow Transfer Distribution Factor (PTDF) based model reduction was proposed [153] and validated by the WECC planning case. A 180-bus network was obtained via identification of nucleus bus and aggregation of non-nucleus buses. This process merges non-nucleus nodes with their nucleus neighbors and will stop all the buses are categorized as nucleus buses. With the help of DC power flow, the model reduction can be less computationally intensive while retain desired accuracy. It has been proved that this 180-bus equivalent system holds smaller discrepancy with the detailed planning model in terms of branch flow mismatches compared with other PTDF based model reductions [154].

However, due to limitations of DC approximation, this equivalent system fails to address reactive and voltage issues of the original WECC and furthermore, without including a dynamic model reduction in the

PTDF-based method, this 180-bus equivalent network carries only static characteristics and therefore not competent to validate proposed HVC that considers the dynamic security constraints.

3) Utility-initiated WECC Reduced Models

So as to have equivalent models to retain both static and dynamic characteristics, model reduction on both steady-state and dynamic part of the WECC system are carried out by utilities to create their own study cases. As created for planning and operational tasks, those models preserve the majority of networks within the service area of each utility, which is referred to as the study region. A buffer region with fewer details is then created to connect the study region and the rest parts of the system are highly simplified to reduced system size. Equivalent systems constructed using above ideology includes the 7210-bus study model created by BC-hydro [155] and the 1200-bus loop model built by Alberta Electric System Operator (AESO) [156].

The above models successfully supported the routine work in planning and operation of corresponding utilities due to their widely admitted credibility in representations of the actual WECC system in both steady state and dynamics. Nevertheless built to monitor and study the typical service areas governed by BC-hydro and AESO, they fail to thoroughly stress the COI intertie and the California part of the WECC network, which is the critical study area from the perspective of the proposed HVC.

4) Market-Oriented WECC Reduced Model

As the California Independent System Operator (CAISO) facilitates one of the biggest competitive wholesale power markets in US, it built equivalent systems that emphasizes on CA load centers and major generations to support a variety of balancing and ancillary services from congestion management to operating reserves. Such equivalent models are comparably smaller in size such as 225-bus system built for evaluation of market rules [157] and the 240-bus system constructed for market prototype design [58, 158]. However, they are equipped with complete information regarding generation and load at each hour of the year. Sometimes, such data even includes details regarding unit fuel types and planned installation of power station. Thereby archived information could be used to develop yearly operating scenarios and implement wind generation for the proposed HVC, even though those market-oriented reduced systems lack sufficient dynamic modeling to support the deployment of transient security constrained voltage control.

5) HVDC-involved WECC Model Reduction

There are two major two terminal HVDC lines in the WECC system: The pacific intertie (PDCI) from Oregon to Los Angeles and intermountain intertie from Utah to Los Angeles. They relieve the congestion on AC transmission and enhance the transient security. Hence, for simplified systems aiming at event studies, the HVDC connections are often represented via loads and injections or detailed modeling of converters based on the importance of switching actions in corresponding studies. In addition, to complete the simulation of an event, all the remaining units in the reduced systems are equipped with detailed models

on synchronous machines, exciters, Power System Stabilizers (PSS) and sometimes governors for frequency regulation. Equivalent WECC systems built based on above ideology includes the 176-bus model [159] and the 179-bus model [160]. Both of them roughly represents all areas of WECC with the latter containing more sub-transmission level details in California areas.

Due to reasonable modeling of dynamics, those models can support online transient analysis and stability margin prediction [161, 162] which best qualifies for the requirements of the proposed HVC, yet steady-state and dynamic modeling of wind units and multi-terminal HVDC overlay are still in absence to completely fulfill the desired functions of a HVC test system.

6) Summary

A summary of existing equivalent models of WECC is listed in Table 2.6.

Table 2.6 Summary of Existing Reduced WECC Models

Reduction Category	Ultra-Simplified	PTDF-based	Utility-initiated	Market-Oriented	HVDC Involved
Simplified Systems	WSCC 9-bus model	180-bus model	BC-Hydro Study Model	225-bus Evaluation Model	WECC 176-bus Model
	Spring-mass model		AESO Loop Model	240-bus Prototype Model	WECC 179-bus Model
	CURENT Model				
Superiorities	Ultra-simplicity	Enhanced-Credibility	Emphasis on Canada area	Provision of hourly scenarios	Emphasis on COI and PDCI
Limitations	Inadequate details	Lacking Dynamic Modeling	Insufficient details in COI and CA	Lacking Dynamic Modeling	Absence of Wind and HVDC overlay

Considering all the expected properties of the test system for the HVC; it is obvious that a reasonable resolution of system information and full modeling of system dynamics need to be retained. Furthermore, this model shall have a higher stress on the critical study areas from the prospective of the proposed control scheme while roughly representing all parts of the whole WECC system. The WECC 179-bus model is the closest to the needs as it contains all 40 locally serviced power systems of WECC and places higher emphasis on the sub-transmission levels of network along California coastal area. Due to absence of wind modeling and HVDC overlay, it cannot directly serve as the test bed for the proposed control scheme and

that has excluded the candidacy for all the existing equivalent WECC models for validating the proposed HVC. Hence, a new reduced system will be derived in this dissertation to serve such purpose. It is built based on the WECC 179-bus model where scenarios with wind penetration will be generated based on the loading profile associated with the market prototype model and HVDC overlay structure will be established based on a preliminary test on the AC-DC hierarchical transmission structure of WECC

3. Methodology

This Chapter summarizes the kernel of the proposed wide area voltage control. With a hierarchical structure, it manages the overall voltage map under a variety of operating conditions to reinforce the system's resistibility against disturbances and enhance its security margin. As mentioned in Chapter 1, here the security margin refers to the difference between the COI base flow and transfer limit, which is constrained by the WECC TPL standard [51, 52] concerning transient and post-transient voltage and frequency behaviors. The requirement on VAR margin reserve after a contingency is also included. With consideration of above security standards, N-1 contingency screening following the guide of CAISO operating study plan [163] was carried out via repetitive simulations. The study results for each scenario were archived into a database. Then this database was analyzed to find the appropriate formulation of the control objective and constraints. The control problem was then solved by an active-set approach which sought the optimum via linearization and relaxation of constraints.

3.1 Architecture

The hierarchical structure of the proposed control consists of three levels: The tertiary OPF and feedback reference corrector; the secondary OPF and gain control based regulator; the primary unit AVR and wind farm reactive allocation system. While higher level functions are allowed to have longer response time compared with their peers at lower level, different response time is assigned to different control functions within the same level for better coordination. The physical architecture of the proposed hierarchical voltage control scheme consists of three layers like displayed in Fig. 3.1.

3.1.1 Tertiary Level Architecture

With the feature for online deployment, the proposed HVC categorizes all streaming-in scenarios as nominal cases, namely cases captured on top of the hour; and off-nominal cases, namely cases processed between each hour. The nominal cases are used to run the hourly tertiary OPF to maximize the limiting COI transfer capability and settle the initial references regarding to pilot bus voltages. Those voltages are maintained by controllable plants within the regulated region, where reactive variances are picked up by adjusting the terminal outputs of the controllable plants. The system operator may have certain power stations taking more responsibility by increasing the magnitude of the corresponding element of the weighting vector λ. With measurement input on resource limits and the q^{ref} from secondary OPF, the reference value for reactive generation from each plant can be obtained and sent to secondary regulators.

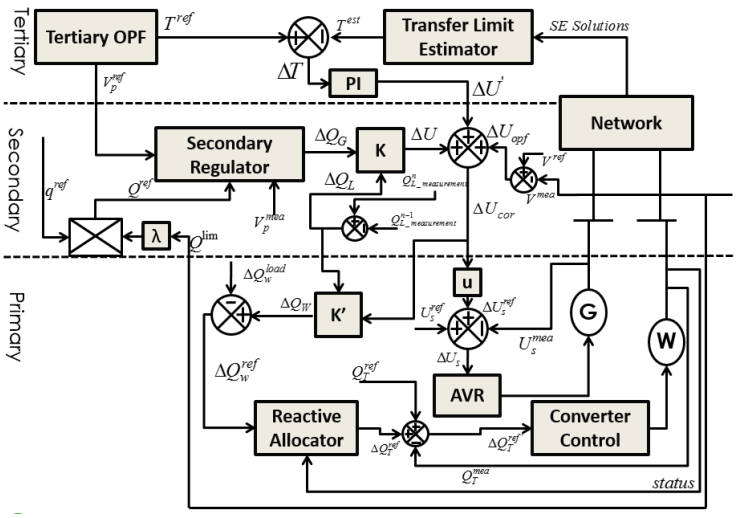

Fig. 3.1 Physical Architecture of the Proposed Hierarchical Voltage Control

In addition to the OPF procedure, the Tertiary Voltage Control (TVC) provides another function to generate correction signals to Secondary Voltage Control (SVC) output as the operating conditions of off-nominal scenarios slowly drifting away from the point where the secondary OPF was carried out and the OPF-computed references may lead to inappropriate plant POI set-points. Due to the utilization of full-topology operational model at control center [164] and minute based real-time state estimation [165], SE solutions can be the control input, based on which, an approximation of COI transfer capacity will be computed and compared with the hourly obtained reference transfer limit from tertiary OPF. If there is a difference between the two, a nonzero correction signal represented will be added to the secondary control output. The reference correction loop changes SVC output at the rate of online state estimation, this requires it to function as fast as the secondary regulator as shown in Fig 3.2.

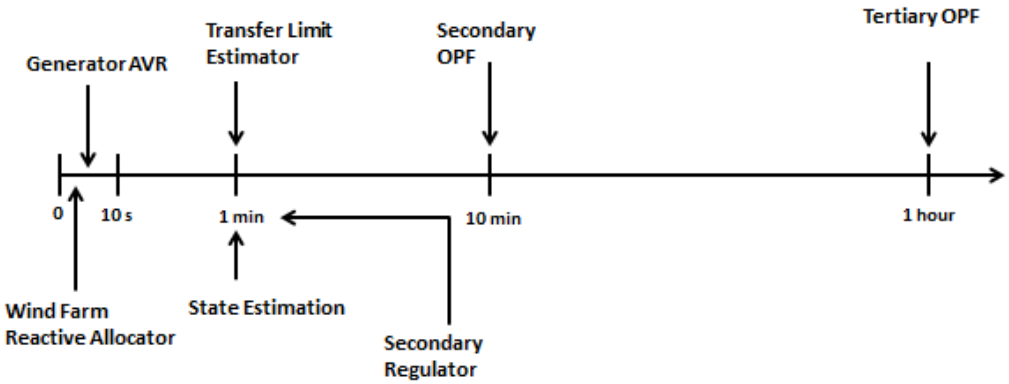

Fig. 3.2 Controller Time Frames

The implementation of the feedback reference correction took advantage of the deployment of full-topology operational model and fast online state estimation in the control center. With its help, the secondary level control output is able to reflect even small and short-term variances in the system conditions. Meanwhile, the secondary regulation in different control areas will be coordinated under the common objective of maximizing COI transfer limit.

3.1.2 Secondary Level Architecture

The secondary regulation is processed at a 1-minute interval. It feeds in the reference value regarding to pilot bus voltage and plant reactive generation, which are computed via tertiary OPF and secondary OPF respectively. Since the secondary OPF converges to a solution where the plant-level reactive output are most appropriately adjusted to maintain pilot bus voltages, the references input to secondary regulator are coordinated by this solution. Hence, it is easy to obtain reactive output variance for each plant noted as ΔQ. With changes on reactive loading levels in the system known via subtraction of two successive measurement recordings, the expected plant terminal voltage set-point variance ΔU can be computed via linearization of power flow equations. Here, the plant terminal is assumed as its point of interconnection. However, this ΔU may not be the best to reach for maximized transfer limit. Therefore a correction signal $\Delta U'$ based on the evaluation of COI transfer capacity under current operating condition is given to amend the SVC output and subsequently, after combination with the secondary OPF-solved reference, the corrected plant voltage set-point variance ΔU_{cor} is input to primary level. Such amendment may contribute to the reactive share of each plant deviating slightly from the reference value and a decreased accuracy of pilot bus voltage following its references. Nevertheless, the overall control objective as to maximize the transfer capacity shall be satisfied. All measurement input to the secondary regulator regarding to pilot node information and reactive load levels need to be coordinated with SVC actions, i.e. their shall be reported at the initialization of each secondary level functions and their report rate should be no slower than 1 record/minute, which is completely manageable by SCADA.

With the corrected set-point variances on plant terminal voltages distributed to both non-renewable power stations and wind farms. The SVC has involved wind turbines into the voltage/VAR regulation of the system via properly utilizing their limited reactive capabilities. Meanwhile, by introduction of q^{ref}, it takes the reactive limitations of both types of units into consideration and greatly prevents over excitations caused by too much required reactive outputs assigned from secondary level. This has enhanced the solution quality of the proposed control.

3.1.3 Primary Level Architecture

The primary level controls act within seconds at the signals from SVC to adjust excitation of non-renewable units and allocate reactive output to wind turbines. Here for non-renewable plants, ΔU_{cor} can be transformed into variance on stator voltage set-point via coefficient vector μ denoting the voltage drop ratio due to transformer impedance. Subsequently, this variance will be added to the intial reference value on stator voltage set-point where the measured stator voltage is subtracted to generate the stator voltage variance that feeds into the AVR. The AVR can then take actions to compensate the variances and maintain unit terminal voltages against small but random disturbances. For wind farms, as all units are operated in constant Q control mode in this dissertation, the terminal voltage variance needs to be reversely transformed into the reactive output variance, which will be used to compute the new set-point of wind farm reactive generation. The expected plant-level generation will then be proportionally allocated to all the in-service turbines within the wind farm [166]. As the volatility of wind speed makes the status of each turbine subject to frequent changes, the reactive allocator must be aware of such changes and assign appropriate share to each of the online turbines.

Ideally, at the end of each primary control loop, the variance in unit stator voltages and wind farm reactive references are to be fully compensated so that the POI voltages of non-renewable plants and the reactive outputs from wind farms can be adjusted to counteract the wind uncertainties. This requires all the measurement input at this level to be completed within seconds. Since wide area communications are not necessary, internal data exchange channels of power stations can be taken advantage of. As wind farms are usually interconnected to transmission grid with a fixed power factor, they will have higher potentials in reactive provision and absorbance if with higher real power productions. However, when encountering extreme loading conditions, this potential will be exhausted faster than non-renewable power stations, which makes high wind penetration detrimental to system security and a constraint bounding the feasibility region of the proposed HVC.

3.2 Formulations

The proposed control is formulated as a three level OPF with the objective to maximize COI transfer limit, minimize pilot bus voltage deviations and follow POI voltage set-points respectively. The constraints are either explicitly expressed or implicitly represented as a form of linear regression. The OPFs are carried out in near-real-time to provide guidance to the control actions in each level. Tweaking of objective functions are some time necessary considering evolving system conditions.

3.2.1 Formulation of Tertiary OPF

The formulation of the tertiary OPF starts with representation of COI transfer limit and WECC security standards in terms of system steady-state voltages. While COI transfer limit is the only control objective we have, WECC security standards contain multiple constraints regarding to system performances. The security standards has classified all contingencies into four categories noted as A, B, C, D, where category A includes normal operating conditions, category B consists of contingencies with loss of one element, category C is made up of contingencies with loss of multiple elements and in category D, are contingencies causing cascading failure. Due to simplicity on distribution level and lack of Remedial Action Scheme (RAS) implementations in the test system, this dissertation only involves events in category A and B for security margin evaluation, namely only normal conditions and N-1 contingencies are studied. The system security constraints are expressed by WECC criterion [42] shown in Table 3.1 and enforced in the tertiary level OPF.

Table 3.1 Planning Criterion on Category A and B Events

	Transient period 20s		Post Transient
	Voltage	Frequency	
Category A	Nothing in addition to NERC		
Category B	Load bus Volt. >=0.75, Non-load bus Volt. >=0.70 Load bus Volt. <=0.80 for less than 20 cycles. 500kV bus Volt. dip<=4%[163]	Load bus Frequency <=59.6Hz for less than 6 cycles	VAR margin positive at 105% loading level of CA load center[163] Southern California Edison (SCE) System Volt. dip<=7%[163], other buses Volt. Dip<=5%

CAISO has issued additional security criteria in its operating limit study[163] as noted in the above table. Such criteria will also be included in the tertiary OPF formulation. Thereby the tertiary OPF will have 6 constraints regarding to voltage behavior, 1 constraint regarding to frequency dip and 1 constraint regarding to allowable margin computed via Q-V analysis according to the guide on WECC/NERC planning on voltage support and reactive power [167]. All constraints functions expressing WECC security standards in the tertiary OPF are formulated by mapping of static bus voltage to security boundaries represented as limitations on voltages, frequency and VAR margin. Such mappings are obtained via

regression methods based on pattern recognition. The formulation of constraint function incorporating WECC security standards are listed from (3-1) to (3-8)

$$V\left(V^{ld}\right) \geq 0.75 \tag{3-1}$$

$$V\left(V^{Nld}\right) \geq 0.70 \tag{3-2}$$

$$T_v\left(V^{ld}\right) \leq 0.333 \tag{3-3}$$

$$V\left(V^{hv}\right) \geq 0.96 \tag{3-4}$$

$$V\left(V^{cse}\right) \geq 0.93 \tag{3-5}$$

$$V\left(V^{Ncse}\right) \geq 0.95 \tag{3-6}$$

$$T_f\left(V^{ld}\right) \leq 0.1 \tag{3-7}$$

$$Q(V) \geq 0 \tag{3-8}$$

Where $V(\cdot)$ are the projection of steady-state voltage to limits on the magnitude of voltage dip during transient and post-transient periods, $T_v(\cdot)$ and $T_f(\cdot)$ denotes the limits on the duration voltage and frequency dip lower than certain thresholds and $Q(\cdot)$ represents the minimum VAR margin computed with all selected contingencies.

The same approach is used in the formulation of objective function to maximize COI transfer limit as shown in (3-9). The transfer limit is considered as an index denoting the security limit of a certain scenario. This formulation is also used in the transfer limit estimation to amend secondary regulation outputs.

$$\max \quad T = f(V) \tag{3-9}$$

Additionally, load flow constraints and voltage/VAR bounds are added to make sure the optimal solution for the proposed control are found where all system attributes locate within pre-defined limits. This means all PV voltages need to be within [0.98, 1.10], every PQ bus voltage is supposed to be within [0.98, 1.17] and all plants reactive generation should not exceed the upper and lower bounds. The upper limits of the PQ bus voltage are higher than usual due to lack of structural support from the sub-transmission networks in the test system.

$$P_i - \sum_{j=1}^{n} |V_i||V_j|\left[G_{ij}\cos\left(\delta_i - \delta_j\right) + B_{ij}\sin\left(\delta_i - \delta_j\right)\right] = 0 \tag{3-10}$$

$$Q_i - \sum_{j=1}^{n} |V_i||V_j|\left[G_{ij}\sin\left(\delta_i - \delta_j\right) - B_{ij}\cos\left(\delta_i - \delta_j\right)\right] = 0 \tag{3-11}$$

$$V^{\min} \le V \le V^{\max} \tag{3-12}$$

$$Q^{\min} \le Q \le Q^{\max} \tag{3-13}$$

For all above implicit representation of OPF objective and constraints, V denotes the voltage matrix where the row number corresponds to simulated scenarios and the column number corresponds to buses. Considering the size of the WECC system and huge amount of data archived for pattern recognition, the voltage matrix has a great dimension that makes the regression of OPF constraint functions computationally difficult. Hence dimension reduction is necessary. It is clear that every bus reflects certain local information that contributes to the transfer limit and security boundaries. Therefore none of them shall be arbitrarily removed. Meanwhile, those voltages are correlated with each other so the sampling matrix V is subject to information overlapping, which will aggravate the complexity of data fitting. In order to clarify the correlation among variables and sort out critical information, the Principal Component Analysis (PCA) [168] is carried out.

The PCA starts with standardizing the sampling matrix V to have column-wise zero empirical mean and unit standard deviation.

$$X_{ij} = \frac{V_{ij} - \mu}{\sqrt{\frac{1}{n-1}\sum_{i=1}^{n}\left(V_{ij} - \mu\right)^2}} \tag{3-14}$$

$$\mu = \frac{\sum_{i=1}^{n} V_{ij}}{n} \tag{3-15}$$

where X is a centered, scaled version of V with n by m dimension where n corresponds to number of observations and m corresponds to number of variables. The covariance matrix of X is then computed as

$$C = \begin{bmatrix} \operatorname{cov}(x_1,x_1) & \operatorname{cov}(x_1,x_2) & \cdots & \operatorname{cov}(x_1,x_m) \\ \operatorname{cov}(x_2,x_1) & \operatorname{cov}(x_2,x_2) & \cdots & \operatorname{cov}(x_2,x_m) \\ \vdots & \vdots & \ddots & \vdots \\ \operatorname{cov}(x_m,x_1) & \operatorname{cov}(x_m,x_2) & \cdots & \operatorname{cov}(x_m,x_m) \end{bmatrix} \tag{3-16}$$

$$X = \begin{bmatrix} x_1 & x_2 & \cdots & x_m \end{bmatrix} \tag{3-17}$$

$$\mathrm{cov}(X_i, X_j) = \frac{1}{n-1}\sum_{k=1}^{n} x_{ki} \cdot x_{kj} - \left(\frac{1}{n-1}\sum_{k=1}^{n} x_{ki}\right) \cdot \left(\frac{1}{n-1}\sum_{k=1}^{n} x_{kj}\right) \tag{3-18}$$

The total number of m eigenvalue of the covariance matrix *C* is while solving (3-19).

$$\begin{vmatrix} \lambda - C_{11} & -C_{12} & \cdots & -C_{1m} \\ -C_{21} & \lambda - C_{22} & \cdots & -C_{2m} \\ \vdots & \vdots & \ddots & \vdots \\ -C_{m1} & -C_{m2} & \cdots & \lambda - C_{mm} \end{vmatrix} = 0 \tag{3-19}$$

And the solution of (3-19) gives $\lambda = \begin{bmatrix} \lambda_1 & \lambda_2 & \cdots & \lambda_m \end{bmatrix}$ where λ_i is the i^{th} largest eigenvalue for matrix *C*. The magnitude of each element in λ denotes the projection of *C* on the corresponding orthonormal base, i.e. eigenvector. Hence the larger the magnitude of λ_i, the more information will be projected on its corresponding eigenvector. Thus, by preserving the first several large elements in vector λ, we can have the most of information represented in the principal component space via a linear transformation formed by the corresponded eigenvectors. Usually in statistics, if the preserved components cumulatively explained at least 85% of the total variance, it is considered that the majority of the information in the original sampling dataset has been captured [169, 170]. The percentage of cumulative contribution can be evaluated using the eigenvalues of the covariance matrix *C*. Assuming the required amount of contribution can be reached by preserving the first k elements in λ, namely:

$$P = 100\% \cdot \frac{\sum_{i=1}^{k} \lambda_i}{\sum_{i=1}^{m} \lambda_i} \geq 0.85 \tag{3-20}$$

The corresponding eigenvectors of the preserved eigenvalues are computed to form the loading matrix *W* via (3-21) and (3-22).

$$\begin{bmatrix} \lambda_i - C_{11} & -C_{12} & \cdots & -C_{1m} \\ -C_{21} & \lambda_i - C_{22} & \cdots & -C_{2m} \\ \vdots & \vdots & \ddots & \vdots \\ -C_{m1} & -C_{m2} & \cdots & \lambda_i - C_{mm} \end{bmatrix} \cdot w_i = 0 \tag{3-21}$$

$$W = \begin{bmatrix} w_1 & w_2 & \cdots & w_k \end{bmatrix} \tag{3-22}$$

Then the score matrix S denoting the representation of original dataset X in the principal component space can be written as:

$$S = X \cdot W \tag{3-23}$$

S is an n by k matrix where the number of variables is reduced but the majority of information is retained. It can then be used in the regression analysis to formulate the objective and part of constraint functions for the tertiary OPF. To carry out the regression, we use F to denote the raw data on security limit and boundaries which are assumed to have a linear relationship with static voltages of the system.

$$F = V \cdot A + e \tag{3-24}$$

Where A and e are both vectors, whose elements depend on the decomposition of F and V in terms of the score matrix S.

$$\begin{bmatrix} X_{11} & X_{12} & \cdots & X_{1m} \\ X_{21} & X_{22} & \cdots & X_{2m} \\ \vdots & \vdots & \ddots & \vdots \\ X_{n1} & X_{n2} & \cdots & X_{nm} \end{bmatrix} = \begin{bmatrix} 1 & V_{11} & V_{12} & \cdots & V_{1m} \\ 1 & V_{21} & V_{22} & \cdots & V_{2m} \\ \vdots & \vdots & \vdots & \ddots & \vdots \\ 1 & V_{n1} & V_{n2} & \cdots & V_{nm} \end{bmatrix} \cdot \begin{bmatrix} Z_{11} & Z_{12} & \cdots & Z_{1,m} \\ Z_{21} & Z_{22} & \cdots & Z_{2m} \\ \vdots & \vdots & \ddots & \vdots \\ Z_{m+1,1} & Z_{m+1,2} & \cdots & Z_{m+1,m} \end{bmatrix} \tag{3-25}$$

$$\begin{bmatrix} F_{11} \\ F_{21} \\ \vdots \\ F_{1n} \end{bmatrix} = \begin{bmatrix} 1 & S_{11} & S_{12} & \cdots & S_{1k} \\ 1 & S_{21} & S_{22} & \cdots & S_{2k} \\ \vdots & \vdots & \vdots & \ddots & \vdots \\ 1 & S_{n1} & S_{n2} & \cdots & S_{nk} \end{bmatrix} \cdot \begin{bmatrix} B_{11} \\ B_{21} \\ \vdots \\ B_{k+1,1} \end{bmatrix} \tag{3-26}$$

$$\begin{bmatrix} O_{11} \\ O_{21} \\ \vdots \\ O_{1,m+1} \end{bmatrix} = \begin{bmatrix} Z_{11} & Z_{12} & \cdots & Z_{1,m} \\ Z_{21} & Z_{22} & \cdots & Z_{2m} \\ \vdots & \vdots & \ddots & \vdots \\ Z_{m+1,1} & Z_{m+1,2} & \cdots & Z_{m+1,m} \end{bmatrix} \cdot \begin{bmatrix} W_{11} & W_{12} & \cdots & W_{1,k} \\ W_{21} & W_{22} & \cdots & W_{2k} \\ \vdots & \vdots & \ddots & \vdots \\ W_{m,1} & W_{m,2} & \cdots & W_{m+1,k} \end{bmatrix} \cdot \begin{bmatrix} B_{21} \\ B_{31} \\ \vdots \\ B_{k+1,1} \end{bmatrix} \tag{3-27}$$

$$A_{ij} = O_{i+1,j} \tag{3-28}$$

$$e_{ij} = O_{11} + B_{11} \tag{3-29}$$

The above regression method takes advantage of the PCA to simplify computation of coefficients. With a linear representation of the relationship between static voltage and security indices, it is easy to implement and efficient in calculation. Its accuracy in terms of Mean Square Error (MSE) and Mean Error Rate (MER) will be compared with a feed-forward ANN method in the next Chapter.

With objective and constraints regarding to dynamic security standards represented via PCA-based linear regression. The formulation of the tertiary OPF is completed. With previously archived data for curve fitting, this PCA-based regression method allows main offline study results to be extracted and organized, thus enabling one to infer knowledge about new cases without cumbersome online transient security analysis. The formulation of OPF resulted from PCA-based regression is a one-time task that would only require modification at significant structural changes of the power grid, a situation where the previously archived data no longer accurately describe the relationships between system variables and security indices.

3.2.2 Formulation of Secondary Regulation

With reference input from tertiary OPF, the secondary regulation minimizes the differences between measured value and the expected set-points on pilot bus voltages by proportionally distributing the task of reactive provision to all controllable power stations according to their capabilities. Initially, as the operating conditions deviates little from the nominal point, such way of distribution would draw the pilot bus voltages fairly close to the references.

$$Q_{\sup}^{ref} = q^{ref} \cdot Q^{\lim} \tag{3-30}$$

Then the desired reactive injection variance at POI is computed as the differences between the supply variances and load variances at the interconnection point:

$$\Delta Q_G = Q_{\sup}^{ref} - Q_{\sup}^{mea} + \Delta Q^{load} \tag{3-31}$$

As the correction signal is incorporated as plant POI voltage variance, the output from secondary regulator needs to be in forms of voltage. Hence the transformation between ΔQ and ΔU is processed via linearization of nodal power equation.

$$Q_i = V_i \sum_{j \in i} V_j \left(G_{ij} \sin\theta_{ij} - B_{ij} \cos\theta_{ij} \right) \tag{3-32}$$

Where V_i is the POI voltage and V_j are the voltages of all buses connected to the POI. G_{ij} and B_{ij} are equivalent conductance and susceptance of branches connecting buses i and j. θ_{ij} represents the phase angle difference between nodes i and j; usually for transmission network, the line conductance can be neglected and the phase angle difference between the nodes at two ends of a branch are small enough so that:

$$\sin\theta_{ij} = \theta_{ij} \tag{3-33}$$

$$\cos\theta_{ij} = 0 \tag{3-34}$$

By regarding POI voltage as 1.0 per unit, the reactive power injected to grid can be written as:

$$Q_i = -\sum_{j \in i} B_{ij} V_j \tag{3-35}$$

Expand above equation according to Taylor series while eliminating higher order terms, we can obtain the representation of perturbed reactive output regarding to voltage variance.

$$\Delta Q_i = -\sum_{j \in i} B_{ij} \Delta V_j \tag{3-36}$$

Since there are multiple plants who's POI are connected to bunch of PQ buses, equation 3.34 needs to be re-written in the matrix form with partitioning between PV nodes and PQ nodes. Here we considered the PV nodes are the points of interconnections of power stations and PQ nodes are the load buses.

$$\begin{bmatrix} \Delta V_L \\ \Delta V_G \end{bmatrix} = -\begin{bmatrix} B_{LL} & B_{LG} \\ B_{GL} & B_{GG} \end{bmatrix}^{-1} \cdot \begin{bmatrix} \Delta Q_L \\ \Delta Q_G \end{bmatrix} \tag{3-37}$$

Here ΔV_L, ΔV_P, ΔQ_L and ΔQ_P are unknown nodal voltage variances and known reactive injection variance at load buses and POIs. B represents the susceptance matrix where elements correspond to buses non-electrically linked to POIs are eliminated. By assuming:

$$-\begin{bmatrix} B_{LL} & B_{LG} \\ B_{GL} & B_{GG} \end{bmatrix}^{-1} = \begin{bmatrix} R_{LL} & R_{LG} \\ R_{GL} & R_{GG} \end{bmatrix} \tag{3-38}$$

The voltage change at POI can be computed as:

$$\Delta V_G = \Delta U = R_{GL}\Delta Q_L + R_{GG}\Delta Q_G = K_1 \Delta Q_L + K_2 \Delta Q_G \tag{3-39}$$

Where K_1 and K_2 are coefficients associated with the gain control in the secondary level that constitutes the proposed physical architecture of the proposed HVC. This ΔU is subject to the correction signal $\Delta U'$ generated from comparison between the reference and estimated transfer limit when operation condition evolves from the nominal point. Eventually, the set-point variances for plant terminal bus are the summation of forward calculation and the feedback correction.

$$\Delta V^{regulation} = \Delta U + \Delta U' = \Delta U + A_G^{-1}\left(T^{ref} - T^{est} \right) \tag{3-40}$$

In (3-40), A_G is the set of coefficients corresponds to controllable plant terminal voltages in linear regression (3-24). The signal of ΔV^{reg} addresses the short-term variances in system condition within this regulated area. It is a supplement to the secondary OPF, which is to handle the slow variances.

The control actions described above are complementary to the secondary OPF that computes POI set-point value V_{ref} for each off-nominal scenario that streams in every 10 minutes. Due to introduction of the reference feedback term, the solutions of the secondary OPF must lead to the minimized summation of the pilot bus voltage variances and transfer limit deviations. Hereby, a Pareto optimum point is found as the solution. This point may not yield pilot bus voltages that exactly follow the references from the tertiary level but could retain the effect of wide area voltage/VAR management when operating conditions evolves. The objective function of the secondary OPF is formulated as a weighted least square programming.

$$\min \ \lambda_T \left\| T^{ref} - T^{est} \right\|^2 + \lambda_V \left\| V_p^{ref} - V_p^{mea} \right\|^2 \tag{3-41}$$

Where the first term is to coordinate with the feedback loop for calculating correction signal $\Delta U'$ and the second term corresponds to the forward path for obtaining initial POI set-point variance ΔU. The secondary OPF aims to minimize both terms so that a satisfactory transfer capability of the COI intertie can be maintained for off-nominal scenarios. During the computation of optimal solution, wind farms are treated separately from non-renewable plants due to their tendency towards frequent output changes. Furthermore, the sensitivity matrices are introduced to link the adjustment of pilot bus voltages between two successive computing steps with POI voltage deviations ΔV so that the solution to the OPF would generate POI voltage references that best practice the ideology of the secondary regulation. With all above included, the secondary OPF is implemented as:

$$Min \left\{ \lambda_V \sum_{i \in \alpha P} \left\| V_{p_i}^{ref} - V_{p_i}^{cal}(t) \right\|^2 + \lambda_T \left\| \left(T^{ref} - T^{cal}(t) \right) \right\|^2 \right\} \tag{3-42}$$

$$V_{p_i}^{cal}\left(t_0\right) = V_{p_i}^{mea} \tag{3-43}$$

$$T^{cal}\left(t_0\right) = T^{est} \tag{3-44}$$

$$V_{p_i}^{cal}(t) = V_{p_i}^{cal}(t-1) + \sum_{k \in G_C} C_{v_i}^k (t-1) \Delta V_G^k (t-1) \tag{3-45}$$

$$T^{cal}(t) = T^{cal}(t-1) + \sum_{k \in G_C} C_t^k(t-1)\Delta V_G^k(t-1) \tag{3-46}$$

Where G_c denotes the set of controllable plants. λ_V and λ_T are weighting factors deciding which term shall be prioritized in the minimization. $C_{v_i}^k$ is the sensitivity matrices element linking the voltage variation at the i^{th} pilot bus to the voltage variation at the k^{th} power station POI. C_t^k links the deviation of COI transfer limit to the voltage variation at the k^{th} POI. Since the sensitivity matrices are calculated using step changes, their value evolves with the iterations to adjust the pilot bus voltage and estimated transfer limit, and eventually, push (3-42) to optimum.

$$C_{v_i}^k(t) = \frac{\Delta V_{p_i}^{mea}(t)}{\Delta V_G^k(t)},\ k \in G_C \tag{3-47}$$

$$C_t^k(t) = \frac{\Delta T^{est}(t)}{\Delta V_G^k(t)},\ k \in G_C \tag{3-48}$$

Additionally, voltages of the pilot bus and POIs need to be maintained within given boundaries at each search step. Thereby, they are examined by constraints functions whenever there applies a step change. Here due to two different types of controls, the wind farms and conventional generation stations are treated separately.

$$0.98 \le V_{p_i}^{cal}(t) + C_{v_i}^k(t)\Delta V_G^k(t) \le 1.17 \tag{3-49}$$

$$0.98 \le V_G^k(t) + \Delta V_G^k(t) \le 1.1 \tag{3-50}$$

Constraints (3-10) and (3-11) are also added to make sure the optimum point has convergent load flow solution.

The secondary OPF corresponds to the forward calculation of initial signal as well as the feedback correction signal of the POI voltage variances. Like most constrained multi-objective optimization, the secondary OPF is formulated and solved using a deterministic method, where the initial set of unknown variables is close enough to the optimal set. This is considered realistic while there is no sudden and dramatic alteration of system conditions due to significant event [171]. Complex and highly meshed transmission network makes local management inefficient.

This management approach is effective as long as wind farms don't exhaust the reactive reserve in the system. Otherwise, for both secondary OPF and regulator, the emphasis on pilot bus voltages will be laid back and a higher weighting factor will be assigned to minimize the transfer limit difference. In this way,

all nodes in the system area allowed with more freedom in voltage settlement to bring up the transfer capability and non-renewable units can stretch their potential in providing reactive support. The solution of the secondary OPF minus the measured POI voltage is added onto the output of secondary regulation. Then this compound signal will be used to guide the actions of the PVC, where unit AVR and turbine controllers are to be leveraged to regulate POI voltages and realize the desired voltage distribution designed by higher level regulations.

3.2.3 Formulation of the Primary Control Actions

The PVC takes the POI voltage variance ΔU_{cor} from secondary level to generate stator voltage variance that feeds into each non-renewable unit and reactive output reference that regulates the wind turbines. A plant level OPF is formulated and processed every minute to dispatch the initial set-points on unit stator voltage and wind turbine reactive provision.

$$Min \left\{ \left\| V^{ref} - V^{mea} \right\|^2 \right\} \tag{3-51}$$

Where V^{ref} and V^{mea} denote reference and measured value of plant POI voltage with V^{ref} as the solution from the secondary OPF. Solving (3-51) would yield a set of desired unit stator voltages and wind turbine reactive outputs to be assigned to corresponding controllers. However, before eventually input to AVR and turbine converters, they need to be compounded by corrective signals from the SVC. To realize this, the primary control is partitioned into two parts, one for implementation of the non-renewable unit regulation and the other for deployment of the wind turbine management.

For non-renewable unit regulation, it is known that there might be multiple units supplying power to the POI via transformers and other electric conductors. Therefore a participation vector μ is introduced to separate the changes of voltage drop on electric conductors from the POI voltage variance. Followed by this, the stator voltage variance of each unit can be computed with input on current measured stator voltage U_S^{mea} and the stator voltage reference U_S^{ref} settled by the plant level OPF.

$$\Delta V_j \cdot u_i + U_{S_i}^{ref} - U_{S_i}^{mea} = \Delta U_{S_i}, \ \ i \in U_C, \ \ j \in G_C \tag{3-52}$$

Here U_c is a set of indices of units inside the j^{th} plant. The corrective signal ΔU_S^{ref} from SVC addresses the desired stator voltage set-point change due to system variances. In the idea situation, $U_{S_i}^{mea}$ shall always

be driven closely to its reference at the end of each primary control cycle, where the terminal voltages of each unit can be adjusted appropriately to deal with local disturbances.

For wind turbine management, as operated in constant Q control mode, the adjustment of wind turbine shall be realized through allocation of reference reactive output. The procedure starts with transformation of voltage variance signal to reactive variance signal:

$$\begin{bmatrix} \Delta Q_L \\ \Delta Q_W \end{bmatrix} = -\begin{bmatrix} B_{LL} & B_{LG} \\ B_{GL} & B_{GG} \end{bmatrix} \cdot \begin{bmatrix} \Delta V_L \\ \Delta V_G \end{bmatrix} \tag{3-53}$$

With ΔQ_L and ΔV_G known as inputs from secondary level regarding to variances on reactive loading and wind farm POI voltage and elements in susceptance matrix B non-relevant to wind farm POIs truncated, the reactive injection variance at the wind farm can be calculated as:

$$\Delta Q_W = -\left(B_{GL}\Delta V_L + B_{GG}\Delta V_G\right) \tag{3-54}$$

Where ΔV_L can be represented in forms of ΔQ_L, B_{LL} and B_{LG}:

$$\Delta V_L = -B_{LL}^{-1}\left(\Delta Q_L + B_{LG}\Delta V_G\right) \tag{3-55}$$

Substitute (3-55) into (3-53) to replace ΔV_L, we can obtain the parameters of the gain controller in the primary level.

$$\Delta Q_W = B_{GL}B_{LL}^{-1}\Delta Q_L + \left(B_{GL}B_{LL}^{-1}B_{LG} - B_{GG}\right)\Delta V_G = K_1'\Delta Q_L + K_2'\Delta V_G \tag{3-56}$$

K_1' and K_2' are the controller gain and with the wind farm reactive loading variance subtracted from ΔQ_W, the variance on the expected wind farm total reactive output is computed and divided for each online wind unit. Before assigning to each turbine, the variance is incorporated with the deviation between initial set-point Q_T^{ref} and the measured turbine reactive output Q_T^{mea} to obtain the final adjustment on the settlement of reactive reference. This adjustment is then input to the turbine electric controller to modify the rotor side reactive currents.

The allocation of reactive power to each turbine must take in account of their reactive capability, which is proportional to their capacity since they are all DFIG units with fixed power factor. Hereby, turbines with higher capacity have more potential in reactive provision and absorbance for the proposed control to take advantage of. They are then appointed with more responsibility in supporting the system.

$$\frac{Q_{T_i}^{ref} + \Delta Q_{T_i}^{ref}}{\sum_{i \in G_{w\_online}} Q_{T_i}^{ref} + \Delta Q_{T_i}^{ref}} = \frac{S_i}{\sum_{i \in G_{w\_online}} S_i} \tag{3-57}$$

In (3-57), ΔQ_T^{ref} is computed from ΔQ_w^{ref}, which is a corrective signal to counteract wind uncertainties. It shall increase the set-point on plant level reactive output when wind blows stronger and more turbines are switched into service, and decrease the set-point while wind speed drops and downstream units are turned off. In case of large portion of turbines offline and this wind farm is not able to provide the required amount of reactive power even with the help of the corrective signal, the system operator will have the wind farm disconnect from the transmission network. Thereby, this plant does not participate in the proposed HVC and its generation would be picked up by adjacent non-renewable power stations, which has a higher capability in providing reactive support.

The layout of PVC has sufficiently made use of the reactive resources in the system by exploiting wind farm reactive potentials. Hence it has mitigated the reactive deficiency due to massive replacement of conventional units with wind turbines. However, because of the limited reactive capability of wind units, they would fail to provide adequate reactive support in situations of extreme loading conditions associated with high wind penetration, where the PVC would cease to live up to expectation and the performance of the proposed HVC shall be less satisfactory. This dissertation will discuss the boundary conditions in terms of loading level and wind penetration under which the HVC would still be functional.

3.3 Solution

The tertiary and Secondary OPF in this dissertation are solved by constraints relaxation, where active-set algorithm is used to remove inactive constraints at each iterates. The definition of inactive constraints can be illustrated by a general OPF problem.

$$\begin{aligned} &\underset{x}{Min}\ f(x) \\ &subject\ to \\ &\quad G_i(x) = 0 \quad i = 1, \cdots m_e \\ &\quad G_i(x) \le 0 \quad i = 1, \cdots m \end{aligned} \tag{3-58}$$

Given a point x inside the feasible region defined by the constraint functions in (3-58), a constraint $G_i(x) \le 0$ is called active at x if $G_i(x) = 0$ and inactive at x if $G_i(x) < 0$. Equality constraints are always active. The active set at x is made up of those constraints $G_i(x)$ that are active at the current point [172].

As an upgraded from the simplex method, the active set algorithm applies similar mechanism in solving a nonlinear program. It gives a subset of inequality constraints to watch while searching for the optimum, which reduces the complexity of the search. Alike the simplex method, the active-set algorithm will direct the search along the boundary of the feasibility region until the optimum point is achieved. The active-set algorithm has ensured a feasible solution shall always be obtained even if the search procedure stops prematurely. The drawback is that a feasible starting point must be guaranteed for this algorithm to function properly. The search of the feasible starting point at the very beginning of solving the nonlinear optimization is completed by obtaining a load-flow solvable and strictly dynamic secure case via a steady-state optimal reactive power dispatch, which will be emphasized in Chapter 5. In case of marginal security, a feasibility search is applied to look for an appropriate initial start as discussed later in this section.

The active-set algorithm starts with creating a working set of active inequality constraints at the starting point. This working set is subject to change as the search for optimum goes on. The achievement of the optimum means the working set equals to the active set of the optimum point, which is detectable by examining the Lagrange multiplies λ for all active constraints at the current iteration. In order to launch the procedure on the tertiary and secondary OPF described in last section, the KKT equations are written where the OPFs are treated as general optimization form in (3-58).

$$\begin{aligned} &\nabla f\left(x^*\right)+\sum_{i=1}^{m}\lambda_i\cdot\nabla G_i\left(x^*\right)=0 \\ &\lambda_i\cdot\nabla G_i\left(x^*\right)=0,\ i=1,\cdots m_e \\ &\lambda_i\geq 0,\ i=m_e+1,\cdots m \end{aligned} \tag{3-59}$$

Since the equality constraints contains the AC load-flow equations, both the tertiary and secondary OPF problem are not convex. Therefore satisfying (3-58) can only ensure local optimum. The first equation in (3-58) describes a canceling of the gradients between the objective function and the active constraints at the solution point, where the Lagrange multipliers are necessary to balance the deviations in the magnitude of the objective function and constraint gradients. Because only active constraints need to be included in this cancelling operation, inactive constraints are given Lagrange multipliers equal to 0. The solution of the KKT is necessary to find the optimum, where the Lagrange multipliers are to be computed directly via constrained quasi-Newton method. This method allows the original optimization to be partitioned into Quadratic Programing (QP) sub-problems, which are formulated based on a quadratic approximation of the Lagrange function of (3-58) [173-176].

$$L(x,\lambda)=f(x)+\sum_{i=1}^{m}\lambda_i\cdot g_i(x) \tag{3-60}$$

Assuming bound constraints in the general optimization problem are expressed as inequality constraints, the QP sub-problem can be obtained by linearizing the nonlinear constraints [177].

$$\begin{aligned} &\underset{d\in\Re n}{Min}\ \frac{1}{2}d^T H_k d+\nabla f\left(x_k\right)^T d \\ &\nabla g_i\left(x_k\right)^T d+g_i\left(x_k\right)=0\ i=1,\cdots m_e \\ &\nabla g_i\left(x_k\right)^T d+g_i\left(x_k\right)\le 0\ i=m_e+1,\cdots m \end{aligned} \tag{3-61}$$

Where H_k is a positive definite approximation of the hessian matrix of (3-62), which is subject to updating at each search step.

$$\begin{aligned} &H_{k+1}=H_k+\frac{q_k q_k^T}{q_k^T s_k}-\frac{H_k^T s_k^T s_k H_k}{s_k^T H_k s_k} \\ &s_k=x_{k+1}-x_k \\ &q_k=\left(\nabla f\left(x_{k+1}\right)+\sum_{i=1}^{m}\lambda_i\cdot\nabla g_i\left(x_{k+1}\right)\right)-\left(\nabla f\left(x_k\right)+\sum_{i=1}^{m}\lambda_i\cdot\nabla g_i\left(x_k\right)\right) \end{aligned} \tag{3-63}$$

By assuming X_k as constant, $\nabla f\left(x_k\right)^T$, $\nabla g_i\left(x_k\right)^T$ and $g_i\left(x_k\right)$ can be represented as c^T, A and b respectively, the QP sub-problem at the k^{th} search step shall then be derived.

$$\begin{aligned} &\underset{d\in\Re n}{Min}\ q(d)=\frac{1}{2}d^T H_k d+c^T d \\ &A_i d=b_i\ \ i=1,\cdots m_e \\ &A_i d\le b_i\ \ i=m_e+1,\cdots m \end{aligned} \tag{3-64}$$

The solution procedure of problem (3-63) involves two phases, the calculation of a feasible initial point forms the first phase and the second phase involves the generation of an iterative sequence of feasible points that converge to the solution [178, 179]. With a feasible starting point $X_k = d_0$ from the last search step, the solution directly enters phase II, where the ideology of active-set algorithm is used and a working set $\bar{A}_n$ is maintained as an estimate of the active constraints at the n[th] iteration in solving (3-63). If one or more Lagrange multipliers corresponding to inequality constraints in $\bar{A}_n$ are detected negative, the current point d_n is considered premature and a search direction $\hat{D}_n$ is obtained while updating the working set, inside which the equality constraints are always remained and inequality constraints with negative Lagrange multipliers are deleted. The search direction $\hat{D}_n$ must be able to minimize the objective function of (3-63) while keeping the search on any active constraint boundaries. In order to achieve this goal, the feasible

subspace for $\hat{D}_n$ is formed from a basis Z_n whose columns are orthogonal to $\bar{A}_n$. A typical approach to obtain Z_n is through the QR decomposition of $\bar{A}_n^T$, where Z_n consists of the last *m-l* columns of decomposed matrix *Q*.

$$Z_n = Q\begin{bmatrix} q_{l+1} & \cdots & q_m \end{bmatrix} \tag{3-65}$$

$$Q^T \cdot \bar{A}_n^T = \begin{bmatrix} R \\ 0 \end{bmatrix} \tag{3-66}$$

In the above equations, *l* refers to the number of active constraints and $l<m$. Once Z_n is found, the new search direction is sought via a quadratic minimization in terms of vector p where $\hat{D}_n$ is in the null space of active constraints, namely, a linear combination of the columns of Z_n that is represented as the multiplication of Z_n and minimizer p^*.

$$Min\ h(p) = \frac{1}{2} p^T Z_n^T H_k Z_n p + c^T Z_n p \tag{3-67}$$

Differentiating *h(p)* with respect to variable *p* yields:

$$\nabla h(p) = Z_n^T H_k Z_n p + Z_n^T c \tag{3-68}$$

According to the first order optimality condition, the minimum of (3-66) is reached when $\nabla h(p)$ equals to zero. Therefore, the corresponding p^* is the solution of linear equation (3-68) and the search direction at the n^{th} iterate can be obtained accordingly.

$$Z_n^T H_k Z_n p^* = -Z_n^T c \tag{3-69}$$

$$\hat{D}_n = Z_n \cdot p^* \tag{3-70}$$

A step to the next iterative point is then taken of the form:

$$d_{n+1} = d_n + \alpha \cdot \hat{D}_n \tag{3-71}$$

Where α is the step length along the search direction $\hat{D}_n$. The step length is evaluated using all constraints including the inactive ones.

$$\alpha = \underset{i\in\{1,\cdots m\}}{Min}\left\{\frac{-\left(A_i\cdot d_n - b_i\right)}{A_i\cdot \hat{D}_n}\right\} \qquad (3\text{-}72)$$
$$A_i\cdot \hat{D}_n > 0,\ i=1,\ \cdots\ m$$

Here α is defined as the distance from the current iterative point to the nearest constraint along $\hat{D}_n$. Usually if d_n is not the optimum for (3-63), α would be smaller than unity. In addition, the nearest constraint from d_n is included in the active set. This procedure is repeated until $\bar{A}_n$ has all independent constraints. Next, the Lagrange multipliers are calculated to satisfy the nonsingular set of linear equations.

$$\bar{A}_n^T\cdot\lambda_n = H_k\cdot d_n + c \qquad (3\text{-}73)$$

Inequality constraints in the working set $\bar{A}_n$ corresponding to negative component in λ_n are to be removed and solution procedure summarized via equations from (3-64) to (3-72) are repeated until all the Lagrange multipliers are positive, which means the objective of (3-63) has descended to minimum. The minimizer d^* of (3-63) is then used to calculate X_{k+1},

$$X_{k+1} = X_k + \alpha_k\cdot d^* \qquad (3\text{-}74)$$

Where α_k is the step length parameter, it is determined by an appropriate line search procedure so that a sufficient decrease in a merit function [180, 181].

$$\Psi(x) = f(x) + \sum_{i=1}^{m_e} r_i\cdot g_i(x) + \sum_{i=m_e+1}^{m} r_i\cdot\max\left[0,\ g_i(x)\right] \qquad (3\text{-}75)$$

The penalty parameter r is initialized as $r_i = \dfrac{\left\|\nabla f(x)\right\|}{\left\|\nabla g_i(x)\right\|}$ and iterated using the following formulation to allow positive contribution from constraints that were recently active but are inactive in the solution of the quadratic programing problem (3-63).

$$r_i = \left(r_{k+1}\right)_i = \max\left\{\lambda_i,\ \frac{\left(r_k\right)_i}{2}\right\},\ i=1,\cdots m \qquad (3\text{-}76)$$

Once α_k is confirmed, X_{k+1} is computed using (3-73) and substituted back to (3-62) to update the hessian approximation H_{k+1} for the next search step.

The above phase II procedure will be directly kicked into effect with a feasible starting point X_k.

Otherwise a linear programing is formulated to produce a reasonable initial point for solving (3-63).

$$\begin{aligned} &\underset{\gamma\in\Re,d\in\Re n}{Min}\ \gamma \\ &A_i d = b_i \ \ i=1,\cdots m_e \\ &A_i d-\gamma \le b_i \ \ i=m_e+1,\cdots m \end{aligned} \tag{3-77}$$

Where r is a slack variable settled to be the maximum inequality constraint at this search step. By setting variable d to satisfy the equality constraints, a feasible start point d_0 for (3-63) can be obtained and the search direction $\hat{D}_0$ is initialized as:

$$H_k \hat{D}_0 = -g_k \tag{3-78}$$

In the above equation, g_k is the gradient of objective function at the current search step X_k. Once a feasible starting point is obtained, all actions in phase II can be practiced to find the minimizer for (3-63). The search procedure from (3-60) to (3-75) is repeated until the predefined stopping criteria are met. Fig. 3.3 illustrates the flow chart of using active-set algorithm to solve nonlinear constrained programing, which is applied in the solution procedure of the tertiary and secondary OPF in the HVC.

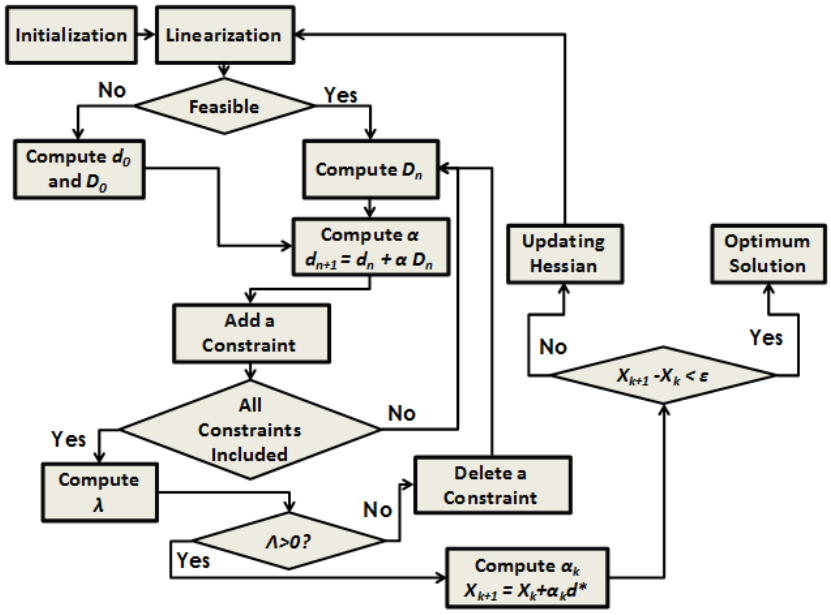

Fig. 3.3 Flow Chart of Active-set algorithm for Solving OPF

All procedures in above flow chat are implemented in Matlab [182]-a software for technical computing. It possesses great capability in managing high-dimensional matrix calculation and can find the optimum

and minimizer for both tertiary and secondary OPF typically within 3 minutes.

3.4 Chapter Summary

This chapter discussed the methodology of the proposed hierarchical voltage control, which covers the physical architecture, the formulation of OPFs and the solution procedure of the nonlinear optimization problem. In order to realize successful system management under supply end uncertainties and dynamic constraints, two major innovative revisions has been made to the traditional hierarchical voltage control.

1) Involvement of wind farm in wide area voltage/VAR regulation by controlling the set-point on reactive output. With conventional plants replaced by wind farms in a massive scale and over 20% of wind penetration, the reactive resources is limited in the system and therefore the proposed control strategy included a wind farm reactive allocation approach based upon secondary regulation and OPF. This approach seeks to adjust the reactive outputs of wind farms and counteract the volatility of wind resources. In case of uncontrollability due to limited reactive capability of wind turbines, coordination between wind farms and conventional plants can be achieved and the proposed control can deliver satisfactory performances under most of operating conditions. Though not yet proved effective for 100% of yearly-round scenarios, the proposed strategy has restored system controllability under supply end uncertainties caused by over 20% of wind penetration, which can serve as enlightenment for control scheme development to manage future power grids with massive renewable integration.

2) Representation of implicit control objective and dynamic constraints using pattern recognition method. This chapter has proposed a PCA-based regression method to establish the explicit mappings between system attributes and security indices. This regression method generalized the information archived from repetitive simulation and defines the linear relationships between the distributions of steady-state voltages to system transient behaviors that are constrained by WECC TPL standards. Hence the tedious transient simulation studies can be greatly simplified and the proposed wide area voltage control involving dynamic constraints can be fast executed and qualified for online deployment. With the dimension of sampling dataset reduced based on principle component analysis where the truncation starts at the most subordinate component, the proposed regression method can produce accurate estimation of target with little computational effort. Its capability in pattern generalization and noise rejection as well as the computational cost will be compared with fuzzy-logic based method in Chapter 5, where the superiority of this PCA-based regression method would be further elaborated.

4. Modeling of Test System

As the full scale WECC planning case is a high-dimensional and complicated model to be used for dynamic studies, a smaller size test system that resembles the real power grid shall be developed to validate the proposed hierarchical control. The 179-bus WECC simplified model discussed in Chapter 2 is hereby chosen to help carrying out the development. It has 29 units supplying roughly 40% of the generation totaled from the 15600-bus WECC planning case. Though highly reduced both in size and capacity, the system preserves reasonable detail in COI transfer area and provides dynamic modeling for units, which meet one of the requirements for building the test system as to support transient-simulation based computation on COI transfer capacity. The one-line diagram of the 179-bus system is presented in Fig. 4.1[183].

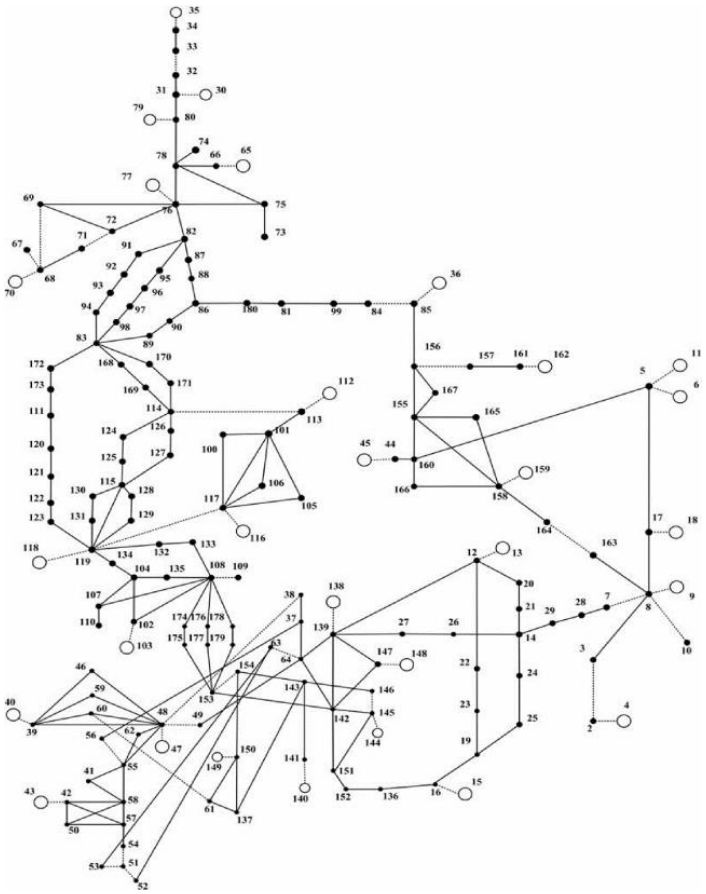

Fig. 4.1 WECC 179-bus System

As shown in Fig. 4.1, this 179-bus model has clearly represented the overall structure of the WECC planning case. However, its transmission network is highly aggregated, where multiple branches sharing the same and adjacent ends are represented as corridors with equivalent impedance and interconnections

with voltage levels lower than 230kV are omitted. This has made it unfit for the N-1 contingency screening, let alone the scenario analysis to estimate the security margin, since severe disturbances causing transient instability may be introduced by tripping a single element in the system and variation in loading levels may aggravate the contingency. Hence, transmission corridors represented as low-impedance branches in this reduced model needs to be split into multiple lines and local VAR support need to be introduced to maintain transient security during disturbance analysis.

In addition, since the proposed control is designed for WECC grid, it shall be validated on a test system that is equivalent to the WECC planning case. Thus, the dynamics parameters of the 179-bus network are to be modified to benchmark the reduced model with the actual WECC grid in frequency-wise disturbance response and COI transfer capacity computed in the CAISO operational limit studies [163].

Furthermore, in order to test the ability of the proposed control scheme to deal with supply end uncertainty with HVDC overlay, wind farms are to be interconnected to the 179-bus network and a HVDC network needs to be designed and constructed. The HVDC with line commutating converters are studied in this dissertation to fulfil this purpose.

With accomplishment of all three types of modifications described above, a 200-bus network with renewable and HVDC as well as equivalence to WECC planning case will be constructed as the test system for the proposed control. The construction procedure will be elaborated in the next three sections of the chapter, which will successively address the customization, equalization and device integration of the WECC-179-bus system.

4.1 Customization

With transmission lines aggregated into corridors and sub-transmission level uninvolved, the WECC 179-bus system is not suitable for N-1 contingency screening. The measures taken to fix this issue include division of transmission corridors and implementation of local VAR support.

4.1.1 Division of Transmission Paths

During the reduction of the detailed planning case, nodes at both end of a transmission path are combined and this path is aggregated into an equivalent branch. The division procedure will break the branch into a number of transmission lines that originally forms the path. As we don't seek to add new buses to the reduced system, those transmission lines will share the same terminals as aggregated nodes and the parameters regarding to impedance and charging will be set the same, which means:

$$R_i^{sp} = n \cdot R^{agret} \tag{4-1}$$

$$X_i^{sp} = n \cdot X^{agret} \tag{4-2}$$

$$B_i^{sp} = \frac{1}{n} \cdot B^{agret} \tag{4-3}$$

Where *R*, *X* and *B* refers to the resistance, reactance and line charging of a branch and *n* denotes the number of transmission lines that the original branch in the reduced system is split into, which is easy to figure out with the graphic information available from maps of western interconnection [184]. There are in total 22 branches in the 179-bus network require division, among which branches located in transfer area (NORTHWEST and PG& E and Central Coast) draw primary attention as how they are modeled would play a significant role in the estimation of security margin. Hence in Table 4.1, a list of aggregated branches in transfer area is displayed and split into multiple transmission lines.

Table 4.1 List of Branches Split in the WECC 179-bus System

From Substation	To Substation	Number of Transmission Lines Split into
GARRISON	JOHN DAY	2
GARRISON	HANFORD	4
HANFORD	NORTH	4
OLINDA	OLINDA1	4
TEVATR	OLINDA4	2
OLINDA1	OLINDA2	2
OLINDA2	OLINDA3	2
OLINDA3	OLINDA4	4

The division of transmission corridors is a customized upgrade applied to the 179-bus model to derive the test-bed for the proposed HVC. It has partially restored the original layout of the high voltage level transmission system of WECC and mitigated the severity of branch loss contingency. However, it may not ensure a secure base case according the TPL standards due to absence of sub-transmission level details except for California coastal area. Since it is tedious and time-consuming to rebuild the sub-transmission network on the 179-bus system, local reactive support can be introduced in forms of fixed shunt and synchronous condensers.

4.1.2 Allocation of Local Reactive Support

As all PQ bus voltages in the test-bed to be developed from the 179-bus system are required to fall between 0.98pu and 1.17pu, fixed shunt are implemented to coordinate with adjustment on PV node voltages for elimination of steady-state violations. The power injected or absorbed from a node via a shunt capacitor is proportional to the square of nodal voltage as:

$$Q = U^2 \cdot B_C \tag{4-4}$$

Where B_c is the admittance of the capacitor and numerically B_c can be negative to simplify the load flow analysis. With Q_N and U_N representing the rated power and voltage of this shunt capacitor and $B_c = \frac{Q_N}{U_N^2}$ the relationship between power injection and nodal voltage can be expressed in the per unit form:

$$Q^* = \frac{Q}{Q_N} = \frac{U^2 \cdot B_C}{Q_N} = \frac{\left(U^* \cdot U_N\right)^2 \cdot Q_N}{Q_N \cdot U_N^2} = U^{*2} \tag{4-5}$$

Differentiating above equation with respect to U^*, we can get the sensitivity of reactive compensation with respect to nodal voltage at $U^* \approx 1$ as:

$$\frac{dQ^*}{dU^*} = 2U^* \tag{4-6}$$

(4-6) indicates that the reactive compensation a shunt capacitor can provide is proportional to the square of nodal voltage, namely if nodal voltage drop 1%, the reactive injection will drop 2%. Hence, when there is a voltage dip due to contingency, the fixed shunt would act less efficiently in providing reactive compensation. Because of this disadvantage, the fixed shunt is considered unsuitable for providing dynamic VAR support and synchronous condensers are thereby introduced.

Synchronous condensers are units that only provide reactive power to the system. Their reactive outputs can be adaptive to system conditions hence playing an important role in mitigation of transient insecurity and weak grids concerns. According to the reactive capability curve shown in Fig. 4.2, synchronous condensers can produce typically 30-35 percent more reactive power compared with generators as the unit can be overexcited in accordance with its capability curve[185]. Thus, to deal with reactive deficiency, placing synchronous condensers instead of generators turns out to be a more efficient approach where adequate reserves can be ensured and units over committing can be avoided [186].

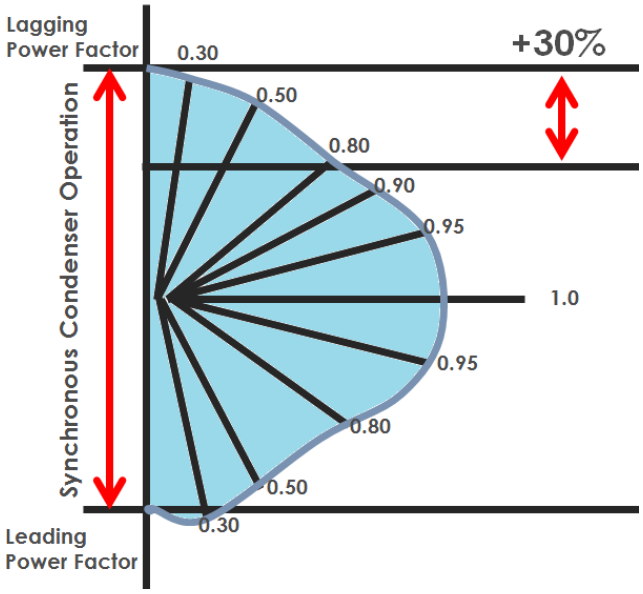

Fig. 4.2 Reactive Capability Curve of Synchronous Condenser

The placement of synchronous condensers is based upon the old layout designed for dynamic VAR support where Flexible AC Transmission System (FACTS) devices were not yet deployed to replace aging units[187]. Since FACTS are neither modeled in the reduced 179-bus grid nor to be dispatched by the proposed HVC, the retired synchronous condenser remains in service and is connected to PG&E network to mitigate transient voltage dip. With similar purpose, another synchronous condenser is added in NORTHWEST area so as to prevent reactive deficiency peak load periods when the northwestern units are stretched to meet the electricity demand from local and distant load centers. In order to make the base case secure under N-1 contingency screening, both synchronous condensers are intuitively given the reactive capability of ±1500MVAR. This capability is fixed for scenario analysis with renewables

The allocation of reactive support has relieved the model from prominent transient instability and made the it suitable for TPL standards constrained contingency screening, based on which the next step of test system construction is carried out to benchmark the reduced model with the actual WECC network in terms of disturbance response and the COI transfer capacity.

4.2 Equalization

In order to make an equivalent test system with similar frequency-based disturbance response and initial COI transfer limit, dynamic parameters of the original 179-bus model are adjusted. The adjustment includes Reduction on generator saturation effect and modification on excitation, out of which the former aims to obtain a no-error initialization and the latter seeks to stabilize the simulated transient responses. Following

the adjustments, the transient simulation and analysis results of the modified system are benchmarked with field recordings and utility reports.

4.2.1 Reduction of Saturation Effect

The saturation effect of a synchronous machine is explained by its open circuit characteristic [188].

$$E_0 = f\left(I_f\right) \tag{4-7}$$

Where E_0 represents the Root Mean Square (RMS) value of the induced open circuit Electromotive Force (EMF) and I_f denotes the excitation current. It is known that with the rotating frequency (f), number of winding turns (N) and the winding distribution ration (K_{w1}) fixed, the RMS value of EMF produced by magnetization is proportional to the magnetic flux (ϕ_0) flowing through the armature.

$$E_0 = 4.44 f \cdot N \cdot k_{w1} \cdot \phi_0 \tag{4-8}$$

Therefore, the open circuit characteristic of a synchronous machine can be graphically expressed as its magnetization curve displayed in Fig. 4.3.

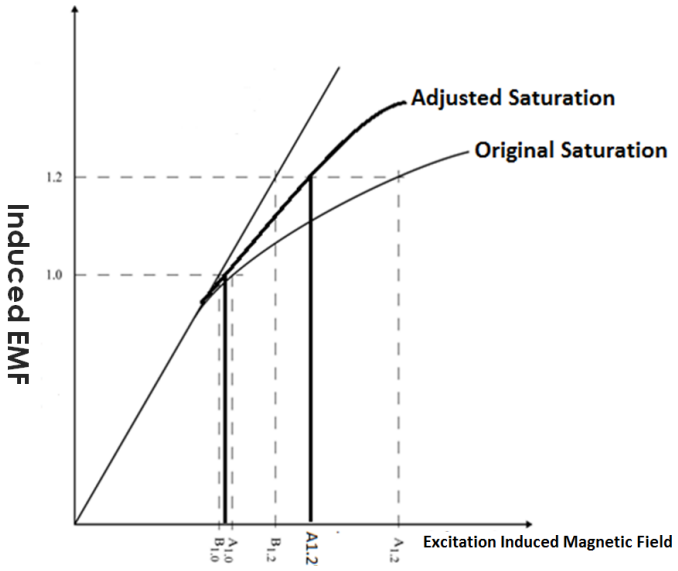

Fig. 4.3 Adjustment of Generator Saturation Factor

As shown, the magnetic circuit of the armature consists of air gap and the iron core. Because of the saturation of the latter, the magnetization curve starts as a straight line and bend towards the x axis when extra Magneto Motive Force (MMF) are demanded to produce the same change in EMF. It is clear from

the figure that the saturation effect would lead to increased excitation to generate unity terminal voltage, which makes the unit susceptible to over-excitation. Thus, the saturation effect needs to be controlled by adjustment on the saturation coefficients in the generator model.

$$S(1.0) = \frac{A_{1.0} - B_{1.0}}{B_{1.0}} \tag{4-9}$$

$$S(1.2) = \frac{A_{1.2} - B_{1.2}}{B_{1.2}} \tag{4-10}$$

By cutting down $A_{1.2}$ and $A_{1.0}$, the magnetization curve can be adjusted as depicted in Fig. 4.3 and the saturation effect can be controlled within a manageable scale so that the field voltage produced by excitation is lower than 5.0 per unit to avoid initialization errors in PSS/E [189]. This a software used in this dissertation to process transient simulations and contingency screening.

Reduction on saturation effect prevented risk of over-exciting and yielded a satisfactory initialization. However, base case simulation showed insufficient damping that leads to oscillatory instability, which requires further tuning on dynamic models.

4.2.2 Modification of Excitation

The excitation system of a unit is responsible for creating the magnetization in its armature to induce open circuit EMF. The excitation system consists of the AVR and the exciter. The elimination of oscillatory instability starts with tweaking AVR gains, and latter accomplished by picking appropriate time constants for exciter and the feedback loop as shown in Fig. 4.4.

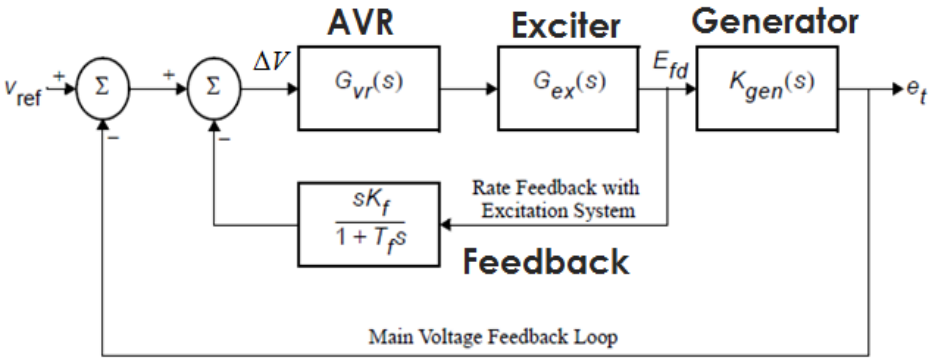

Fig. 4.4 Feedback Excitation System Used in the Reduced Model

It is widely acknowledged that the steady-state gain of the AVR should be high to keep the voltage error

as small as possible in the steady state [189]. However, high-gain fast response AVR can lead to reduced damping of system electromechanical modes of oscillation [190], which accounts for the small signal instability in the reduced WECC system. Therefore the common practice is to design a voltage regulator with high steady-state gain and relatively low gain under transient conditions. The gain reduction is achieved in a number of different ways including shaping AVR transfer function and introducing feedback loop. The AC excitation system displayed in Fig. 4.4 adopted both where the transfer functions for AVR, exciter and open-circuit generator are expressed from (4-11) to (4-13), respectively [191].

$$G_{vr}(s)=\frac{K_A\left(1+sT_C\right)}{\left(1+sT_B\right)} \tag{4-11}$$

$$G_{ex}(s)=\frac{1}{\left(1+sT_A\right)} \tag{4-12}$$

$$K_{gen}(s)=\frac{1}{\left(1+sT_{d0}\right)} \tag{4-13}$$

As for above equations, K_A, T_c and T_B are AVR gain and time constants, T_A and T_{d0} refer to the time constants for exciter and generator. The relationship between the magnitudes of unit terminal voltage (e_t) and the magnetic field voltage (E_{fd}) is expressed in Fig. 4.3. In order to reduce the transient gain, we re-assign values to the parameters in the excitation system by selecting T_c=0 and T_B, T_a much smaller than T_f, the transfer function converting ΔV to E_{fd} can be approximated as:

$$G(s)=\frac{K_A\left(1+T_f s\right)}{1+\left(T_f+K_A\cdot K_f\right)s} \tag{4-14}$$

The default AVR gain was given as 200 to fight against transient instability via shortening of faulted trajectory as high gain AVR can rapidly raise E_{fd} to its maximum and increase the power delivered by the machine [192]. However, since customized changes including splitting transmission path and placement of synchronous condensers are made to the reduced model, the transient instability is less prominent. Thus the AVR gain is cut in half. And with T_c=0, the transient gain of the AVR alone is highly reduced as can be deduced from the logarithmic amplitude characteristic expressed in (4-15).

$$L(\omega)=20\lg\left(K_A\right)-20\lg\left(\sqrt{1-\left(\omega\cdot T_B\right)^2}\right) \tag{4-15}$$

Where ω denotes the frequency in rad/s and T_B=0.01. With values picked for all parameters, the AVR is going to function with exciter and the feedback loop to form an excitation system with high gain in steady state and low gain under transient conditions. Therefore according to the general recommendation [189], the values assigned to K_f and T_f are 0.108 and 1.2 respectively. This will make the excitation system transient gain calculated from (4-14) as 10, one tenth of its steady-state gain. By applying the same procedure to all the excitation system in the reduced model, the oscillatory instability in base case simulation can be eliminated and the frequency response to disturbances can be obtained without noticeable noises. Hence benchmark between this modified reduced model and the WECC planning case is carried out where the set-points on plant terminal voltages and the number of in-service governors are further adjusted to build a control test-bed that is equivalent to the actual WECC power grid.

4.2.3 Benchmark Results

Despite the fact that the test-bed is modified from a reduced model where local support including FACTS devices and Remedy Action Schemes (RAS) is unavailable, it is equipped with governor models for all the units. Since tuning on saturation factor and excitation parameters has already stabilized the transient frequency response of the test system, the governor settings can be modified to mimic system behaviors recorded by Frequency Monitoring Network (FNET) measurements in spite of the difference in generating capacities. Here for simplicity, 11 out of 29 governors accounting for around 30% of the capacity in the test system are switched off to benchmark the simulated frequency response with field recordings as shown in Fig. 4.5.

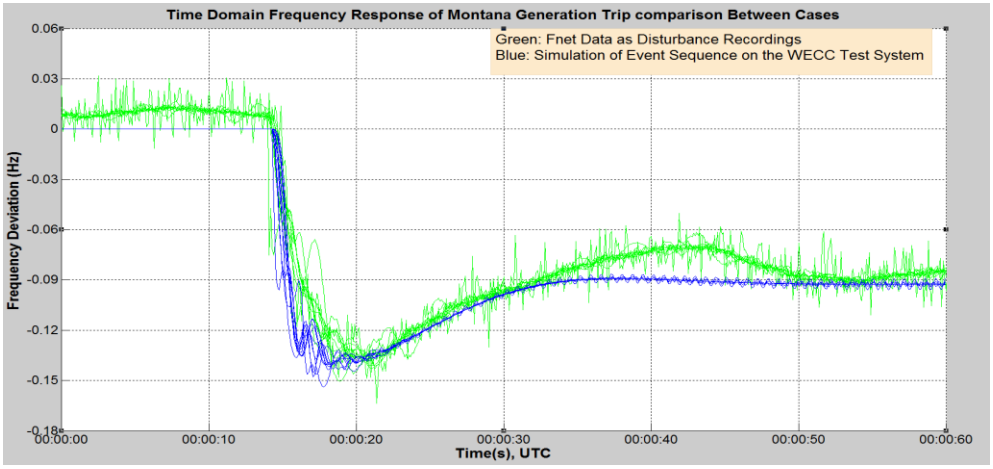

Fig. 4.5 Benchmark Time-domain Frequency Response to Montana Generation Trip

As illustrated, the switching sequences of 1400MW generation trip in Montana are simulated on the test

system and the outcome is compared with FNET recordings. The FNET measurements archived the event-induced frequency responses at multiple locations, corresponding to which, nodes in the test system are selected to represent the simulated behaviors. Despite the pre-event mismatch as the balancing frequency is not always maintained exactly at 60Hz, the overall tendency of the simulated response agrees with the FNET recordings. When the disturbance-induced frequency excursions are on the way to their final settlement, it is observed from Fig. 4.5 that the simulated curve deviates away from the recorded ones for 15 seconds. This is because of absence of Automatic Generation Control (AGC) in the test system. However, as the test bed is not built for secondary frequency regulation, modeling of AGC is not necessary and the discrepancy 20 seconds after the drop of generation is considered acceptable the maximum frequency excursion and final frequency deviation observed from the simulation are close to the measurement recordings. The benchmark of time domain frequency behaviors has validated the equivalency of the test system to the actual WECC power grid in terms of governor settings.

In order to compare the damping ratio and oscillation modes in the simulated and recorded frequency response, a Fast Fourier Transformation (FFT) is carried out to obtain the frequency domain representation of event-induced system behaviors. Since the test system only preserves the high voltage level transmission network from the actual power grid, it may not carry enough details to produce the same local oscillation modes. However, the exhibition of inter-area oscillation caused by different groups of generator swinging against each other is less susceptible to local details and can be benchmarked with measurement recordings. To better assist the understanding of FFT analysis results, a band pass filter is adopted to attenuate local oscillations whose frequency is higher than 0.9Hz and a curve-fitting method is design to de-trend the DC component. Fig. 4.6 displays the spectrum obtained by FFT analysis on frequency response captured on bus ‘HANFORD’.

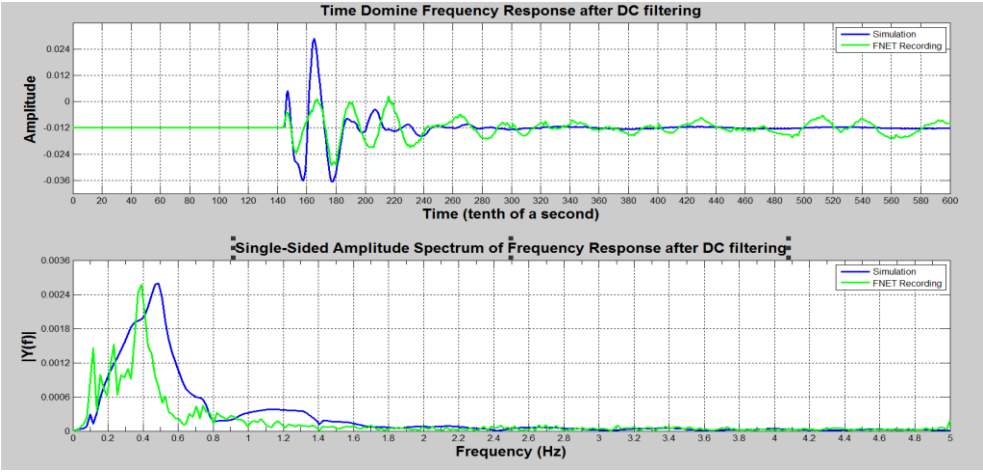

Fig. 4.6 FFT analysis of Oscillation Modes

With the DC component de-trended and local oscillation attenuated, the inter-area oscillatory behaviors pops out in the time and frequency domain representation. It can be observed from Fig. 4.6 that the major oscillation modes of simulated and recorded response are fairly close to each other. The discrepancy in oscillation frequency is within tolerance considering the difference in resolution between the reduced and actual systems. Thereby the test model is regarded as equivalent to the actual WECC grid in terms of synchronous torques.

The damping ratios of the major oscillation modes presented in simulated and measured frequency response are computed in small signal analysis. The overall comparison between the two systems in terms of disturbance induced frequency behaviors is summarized in Table 4.2.

Table 4.2 Comparison of Simulated Frequency Response with FNET Recordings

Item	Maximum Frequency Excursion	Final Frequency Deviation	Inter-area Oscillatory Frequency	Inter-area Oscillatory Damping Ratio
Test System	0.14Hz	-0.09Hz	0.475Hz	0.769%
Actual Grid	0.146Hz	-0.0852Hz	0.4Hz	0.877%

Though not including the sub-dominant oscillation modes, Table 4.2 further demonstrates the close match between simulated and measured responses under the specified event. Therefore the test system is validated as equivalent to actual WECC power grid in terms of disturbance-induced frequency and oscillatory responses.

In addition to frequency, the voltage response of the test system requires to be benchmarked. Thus its COI transfer limit is computed and compared with the results obtained by CAISO using WECC planning case, which is a network model proved statically and dynamically equivalent to the actual power grid [193-196]. The computation is carried out via iterative simulations where generations are increased proportionally to unit capacity in the NORTHWEST and decreased in California to stretch the COI transfer. During the simulations, criteria involved in both WECC TPL standards and CAISO study report are applied to check the transient behavior of the system. Once there is a violation, the simulation ends and the active flow transferred through COI intertie at the current iterate is considered as its limit. The northwestern units are stressed along with the COI intertie during the iterative simulation. Therefore, in order to push the COI limit of the test system as close as what reported by CAISO, the northwestern PV voltages are settled higher to encourage more reactive output under stressed operating conditions. Table 4.3 lists the reported and calculated COI limits along with the system details of the control test-bed and the WECC planning case.

Table 4.3 COI Transfer Limit Comparison between Test System and WECC Planning Case

Case	Bus Number	Total Generation	COI Limit	COI Base	Security Margin
Test System	181	61.4GW	4620.5MW	3130.3MW	1490.2MW
Planning Case	15600	154GW	4800MW	3200MW	1600MW

Despite the difference in size and total generation, the COI limit and security margin of the test system is close to the values obtained via operation limit study on the planning case. Hence the test system after adjustment on PV set-points is considered equivalent to the actual power grid in terms of steady-state layout and dynamic parameters. Transient voltage behaviors presented by the planning case under N-1 contingency screening can hence be replicated by the test system, which can hereby give a close enough estimation of COI limit and security margin of the real WECC grid.

After customization on network structure and allocation of reactive compensation as well as parameter adjustment regarding to unit saturation and excitation, the 181-bus base case of the control test bed is developed from the 179-bus WECC reduced model as shown in Fig. 4.7.

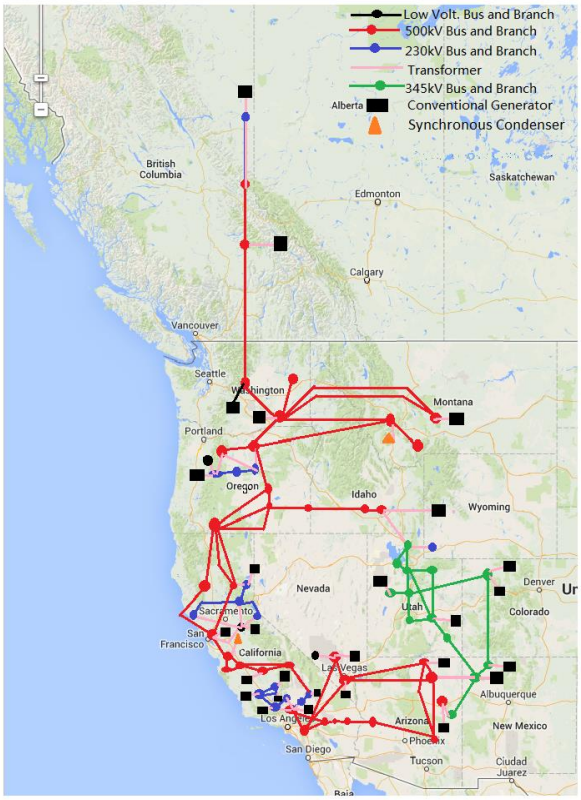

Fig. 4.7 Base case of Control Test-bed Derived from WECC 179-bus System

By benchmark with FNET recordings and CAISO operation limit report, this base case is deemed equivalent to the actual system in terms of disturbance-induced frequency and voltage responses. With standards concerning transient frequency and voltage behaviors involved in the security margin estimation, this equivalence ensured that the observations and the analytical results from the testing procedure of the proposed HVC are useful to the operation and planning of the actual WECC system.

4.3 Device Interconnection

As the proposed HVC is designed to manage system with high level of wind penetration and HVDC overlay, wind farms and HVDC interconnections are modeled and integrated to the base case. With total capacity unchanged, the wind penetration of the base case is improved by replacing the conventional generation with wind outputs. Hence the conventional plants would have fewer units online with lower reactive capabilities. The location of the wind plants is determined based on the loading profile of WECC prototype system [58] that includes information regarding to planned power stations. With more and more wind farms commissioning and system demand increasing, the power grid in the future would have large amount of wind power supplying the growing demand from distant generating locations, which lay extra stress on the existing AC transmission system. Hence the HVDC overlay is built to relieve the stress on AC transmission grid and enable long distance transmission of wind energy to load centers. For the scope of this dissertation, a multi-terminal network made up of CSC HVDC links is deployed to transfer northwestern wind and hydro generations to California load centers [197].

4.3.1 Modeling and Integration of Wind Farm

The wind farms interconnected to the test system are modeled as units aggregated of multiple GE 1.5MW wind turbines, which link to doubly-fed asynchronous generators with partial scale converters as described in Chapter 1. Each wind turbine is equipped with four basic components:

- WT3G: generator converter model that regulates the grid-side converter and decides the power output of this wind units.
- WT3E: Converter control model that feeds in the reactive reference and correct the output of the units through WT3G.
- WT3P: Pitch control model which manages the blade pitch angle according to turbine speed.
- WT3T: Wind turbine model which describes the shaft dynamics and feeds in the shaft speed to WT3P and WT3E for estimation of pitch angle and active power generation.

The interaction and data flow among different control models are displayed in Fig. 4.8.

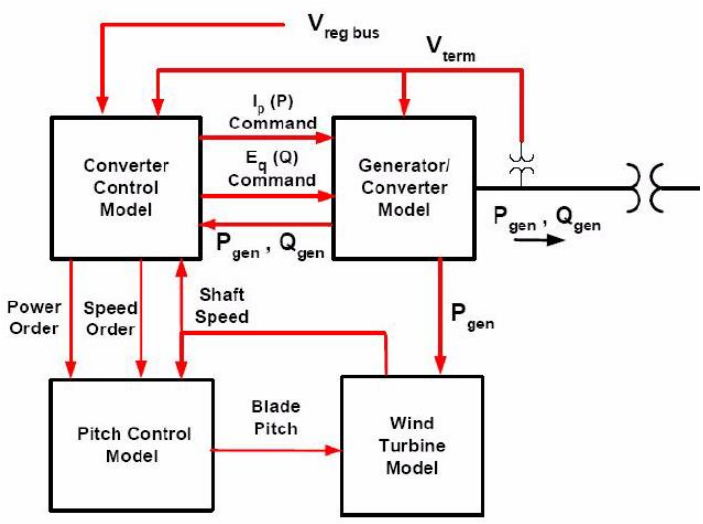

Fig. 4.8 Interaction among Generic Wind Models

With dynamics behaviors regulated by above control models, the wind farm, if its output is beyond a certain limit, is linked to the transmission system with a fixed power factor as suggested by grid regulations [17]. Though intended to be connected in parallel with conventional plants and replace their generations, the POIs of wind farms are electrically decoupled from those of conventional power station to avoid unwanted control interaction. Fig. 4.9 illustrates how a wind farm is interconnected into the test system.

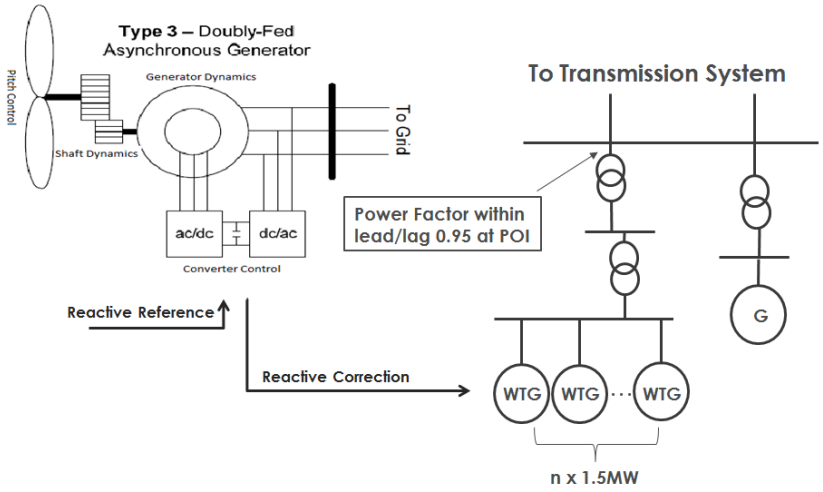

Fig. 4.9 Wind Integration into the Test System

With generating capacity scaled from archived generation profile, 11 wind farms are linked to the transmission grid in parallel with nearby conventional plants. By changing the number of aggregated wind turbines in each farm, base case II and III with 12% and 22% of wind penetration respectively are built for

the control test system. Since Compressed Air Energy Storage (CAES) has been developed to increase wind plant capacity factor [198], the real power output assigned to each wind farm is approximately 50%-70% of its name-plated capacity. Due to the newly added wind plants and transformers, the bus number of case II and III increased to 197. Table 4.4 lists the power stations whose outputs are partially replaced by wind generations to build renewable penetrated scenarios.

Table 4.4 Locations and Capacity of Wind Farms and Conventional Plants Connected in Parallel

Station Name	Case II Wind Farm Generation	Case III Wind Farm Generation	Case II Conventional Plant Output	Case III Conventional Plant Output
CORONADO	300 MW	400 MW	500 MW	400 MW
CANAD	662.04 MW	1062.08 MW	3788 MW	3388.92 MW
GMAIN	400 MW	1000 MW	4080.37 MW	3480 MW
BRIDGER	300 MW	700 MW	1340.22 MW	940 MW
MONTANA	500 MW	1000 MW	2410 MW	1910 MW
DALLES	379.3 MW	878.6 MW	922 MW	422.4 MW
JOHN DAY	1969.71MW	2369.42 MW	3898.079 MW	3449.813 MW
THE NORTH	1000.89 MW	3001.78 MW	8859.110 MW	6858.22 MW
TEVATR2	469.28 MW	1068.56 MW	2997.720 MW	2398 MW
LITEHIPE	550 MW	1050 MW	2645 MW	2145 MW
MOHAVE	780 MW	980 MW	900 MW	700 MW
Total Generation	7.32 GW	13.51 GW	54.08 GW	47.89 GW

With integrated wind capacity scaled from archived data regarding to existing and planned renewable generations, base case II and base case III are good representations of the future WECC grid high level wind penetration. Using them as the control test case would not only validating the fitness and advancement of the proposed HVC in managing high-wind penetrated systems but also provide reference for future deployment of wide area voltage/VAR regulation on the real WECC power grid.

As it is planned to increase the wind penetration ratio of US grid to 20% by 2030 [6], base case III is eventually chosen as the test case for the control validation, yearly-round scenarios will be developed with loading level and wind generation fluctuating in accordance with archived data. With 22% of wind penetration, it meets the future requirement regarding to the scale of renewable integration and hence can

be used to test the capability in managing supply end uncertainty of the proposed HVC. Later on, with the development and adoption of base case IV whose wind penetration is increased to 43%, AC transmission system will be stressed with limited reactive reserve for the HVC to maneuver with. The HVDC overlay structure is therefore built to enable long distance transportation of renewable energy and expand the feasibility region of the proposed control scheme.

4.3.2 Design and Deployment of HVDC Overlay

With DOE planning to increase the wind penetration of US grid to 20% by 2030 and 35% by 2050 [10], more and more wind power stations, which are far from load center, will be integrated to the existing power grid to supply for growing demand. This will result in a fundamental increase in the transmission of large amount of power over long distances. Due to lower cost in infrastructure building and higher efficiency in energy transportation, HVDC links are the primary selection to achieve the visions of future energy capacity expansion. In order to increase the capability of energy transmission, the HVDC links are supposed to be operated under a significantly higher voltage rating. Meanwhile, since interaction with existing AC transmission grid is undesirable, an overlay structure is adopted for building the extra layer of DC transmission system. Hence, a closed-loop HVDC overlay network formed by monopole DC links is built as displayed in Fig. 4.10.

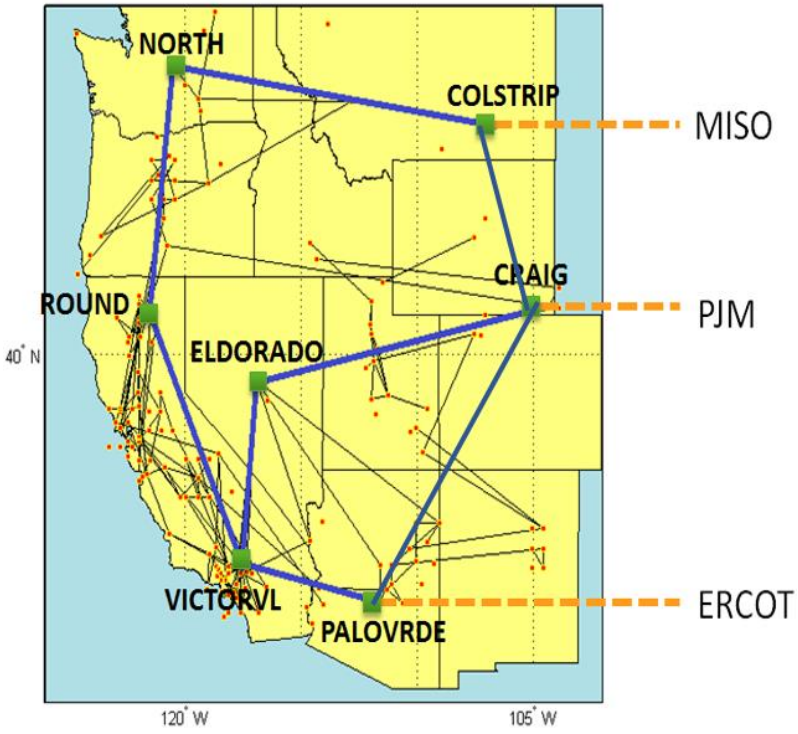

Fig. 4.10 WECC HVDC Overlay Structure

The overlay system designed in Fig. 4.10 seeks to support electricity consumption centers by transmitting southwestern nuclear power, northwestern wind and hydro energy and northeastern fossil generation to Los Angeles. The close loop structure allows the proposed DC overlay to withstand N-1 contingency analysis [197]. To better explain the selection of parameters, a simplified representation of each DC link in the overlay system is illustrated in Fig. 4.11 [199]. V_r and V_i is the AC voltage at the sending terminal and receiving terminal respectively, X_{cr}, and X_{ci} are commutating reactance for sending end rectifier with the firing angle noted as α and receiving end inverter whose extinguish angle is represented by γ. Here we consider all converters use only one bridge for each phase.

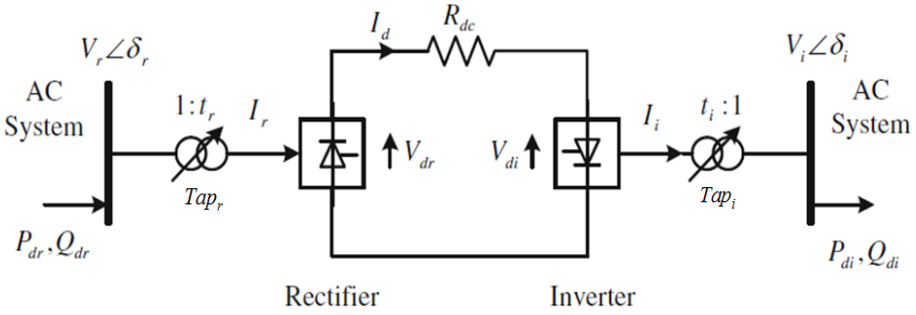

Fig. 4.11 Equivalent Circuit of Each DC link in the Overlay Structure

With the DC voltage noted as V_{dc} already known and transformer winding ratios determined by the quotients of V_{dc} over V_r and V_i over respectively, the tap ratios of transformers at rectifier and inverter end are approximated by:

$$Tap_r \geq \frac{V_{dc}}{V_r \cdot t_r} \tag{4-16}$$

$$Tap_i \leq \frac{V_{dc}}{V_i \cdot t_i} \tag{4-17}$$

With the rated transfer power for this DC link represented as P_{dc}, the direct current that flows through the link can be computed via:

$$I_d = \frac{P_{dc}}{V_{dc}} \tag{4-18}$$

With I_d obtained, the minimum firing angle of sending end rectifier and maximum extinguish angle of receiving end inverter is estimated by the following equations:

$$\frac{3\sqrt{2}}{\pi}V_r t_r Tap_r \cos\alpha^{\min} - \frac{3X_{cr}}{\pi}I_d \geq V_{dc} \tag{4-19}$$

$$\frac{3\sqrt{2}}{\pi}V_i t_i Tap_i \cos\gamma^{\max} - \frac{3X_{ci}}{\pi}I_d \leq V_{dc} \tag{4-20}$$

The range of α and γ can be further determined by selecting α^{max} and γ^{min} to satisfy (4-21)-(4-23).

$$\frac{3\sqrt{2}}{\pi}V_i t_i Tap_i \cos\gamma - \frac{3X_{ci}}{\pi}I_d + R_{dc}I_d = \frac{3\sqrt{2}}{\pi}V_r t_r Tap_r \cos\alpha - \frac{3X_{cr}}{\pi}I_d \tag{4-21}$$

$$\gamma^{\min} \leq \gamma \leq \gamma^{\max} \tag{4-22}$$

$$\alpha^{\min} \leq \alpha \leq \alpha^{\max} \tag{4-23}$$

In this dissertation, the commutating reactance is chosen as 0.57 per unit to allow an appropriate length of commutation period [200]. The other known parameters are listed in Table 4.5 and 4.6.

Table 4.5 WECC Overlay HVDC Data (Part I)

DC Cable No.	1	2	3	4
From Station	COLSTRIP	NORTH	ROUND	ELDORADO
To Station	NORTH	ROUND	VICTORVL	VICTORVL
Length in km	1300	800	900	800
P_{dc} in MW	300	600	100	300
V_{dc} in kV	500	500	500	500
R_{dc} in Ohm	17.16	10.56	11.88	10.56
X_{dc} in mH	397.37	244.54	275.10	244.54

Table 4.6 WECC Overlay HVDC Data (Part II)

DC Cable No.	5	6	7	8
From Station	PALVRDE	CRAIG	COLSTRIP	CRAIG
To Station	VICTORVL	ELDORADO	CRAIG	PALVRDE
Length in km	1000	400	600	900
P_{dc} in MW	600	600	200	100
V_{dc} in kV	500	500	500	500
R_{dc} in Ohm	13.20	5.28	15.00	15.00
X_{dc} in mH	305.57	245.54	200	200

With P_{dc}, V_{dc} and R_{dc} given, the tap ratios and range of ignition angles can be obtained via (4-16)-(4-23). By proportionally increasing the wind generations listed in Table 4.5 base case IV shall be constructed for the test system where the wind penetration is as high as 43%, surpassing the expectation for 2050 scenarios and the operation of the two-layer AC-DC transmission network designed to assist future capacity expansion for WECC grid can be explored.

It is expected that the HVDC overlay does not bring extra risk for the overall system security. Hence, this dissertation will propose a test of the HVC on base case IV and operating scenarios developed from it to examine and enhance the security margin under N-1 contingency screening and realize the coordination between wide area voltage\VAR regulation and multi-terminal HVDC overlay. The testing results would be beneficial for the operation and control of the actual WECC power grid with massive wind integration and DC network in commission.

4.4 Chapter Summary

This section describes the development procedure of the test system where the proposed HVC scheme is to be validated. By customization of system structure and modification of dynamic parameters, the control test-bed is established with equivalence to actual power grid in transient voltage and frequency behaviors and hence capable of producing reference regarding to security margins to system operators of WECC network. By further integrating wind and HVDC overlay to the test system, base cases are created to meet the expectation for future power grid with high percentage of wind penetration and double-layer transmission grid. The proposed HVC are to be tested on those base cases to obtain useful information for future power system operation and control.

This procedure for test system development yields a reduced WECC model that can not only resemble current power system but also represent future grid. Though customized to meet the requirement of the proposed control strategy, this procedure covered major steps involved in standard system-wide model validation [201] including dynamic parameter refining and benchmark with measurement. Therefore procedure can provide reference to other research and academic work where model reduction and equalization are necessary.

5. Deployment of Hierarchical Voltage Control

The proposed hierarchical voltage control is implemented on a 200-bus WECC system for testing and evaluation purposes. With real-time scenarios generated according to the hourly loading profile for WECC prototype model and the archived 5-min interval wind production data from ERCOT[58, 59], repetitive simulations are carried out to construct the database for tertiary OPF formulation, prior to which an interior point OPRF is processed to locate a load-flow convergent solution for each scenario. Later, the classical regression approach is compared with fuzzy-logic based method in the accuracy and computation cost of pattern recognition and curve fitting. Once a more efficient regression method is selected, the tertiary OPF is formulated and the tertiary dispatch is activated. The regional regulation, as the second level of the proposed HVC, need to feed in reference on pilot buses from the tertiary dispatch. The selection of pilot buses is an online procedure based on nonlinear sensitivity analysis, which considers the evolving operating conditions and adjust locations of voltage benchmark point accordingly. The overall procedure for implementation of the proposed HVC is described in Fig. 5.1.

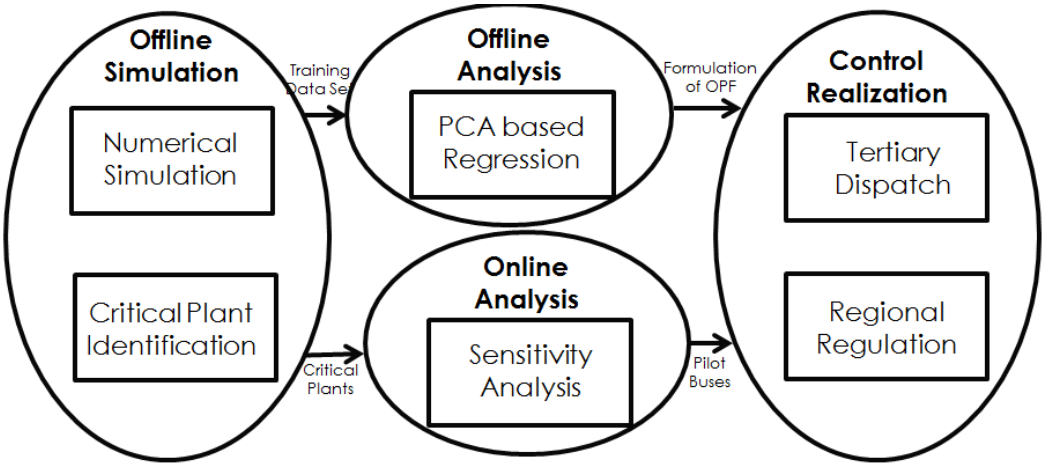

Fig. 5.1 Implementation Procedures of the Proposed Hierarchical Voltage Control

5.1 Enhancement of Solvability

Both the repetitive simulation and the OPF solution requires solvable load-flow initial start, hence systematic mechanisms are taken to match the WECC prototype profiles to the test system which is smaller in size and capacity. Generally, backup devices are introduced to ensure power balance and optimal reactive power dispatch is carried out to obtain a satisfactory load flow result.

5.1.1 Settlement of backup devices

Since plants in the 200-bus equivalent WECC system are highly aggregated and some omitted, the system is not suitable to support yearly round scenarios. Thus, backup units and fixed shunts are added to expand the total capacity of the system and to allow the proposed HVC being evaluated under a wider range of operating conditions. The principal goal for back up unit to kick in is to allow adequate reserve for each generator, both on active and reactive side. Back-up generators are prepared for plants supplying power to load centers, whose potentials are to be stretched during peak-loading period. Table 5.1 describes the location of units with backups and their backup capacity.

Table 5.1 List of Backup Units

Abbreviated Station Name	Balancing Authorities	Control Region	Nearby Load Center	Original Capacity (MVA)	Backup Capacity (MVA)
CASTAIC	LDWP	LDWP	Los Angels	500	1500
HAYNES	LDWP	LDWP	Los Angles	540	1620
INTERMT	NEVP	DC TIE	Salt Lake City	1982	2973
OWENS	LDWP	LDWP	Los Angles	113	339
DALLES	BPA	NORTHWEST	Portland	915.4	750
NORTH	BPA	NORTHWEST	Seattle	10064	8235
ROUNDMT	PG&E	PGE	Sacramento	2000	3000
TEVATR	PG&E	PGE	San Francisco and Sacramento	895	2685
TEVATR2	PG&E	PGE	San Francisco and San Jose	5473	5475
ELDORADO	SCE	SCE	Las Vegas	2104	2106
LITEHIPE	SCE	SCE	Los Angeles	7299	7299
MIROLOMA	SCE	SCE	Los Angeles and San Diego	3000	1500
MOHAVE	SCE	SCE	Las Vegas	1414	1062
PARDEE	SCE	SCE	Los Angeles and Santa Barbara	2500	3750

Each plant listed in Table 5.1 was assigned 3 aggregated back-up units to evenly share the back capacities, which is initially decided according to the planned capacity from loading profiles for WECC prototype system and pertinently scaled to maintain power balance for the widest range of operating conditions. As the for each scenario created for the WECC 200-bus test system, the loading level and wind outputs follows the archived profile of the prototype model and the generation of non-renewable plants are dispatched proportionally to their capacities to meet the demand within the control region. The backup units won't be turned on until the generation required from the plant exceeds its original capacity. In cases when backup generators are needed, the quotient between distribution coefficients noted as N and C is examined to decide how many backup units to be switched into service.

$$N = \frac{P^{disp}}{S^{orig}} - 1 \geq 0 \tag{5-1}$$

$$C = \frac{S^{back}}{S^{orig}} \tag{5-2}$$

$$0 \leq q = \frac{N}{C} \leq 3 \tag{5-3}$$

As for above equations, P^{disd} refers to the required generation from this plant for maintaining power balance. S^{back} is the capacity of each backup unit prepared for the plant. By rounding q up to the next integer, we can get the number of backup units to be switched on, and the output assigned to each unit can be computed via (5-4) and (5-5).

$$P^{reg} = P^{disp} \cdot \left(\frac{1}{1 + \bar{q} \cdot C} \right) \tag{5-4}$$

$$P^{back} = P^{disp} \cdot \frac{1}{\bar{q}} \cdot \left(1 - \frac{1}{1 + \bar{q} \cdot C} \right) \tag{5-5}$$

In (5-4) and (5-5), $\bar{q}$ denotes the round-off number of q. The generation allocation method makes sure that the backup units are only in service when necessary and the outputs distributed among all online units are proportional to their capacities, which saves operational costs and avoided any units get over stressed in production.

In scenarios where the loading level is extremely high, plants listed in Table 5.1 would have all backup units in service, yet still fail to support adjacent nodal voltages. The spare fixed shunts come in handy to solve the problem. The extra reactive injection given to each plant POI is proportional to the reactive capability of its regular units.

$$Q^{inj} = \alpha \cdot Q^{\max} \cdot (1+3C) \tag{5-6}$$

Where Q^{max} is the upper limit of reactive provision of regular units in this plant and α is a scaling factor to adjust Q^{inj} according to loading conditions. The scaling factor associated with certain power stations could be higher to compensate for rapidly exhausted reactive reserves and vice versa. Since all plants in the test system allow operation with leading power factor, their capabilities to absorb reactive power from the system are also compensated by a fixed shunt with negative susceptance.

$$Q^{absb} = \beta \cdot Q^{\min} \cdot (1+3C) \tag{5-7}$$

With the help of backup units and fixed shunt, the yearly-round scenarios for the WECC 200-bus system are created and the real and reactive power can be balanced under all the operating conditions. Next, an ORPF will be carried out to settle the plant POI voltages appropriately so that a convergent load-flow solution can be obtained with all system attributes within predefined limits.

5.1.2 Optimal Reactive Power Dispatch

With yearly-round scenarios generated for the test system, it is noticed that this reduced WECC network is subject to intensive loading for a relatively long period, where the cases are initialized without a feasible solution to the load flow equations. Since both repetitive simulation and the proposed control requires a case to be solvable and today's online state estimation has not been able to 100% resolve this issue. This optimal reactive power dispatch is carried out to enhance the solvability of a scenario under extreme loading conditions. An interior point based method is adopted to solve the optimization.

As for peak loading period, the plant POI voltages are usually settled high to support local voltages; this OPRF is formulated with the objective to maximize reactive reserve, which can firstly avoid plant terminal voltages breaking upper limits and secondly allow more available reactive resource for the proposed HVC to maneuver with. As a nonlinear programing problem, the objective function is penalized by weighting factors denoting the cost of reactive reserves for each plant. Since this is a maximization problem, the cost coefficients are negative [202].

$$Min\ \rho \sum_{i=1}^{N_{gen}} \left(Q_i^{\max} - Q_i^{gen} \right) \tag{5-8}$$

Where N_{gen} is the number of in-service plant and Q_i^{gen} and $Q_i^{\max}$ are the total reactive generation and maximum reactive capability of the i^{th} plant. In order to treat each plant equally, the cost coefficients for

every power stations are set as -100. In addition to the equality constraints as power mismatch equations, hard limits are applied to bound bus voltages. The nonlinear problem can then be formulated with *f(x)* denoting objective function (5-8) and *x* representing power system variable, which includes PV voltages and unit outputs as well as other attributes that depend on them.

$$\begin{aligned} &L(x,\lambda) = f(x) + \lambda^T h(x) \\ &h(x) = 0 \\ &x^{\min} \le x \le x^{\max} \end{aligned} \tag{5-9}$$

The hard limits are rigorously enforced by augmenting the Lagrange function in (5-9) with objective-like equations in terms of *x*, x^{min} and x^{max}. The equations are called barrier functions denoted as *B(x)*, which can be written as:

$$B(x) = -\left(10^{\mu}\right) \sum_{i=1}^{N} \left[\log\left(x_i - x_i^{\min} \right) + \log\left(x_i^{\max} - x_i \right) \right] \tag{5-10}$$

As for (5-10), *N* is the number of variables and μ is the barrier coefficient initialized as 1.0 to adjust the magnitude of *B(x)* as iteration proceeds. The barrier function is continues and asymptotic to the limits as depicted in Fig. 5.2. With no definition for values of *x* outside the specified range, the barriers are formed in which all of x is corralled within a feasible region. The optimization problem would be infeasible if any equality constraint requires *x* to violate this feasible region.

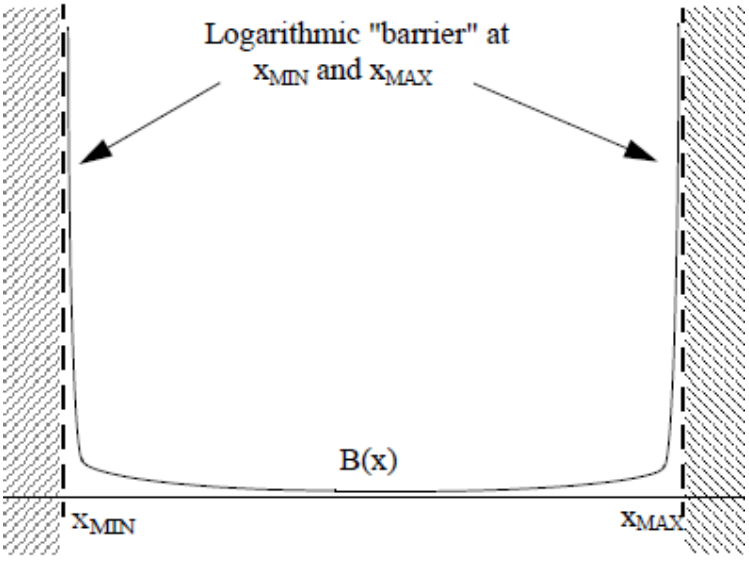

Fig. 5.2 Logarithmic Barrier Function

The barrier function speeded up the solution process by transforming inequality constraints into objective terms and eliminated an additional iterative process that would otherwise be required to prevent violations. The addition of the barrier function converts the constrained problem into a more easily handled unconstrained problem that can be formulated as *L(x,λ)'*.

$$L(x,\lambda)' = f(x) + \lambda^T h(x) + B(x) \tag{5-11}$$

The minimizer of (5-11) always occurs within the limits imposed by x_{MIN} and x_{MAX}. Since combined Lagrange function (5-11) is unconstrained, its minimizer is sought by employing the Newton's second order solution method, where the step changes are formulated by the standard Kuhn-Tucker conditions.

$$\begin{bmatrix} \frac{\partial L^2(x,\lambda)'}{\partial x^2} & \frac{\partial L^2(x,\lambda)'}{\partial x \partial \lambda} \\ \frac{\partial L^2(x,\lambda)'}{\partial \lambda \partial x} & \frac{\partial L^2(x,\lambda)'}{\partial \lambda^2} \end{bmatrix} \cdot \begin{bmatrix} \Delta x \\ \Delta \lambda \end{bmatrix} = \begin{bmatrix} -\frac{\partial L(x,\lambda)'}{\partial x} \\ -\frac{\partial L(x,\lambda)'}{\partial \lambda} \end{bmatrix} \tag{5-12}$$

The solution of (5-12) provides corrections to both x and λ and solves a quadratic approximation to the nonlinear system. The right hand side of (5-12) is composed of a lambda gradient term $-\frac{\partial L(x,\lambda)'}{\partial \lambda}$ that encompasses the equality constraint residuals. This term encourages the value of x to move in a direction that reduces the power mismatch as each node. Simultaneously, x is urged to move in a direction that minimize the combined Lagrange function by another gradient term $-\frac{\partial L(x,\lambda)'}{\partial x}$ in the right hand side of (5-12). Variable x and λ are hence updated iteratively using the solutions from (5-12).

$$x_{k+1} = x_k + \alpha \cdot \Delta x \tag{5-13}$$

$$x_{k+1} = x_k + \alpha \cdot \Delta x \tag{5-14}$$

where the step length α can be 1.0 if the correction can be added to x without violating any limits, otherwise, α will be decided by how much the most limiting element reduces the correction and would be smaller than 1.0. The barrier term contributes to (5-12) and its impact is diminished as the solution progresses. The exponent coefficient μ is used to reduce the magnitude of the barrier function at every iteration which results in a favorable step length larger than 0.5. This reduction continues until the final value of the barrier coefficient is reached, which is set as 0.0001 in solving the optimal reactive power dispatch. The direct IP ORPF problem is solved in PSS/E with all phase shifter and transformer tap ratios

fixed to simplify the control actions. Even with an infeasible start, the optimal allocation of reactive generation from both non-renewable and wind power stations can be obtained almost instantaneously. And the load flow convergence and acceptable voltage map settled without extra time cost. Inspired by previous publications on solvability enhancement using interior point methods [140, 203], this direct IP ORPF accomplishes its designed purpose without modification on loading conditions. Therefore, it can serve as a fast and convenient remedy for online state estimation.

Together with settlement of backup devices, the ORPF described above has made all scenarios created for the test system solvable with all attributes falling into desired bounds. Hence, the case preparation is completed and repetitive simulations can be launched for pattern recognition of transient system behaviors and formulation of tertiary OPF.

5.2 Selection of Regression Method

Formulation of the tertiary OPF is a crucial to the performance of the proposed HVC. As to support online control actions, the objective and constraints of the tertiary OPF shall be represented straightforward in terms of static system attributes so that the execution of control can be swift. Meanwhile, the solution of the OPF must converge to an operating point that maximizes the security margin without any violation on system limits. Therefore, lower-order mappings between system variables and security indices are preferred for formulating the OPF problem so that the Hessian approximation of (3-60) can be simplified. Additionally, the regression method used to obtain the mappings need to have excellent generalization capabilities and superior noise rejection. As for the latter, the Artificial Neural Network (ANN), though do not provide explicit mapping, exhibits more promising performance in managing high-dimensional dataset compared with the classical regression methods. Hence, This section evaluates its candidacy to replace the PCA-based Regression (PCR) method described in Chapter 3.Since the proposed PCR yields linear projection between variables and targets. The ANN applies linear transfer functions in each neuron model as shown in Fig. 5.3.

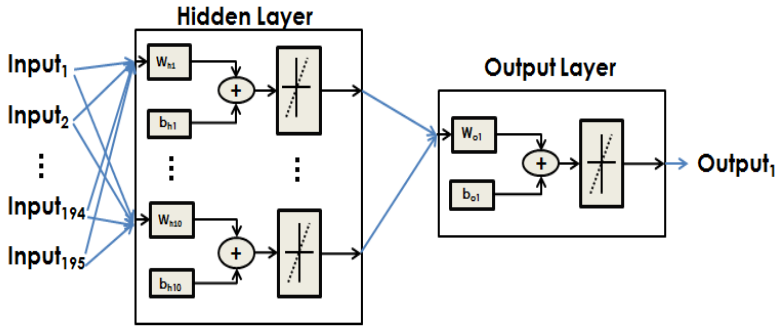

Fig. 5.3 Neuron Network Designed for Formulating Tertiary OPF

As shown, the ANN designed to deal with data from repetitive simulation has three layers. The number of neurons in the hidden layer greatly impacts the network training time. With more hidden neurons, it would request fewer epochs to complete training but ask for more time to finish each iterate. In the contrary, fewer hidden neurons can reduce the time spent for each iterate but lead to more epochs for the network to converge. After an evaluation of computation cost, 10 neurons were placed for the hidden layer for the most efficient performance. This ANN is applied to implicitly formulate the objective function of the tertiary OPF, where the system steady-state voltages are projected to COI transfer limit. The data needed for training are recorded from transient simulation using April scenarios, where the wind outputs fluctuates frequently and noise are common for pattern recognition. The capability of noise rejection would be highly demanded in this situation. The training performance of the designed ANN IS shown in Fig. 5.4.

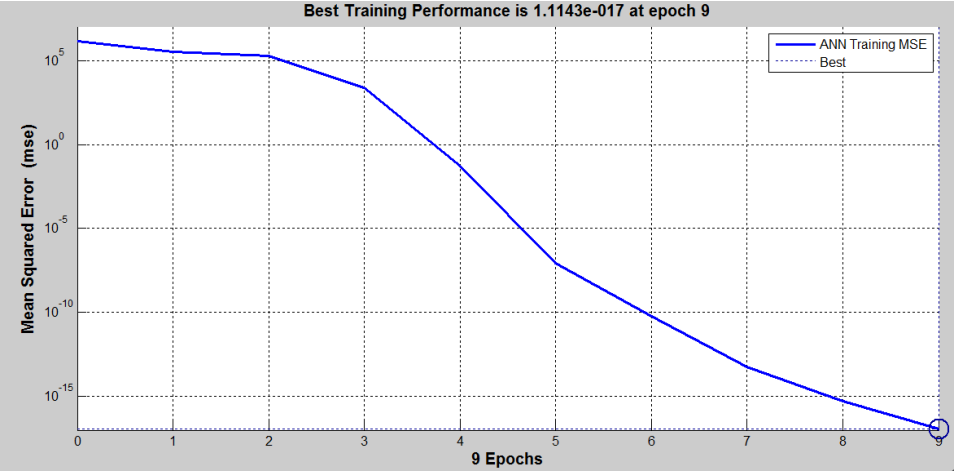

Fig. 5.4 Training Performance of the designed ANN on Simulated data from April Scenarios

As can be seen from the above figure, it takes 9 epochs for the network to converge. The training procedure lasted for 7 seconds, which is acceptable since the OPF formulation is an offline procedure. The Mean Square Error (MSE) utilized to evaluate training performance in Fig. 5.4 is calculated as:

$$MSE = \frac{\sum_{i=1}^{m} \left\| F_{out} - F_{arch} \right\|^2}{m} \tag{5-15}$$

Where F_{out} is the estimate of transfer limit and F_{arch} are information recorded from repetitive simulations. The regression performance in Fig. 5.5 illustrates that the relationship between system variables and transfer limit can be generalized despite of noises and the target value can be reached with the trained neuron network.

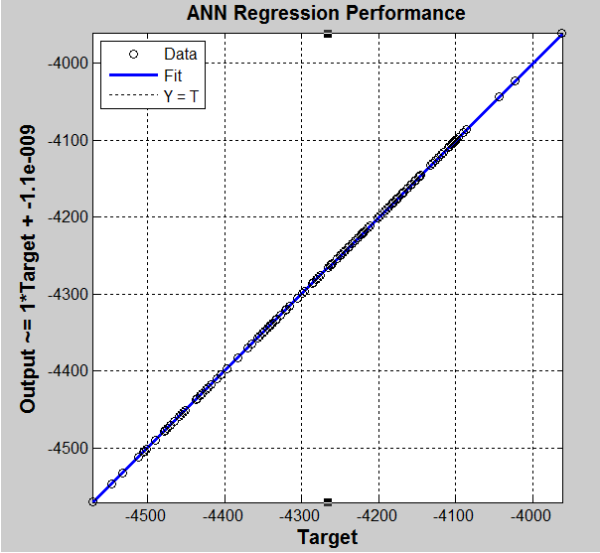

Fig. 5.5 Regression Performance of the Designed ANN on Simulated Data from April Scenarios

Here the archived data from simulation results are randomly divided into half for training and regression respectively. The *X* and *Y* axis value in Fig. 5.5 are negative of estimate and simulated transfer limits and the estimations are fairly close to the simulated information hence the ANN is trained well for expressing the projection between system variables and the COI transfer capacity.

Since the test system is a reduced WECC network, we noticed that every bus, as long as electrically decoupled from its neighbor, is making a bigger impact on system behaviors compared with the planning case. Thus for the PCA-based regression, we need to preserve the as many components as allowed to reach for accuracy in pattern generalization. Fig. 5.6 shows the contribution made by each component.

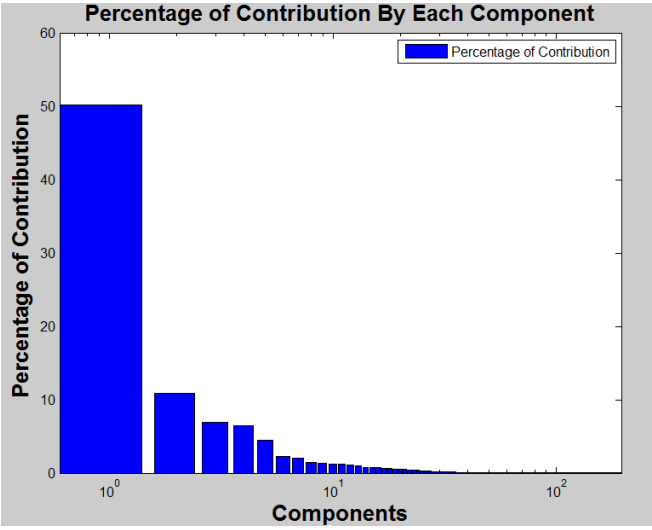

Fig. 5.6 Percentage of Contribution by Each Component

As shown, the percentage of contribution is close to zero for components whose significances are ranked after 100. With the purpose to keep the most critical information, the data truncation starts with the most insignificant components. However, to make sure even less important information is also included for the regression, 155 out of 195 components has been picked to carry out the PCR, which linearly fit the system variable to meet the target value in a form of 3.24. The regression performance of the PCR with 155 components preserved is depicted in Fig. 5.7.

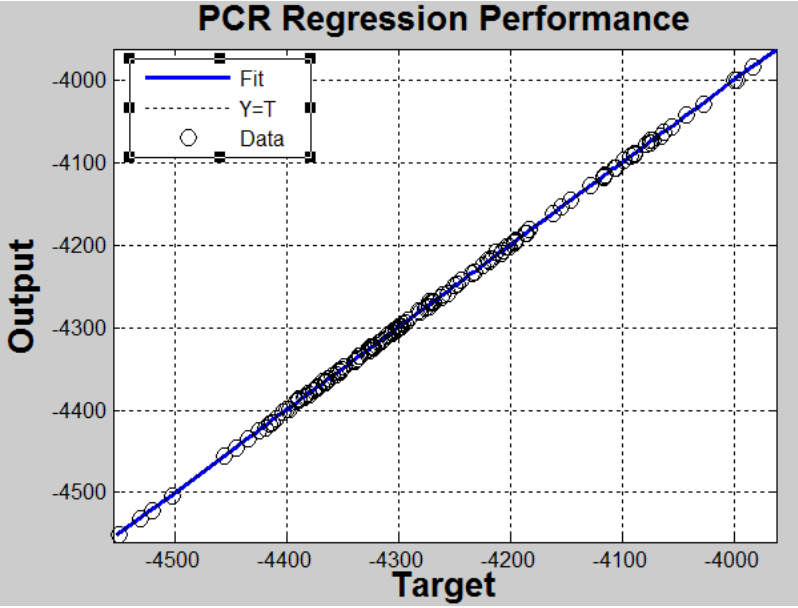

Fig. 5.7 Regression Performance of PCR on Simulated Data from April Scenarios

Similar to Fig. 5.5, the *X* and *Y* axis in above graph denotes the output and target value as the negative of COI transfer limit. As all the circles referring to estimated values visually fall on the blue curve, the PCA-based regression method is delivering satisfactory performance formulating the objective function of the proposed HVC. Without obvious differences in regression performance, an analytical comparison on residuals resulted from the two regression methods is carried out, where the definition of mean error rate is introduced.

$$Mean\% = \frac{\sum_{i=1}^{m} \left\| F_{out} - F_{arch} \right\|}{\sum_{i=1}^{m} \left\| F_{arch} \right\|} \tag{5-16}$$

To fulfil the comparison, repetitive simulations are carried out on January, April and August scenarios, which are chosen due to presence of high wind penetration, intensive fluctuation of wind outputs and long

period of stressed system conditions respectively. Then the accuracy of PCA-based regression and feed forward ANN is compared by means of MSE and mean error rate resulted from training and testing procedure, which is displayed by Fig. 5.8. The impact of number of component preserved for regression is also studied in this comparison.

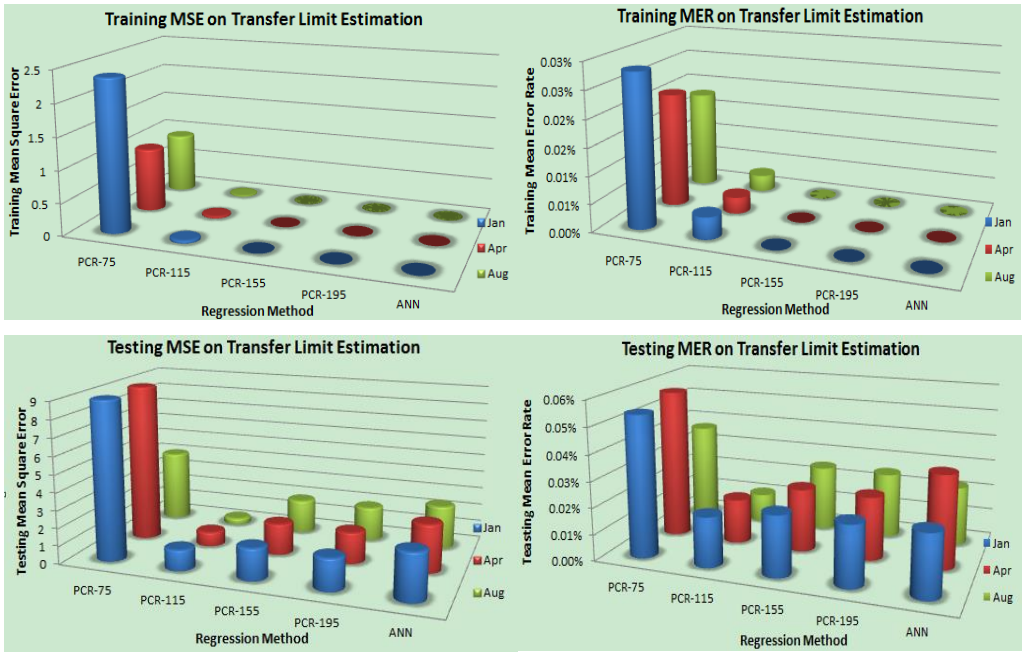

Fig. 5.8 Comparison of Regression Accuracy among different Methods

As can be noted in Fig. 5.8, the overall training error by PCR is negligible if adequate components are involved. The testing error proves be minimum with 115 components preserved as more component participating in regression may lead to over fitting. However, in order to fully understand the pattern of archived data, 155 principal components are eventually retained on account of higher training preciseness. The proposed PCR with more than 155 components preserved gives lower values in both MSE and MER compared with ANN while computation costs are much less. Moreover, as PCR yields explicit expressions for objective and constraint of the tertiary OPF, user defined derivative can be used to speed up the solution procedure. Hereby, the candidacy of ANN to formulate the tertiary OPF based on fuzzy-logic theory is removed and the PCR with 155 component is deemed accurate enough to accomplish the offline regression procedure for the proposed HVC.

Fig. 5.9 illustrates the estimation on transfer limits for approximate 900 cases. It can be seen from the figure that the estimation agrees with the results obtained from transient simulations. As can be noticed from the zoomed in details at the lower right corner, the estimating error for each case is within 1MW and therefore considered negligible.

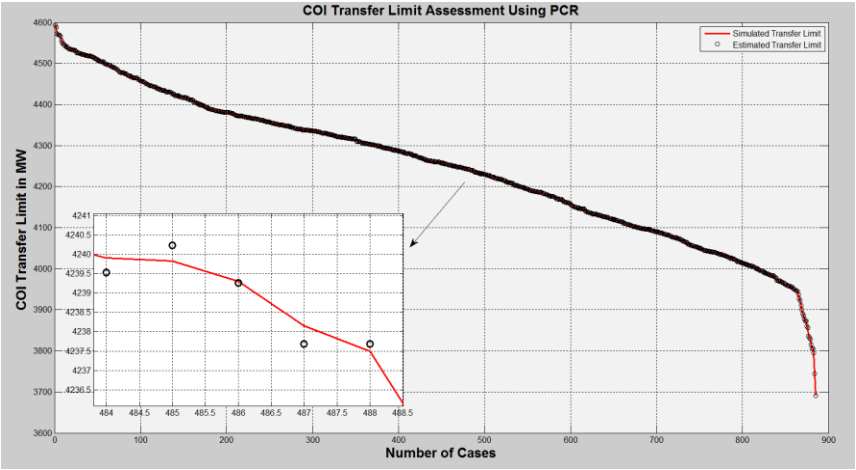

Fig. 5.9 PCR-based Estimation of Transfer Limit

This section compared the PCR with ANN to find the most suitable regression method and meanwhile decided the proper number of components to be preserved. The resulting regression approach achieves the highest accuracy in estimating the COI transfer limit, namely formulating the objective function of the tertiary OPF. With the same mapping methodology, this PCR approach is selected for formulating constraint functions (3-1) to (3-8) as well. Due to its capability to be fast executed and provide explicit formulations, it expedited the tertiary control actions including the OPF and the reference feedback loop, which is a great asset for the proposed HVC to benefit from.

5.3 Pilot bus selection

The secondary regulator in the proposed hierarchical voltage control drives the actual POI voltage to its desired set-point calculated from secondary OPF at a 10-minute interval, and meanwhile, adjusts this set-point every minute to meet the reactive demand. Compared with most coordinated and adaptive control summarized in Chapter 2, where the execution of SVC happens every 10 seconds, the proposed HVC achieves its designed purpose with a much slower control loop and less frequent primary level adjustments. Additionally, the all control actions in the proposed HVC are supposed to conclude with the dynamics completely damped out within the designated cycle. This means the secondary regulation can start under strictly steady-state conditions, which is beneficial for pilot bus selection in the proposed control as the computational costly quasi-steady-state sensitivity analysis is no longer necessary.

Moreover, with the overall goal to maximize security margin, the proposed HVC seeks to reinforce system weak parts. The pilot bus selection needs to serve this purpose hence this dissertation presents a new mechanism where nodes that can reflect the changes in security margins the most are identified as pilot buses. AC steady state sensitivity analysis is used here to prevent approximation errors for stressed

scenarios. As this mechanism does not produce an even distribution of pilot buses to ensure maximum observability, the locations of pilot nodes are susceptible to system condition changes. Therefore this selection mechanism is integrated as an online procedure to account for evolving operating conditions.

In order to enforce the proposed voltage control to the whole system, each control area must be placed with at least one pilot node. The test system as originated from the WSCC system created by EPRI[160, 204] has 12 control areas, out of which 9 areas are selected due to their stronger coupling with PV buses. Some regions that are far from transfer areas are represented by equivalent networks. Those regions include Canada, Rocky MT, Southwest and Northwest. Regions located along California coast, where PV bus voltages exerts higher influence on COI Transfer Limit, contains details in sub-transmission level and are represented by balancing authorities. Due to the deregulation in US power grid, it is uncommon for balancing authorities to share access with the control center to regulate units within their territories. Hence the division of control region is fixed for the proposed HVC. The control areas of the test system are illustrated in Fig. 5.10., in which each control region is highlighted with dark circle and red labels.

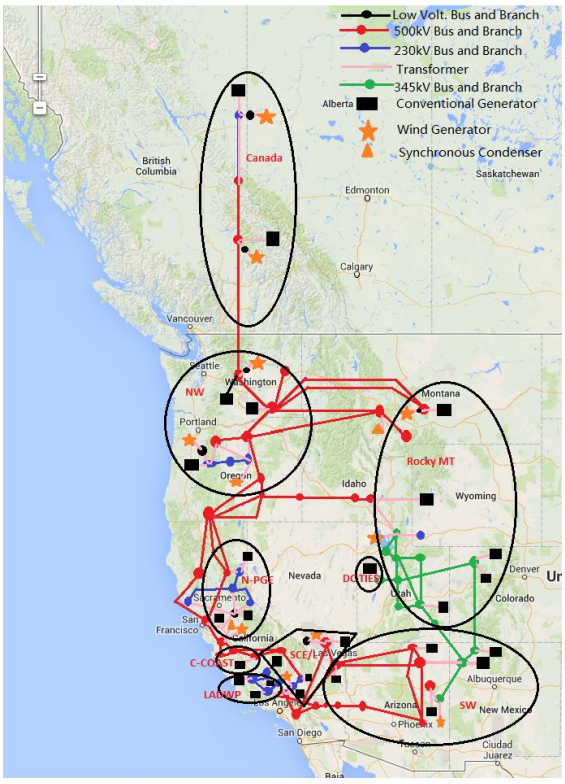

Fig. 5.10 Control Areas of the Test System as the Simplified WECC Model

Generally speaking, to best serve the control objective, variation on pilot bus voltages shall be a good measure of transfer limit changes. This is realized in two phases: identification of critical plants and location

of most sensitive PQ buses. For Phase I, repetitive simulations are carried out on the base case of the test system to find out the impact of PV voltage variations on COI transfer capacity. The simulated results are summarized in Table 5.2-5.9, where we vary the voltage set-point for one plant and maintain PV bus voltages for other power stations. The range for set-point variation is bounded by pre-defined limits on system attributes and depends on the reactive output capability of each plant. Here the sensitivity of the MW change of COI transfer limit with respect to plant POI voltage is calculated, and only plants with non-zero sensitivities are listed.

Table 5.2 Summary on Impact of SOUTHWEST Plant POI Voltage Variations on COI Transfer Limit

Abbreviated Name	HAYDEN	**PALOVRDE**	CORONADO
Fuel Type	Coal	**Nuclear**	Wind
Volt. Range	[1.0,1.06]	**[1.0,1.08]**	[1.0,1.1]
Transfer Limit Increase	5.5 MW	**26 MW**	1.2 MW
Sensitivity MW/0.01pu	0.92	**3.25**	0.12

Table 5.3 Summary on Impact of SCE Plant POI Voltage Variations on COI Transfer Limit

Abbreviated Name	ELDORADO	LITEHIPE	**MIROLOMA**	MOHAVE	PARDEE	**MOHAVE**
Fuel Type	Solar	Natural Gas	**Natural Gas**	Coal	Coal	**Wind**
Volt. Range	[1.0,1,1]	[1.0,1,1]	**[1.0,1.08]**	[1.0,1.08]	[1,1.06]	**[1.0,1,1]**
Transfer Limit Increase	143.33 MW	-18.95 MW	**117.171 MW**	15.22 MW	45.59 MW	**35.67 MW**
Sensitivity MW/0.01pu	14.33	-1.895	**14.65**	1.906	7.6	**3.567**

Table 5.4 Summary on Impact of LDWP Plant POI Voltage Variations on COI Transfer Limit

Abbreviated Name	HAYNES	OWENS	**CASTAI**
Fuel Type	Gas & Steam	Hydro	**Pump-Hydro**
Volt. Range	[1.0,1,1]	[1.0,1.1]	**[1.0,1.1]**
Transfer Limit Increase	19.43 MW	3.26 MW	**23.62 MW**
Sensitivity MW/0.01pu	0.1943	0.0326	**2.362**

Table 5.5 Summary on Impact of PG&E Plant POI Voltage Variations on COI Transfer Limit

Abbreviated Name	ROUND MOUNTAIN	TEVATR	**TEVATR2**	**TEVATR2**
Fuel Type	Hydro	Hydro	**Hydro**	**Wind**
Volt. Range	[1.06,1.08]	[1.0,1.08]	**[1.0, 1.04]**	**[1.0,1.06]**
Transfer Limit Increase	9.143 MW	111.615 MW	**565.857 MW**	**24.268 MW**
Sensitivity MW/0.01pu	4.572	13.952	**141.46**	**4.04**

Table 5.6 Summary on Impact of NORTHWEST Plant POI Voltage Variations on COI Transfer Limit

Abbreviated Name	DALLES	J_DAY	**THE NORTH**	DALLES	J_DAY	**THE NORTH**
Fuel Type	Hydro	Hydro	**Hydro**	WIND	WIND	**Wind**
Volt. Range	[1.02,1.1]	[1.02,1.08]	**[1.04, 1.06]**	[1.0,1.04]	[1.0,1.02]	**[1.06,1.0613]**
Transfer Limit Increase	590.5 MW	1909.8 MW	**1173.3 MW**	2.765 MW	0.012 MW	**2.4 MW**
Sensitivity MW/0.01pu	73.812MW	318.3	**586.65**	0.691	0.006	**18.46**

Table 5.7 Summary on Impact of CANADA Plant POI Voltage Variations on COI Transfer Limit

Abbreviated Name	**CANAD**	CMAIN CM	CANAD
Fuel Type	**Natural GAS**	COAL	Wind
Volt. Range	**[1.0,1.06]**	[1.0,1.06]	[1.0, 1.1]
Transfer Limit Increase	**3.32 MW**	0.002 MW	0.159 MW
Sensitivity MW/0.01pu	**0.55**	0.0003	0.0159

Table 5.8 Summary on Impact of ROCKY MT Plant POI Voltage Variations on COI Transfer Limit

Abbreviated Name	CRAIG	**EMERY**	NAUGHT	BRIDGER	MONTANA
Fuel Type	Coal	**Coal & Gas**	Coal & Gas	Wind	Wind
Volt. Range	[1.0,1.06]	**[1.0,1.06]**	[1.0, 1.08]	[1.0,1.1]	[1.0,1.1]
Transfer Limit Increase	12 MW	**55.68 MW**	1.523 MW	2.631 MW	0.468 MW
Sensitivity MW/0.01pu	2	**9.28**	0.19	0.263	0.0468

Table 5.9 Summary on Impact of Plant POI Voltage Variations on COI Transfer Limit-Other Control Areas

Abbreviated Name	**INTER MOUNTAIN**	**DIABLO**
Fuel Type	**Coal**	**Nuclear**
Control Region	**DC TIE**	**CNT COAST**
Volt. Range	**[1.0,1.06]**	**[1.02,1.08]**
Transfer Limit Increase	**4.17 MW**	**6.082 MW**
Sensitivity MW/0.01pu	**0.695**	**1.014**

Plants whose POI voltage variations are most influential to COI transfer capacities are identified as critical plants as highlighted with boldface in Table 5.2-5.9. In order to involve all control areas in the wide area voltage/VAR regulation, at least one plant within each area is deemed critical. Hence, for control region 'Central Coast' and 'DC Tie', station 'DIABLO' and 'Inter Mountain' are considered critical though their sensitivity to transfer limit increase is lower compared with plants in other regions. Additionally, in order to encourage wind farm participation in the proposed HVC, wind plants with sensitivity value larger than 1 are regarded as critical so that the pilot bus selection based on which would allow better supervision and management on wind farm behaviors.

With 12 critical plants in total identified for 9 control areas, the pilot bus selection enters Phase II where online AC steady-state sensitivity analysis is carried out to locate the most sensitive PQ buses where the sensitivity analysis is derived from the power injection equation [205].

$$S = \Delta(V) Y^* V^* \tag{5-17}$$

Where $\Delta(V)$ refers to the diagonal matrix whose diagonal elements are the bus voltages and V^* and Y^* denotes the conjugate of voltage vector and admittance matrix respectively. (5-17) can be partitioned into the following.

$$S = P + jQ = \begin{bmatrix} S_l \\ S_g \end{bmatrix} = \Delta\left(\begin{bmatrix} V_l \\ V_g \end{bmatrix}\right)\begin{bmatrix} Y_{ll}^* & Y_{lg}^* \\ Y_{gl}^* & Y_{gg}^* \end{bmatrix}\begin{bmatrix} V_l^* \\ V_g^* \end{bmatrix} \tag{5-18}$$

As for 5.18, subscripts *l* and *g* represent quantities that are associated with the PQ and PV buses, respectively. Hence for PQ buses, the power injection equation can be re-written as:

$$S_l = \Delta(V_l) Y_{ll}^* V_l^* + \Delta(V_l) Y_{lg}^* V_g^* \tag{5-19}$$

With the admittance matrix only related to network model and being constant, the Taylor series expansion of 5.19 with respect to PQ and PV voltage magnitudes is:

$$dS_l = \frac{\partial S_l}{\partial |V_l|} d|V_l| + \frac{\partial S_l}{\partial |V_g|} d|V_g| \tag{5-20}$$

As the test system is not modeled with voltage-dependable loads, it is desirable that the complex power at a PQ bus to be insensitive to the voltage magnitude variations, i.e. dS_l=0. Hereby from (5-20), the sensitivity matrix of the PQ bus voltage to the variations in the PV bus voltage can be derived.

$$\frac{d|V_l|}{d|V_g|} = -\left[\frac{\partial S_l}{\partial |V_l|}\right]^{-1} \frac{\partial S_l}{\partial |V_g|} \tag{5-21}$$

$\frac{\partial S_l}{\partial |V_l|}$ and $\frac{\partial S_l}{\partial |V_g|}$ can be obtained by differentiating 5.19 with respect to PQ and PV voltage magnitudes respectively.

$$\frac{\partial S_l}{\partial |V_l|} = \Delta\left(e^{j\delta_l}\right)\Delta\left(Y_{ll}^* V_l^* + Y_{lg}^* V_g^*\right) + \Delta\left(V_l^*\right) Y_{ll}^* \Delta\left(e^{-j\delta_l}\right) \tag{5-22}$$

$$\frac{\partial S_l}{\partial |V_g|} = \Delta(V_l) Y_{lg}^* \Delta\left(e^{-j\delta g}\right) \tag{5-23}$$

With δ denoting the phase angle and $|V_g|$ as the magnitude of critical plant POI voltages, buses with maximum absolute values on $\frac{d|V_l|}{d|V_g|}$ are searched within each control region and recognized as index to look for pilot buses. Those selected pilot nodes can best reflect voltage variations on critical plants and hence provide a good measure of transfer limit changes. Moreover, as AC power equations are utilized in the sensitivity analysis of pilot bus identification, its accuracy can be guaranteed for yearly-round scenarios as no approximation error due to linearization will be introduced for stressed operating conditions.

The pilot bus selection described above is an intuitive method invented during the dissertation work to best coordinate with the proposed HVC. It serves the control goal by allowing close watch on critical plant

behaviors and further prevents the COI transfer capacity of an off-nominal scenario deviating from the tertiary OPF optimum. Although this pilot bus selection has sacrificed part of observability in non-critical power stations, it does not lay detrimental effect on the control performance since the behaviors of non-critical plants impact little on the security margin of the system. Therefore, satisfactory security reinforcements on off-nominal scenarios are delivered by the proposed pilot bus selection mechanism with affordable cost on observability.

5.4 Chapter Summary

This section focused on the implementation of the proposed hierarchical voltage control on the test system constructed in Chapter 4. In order to achieve the best testing results, the dissertation has proposed two innovations:

1) **The direct interior-point optimal reactive power dispatch to locate load flow solution for otherwise unsolvable cases**. With the appropriate arrangement of backup devices and introduction of barrier function, this ORPF can bring solvability back to a case with all system attributes falls within the pre-defined limits as long as power balance can be maintained. Moreover, as the objective function is designed to maximize the reactive reserves, this OPRF has allowed extra resources for the proposed HVC to maneuver in enhancing system security margin.

2) **The intuitive pilot bus selection to allow satisfactory security reinforcement on off-nominal scenarios**. Serving as good measures of transfer limit deviation, the pilot bus voltages in off-nominal scenarios are to be driven to the minimizer point of the tertiary optimization problem, which pushes the security margin indexed by transfer capacity to the optimum of the tertiary OPF. Moreover, the pilot buses selected by this mechanism allows better observability on critical plants, who contribute the most in bringing up COI transfer capacity in the proposed control. Hence, it encourages more regulation effort to be laid on those critical plants and improve the efficiency of the proposed HVC.

6. Results and Analysis

6.1 Basecase Results

With the proposed HVC successfully launched in the test system, the tertiary OPF formulated via regression of simulation recordings can be carried out for nominal snapshots and the secondary OPF to set PV bus voltages can be processed on off-nominal snapshots. However, prior to scenario analysis, the performance of the HVC is first evaluated with base cases I-III where different percentages of wind penetrations are presented. Since all base cases share the same loading level, the impact of wind penetration on system security margin and control performance is also investigated. This gives us an intuitive understanding of how wind penetration impacts the security margin and the proposed control. The outcomes of control applying to base case I-III are listed in Table 6.1

Table 6.1 HVC Performances on Base Cases

Case	Bus Number	Wind Generation	Wind %	Initial Transfer Limit	Controlled Transfer Limit	Security Margin Increase
I	181	0GW	0%	4620.5MW	4778.5MW	158MW
II	197	7.37GW	12.08%	4593.5MW	4722.4MW	128.9MW
III	197	13.51GW	22.0%	4445.8MW	4533.7MW	87.9MW

Since all base cases are considered as nominal snapshots, only tertiary OPF is applied decide appropriate pilot bus reference based upon which the plant POI voltages are re-dispatched. For all three cases, scenarios of various operating conditions are derived and randomly selected for creating sampling dataset, based on which the tertiary OPF is formulated. By checking table 6.1, it is obvious that increase in wind penetration has greatly contributed to the shrinkage of the initial security margin by reducing the existing COI transfer limit. This is because of decreasing in system reactive reserve due to more and more conventional generators replaced by wind turbines with limited reactive capability. In wind-penetrated cases, the displacement of conventional generations is especially prominent in NORTHWEST, where high-capacity wind farms participate in energy supplying as demonstrated in Chapter 4. This leads to extra loss of available reactive resources in NORTHWEST, which is the sending area that provides power to California through COI intertie. Thus, when the northwestern conventional units are stretched towards their limits, the reactive reserve in this area is drained first of all, which aggravates the transient voltage dip under critical

contingencies and further reduces the security margin of the system.

Though the initial transfer limits of wind penetrated cases are conservative compared with case I, there are still space for the proposed control to take actions. By re-dispatching the POI set-points for all in-service plants, the pre-event voltage distribution is optimized with units supporting weak parts of the system regulated with a higher reactive output and more reactive reserve. This procedure is completed by region-wide adjustment of conventional unit stator voltage and modification on wind turbine reactive reference, which unit AVRs and turbine converter control would always try to maintain, forcing the reactive support to system weak points at the desired level during disturbances and allowing higher reactive output from units under stressed conditions. To ensure satisfactory performance, there must be enough reactive reserve in the system for the proposed HVC to maneuver with. This is often not the case for high-wind penetrated power grids, which explains the reduction in security margin increase induced by HVC in Table 6.1 as wind penetration goes up in the system.

In all, by applying proposed HVC scheme in base cases, we discovered that increasing percentage of wind penetration reduces the initial margin of the system. While the proposed scheme can serve to partially restore this margin, its performance is negatively affected by wind integration, as insufficient reactive reserve has made the wide area regulation hard to process without breaking steady-state limits. It is noticed that the HVC enables less than 100MW in margin increase in base case III, where 22% of wind penetration is presented. However, since the base cases are derived on top of a reduced WECC model which holds equivalence to the WECC planning case. They do not represent evolving system conditions nor resemble snapshots captured from real-time operation. Hence, other than giving an intuitive understanding of how wind penetration affects security margin and the proposed control, the control results from base case applications won't suggest the performances of the HVC under real-time conditions. Hence, yearly-round scenarios on basis of case III are derived, where the distribution of system load varies and the wind penetration is not always as high as 22%. With scenario analysis involved, the impact of wind penetration and system loading levels on the proposed HVC can be systematically evaluated and the online capability desired for the proposed control to function under a variety of operating conditions can be examined.

6.2 Scenario Analysis

6.2.1 Single Scenario

The scenario analysis starts with deployment of the HVC on a random snapshot captured in January, which is a month with frequent occurrence of high levels of wind penetration. The details of this snapshot is shown in Table 6.2

Table 6.2 Details of January Snapshot

Captured at	Wind Generation	Total Load	Wind Penetration	Initial Margin
Jan-29 7:00am	13.429 GW	61.2 GW	21.55%	897.9 MW

By formulating the OPF with sampling dataset obtained by simulations on archived January cases, it increased the accuracy in margin estimation and hence boosted the performance of the proposed HVC as 174.8MW increase in security margin is enabled by the control. The security enhancement can be better illustrated by comparison of simulated transient voltage behaviors before and after control as shown in Fig. 6.1 and 6.2. \

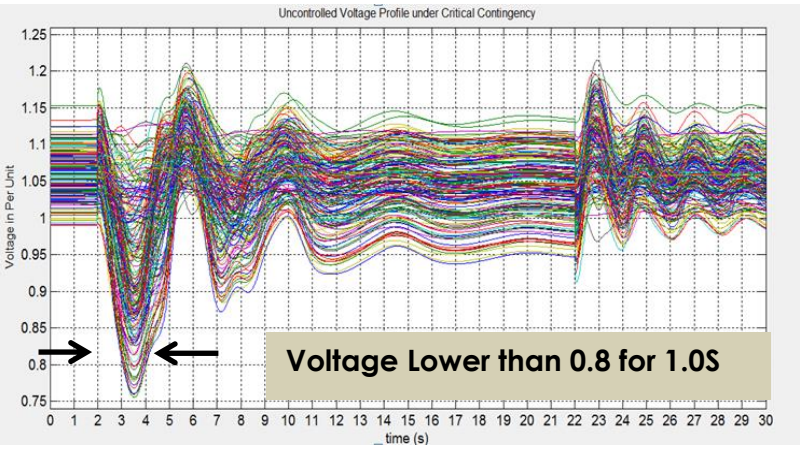

Fig. 6.1 Transient Voltage Behavior in January Snapshot Before HVC Control

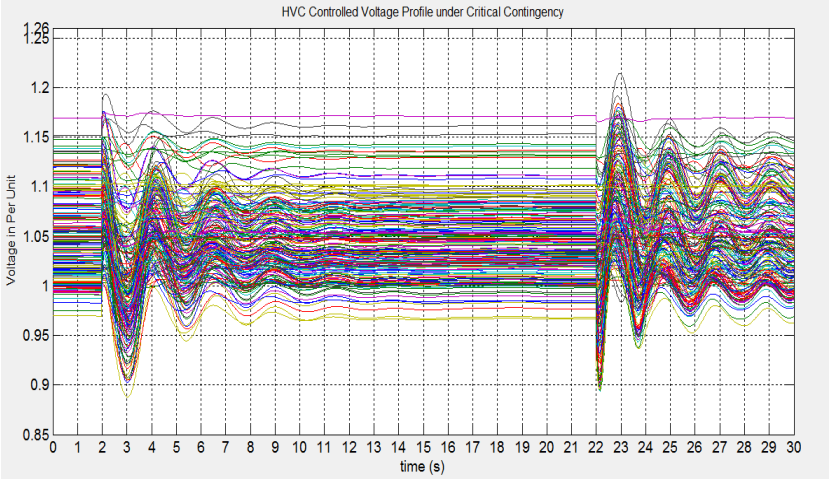

Fig. 6.2 Transient Voltage Behavior in January Snapshot After HVC Control

The critical contingency mentioned in Fig. 6.1 and 6.2 for this typical snapshot is the monopole DC loss of PDCI, which is modeled as halving of load in NORTHWEST and injection in California. With the one of the two PDCI link out of service at 2s, 1500MW of power transfer from the north to the south is shifted to parallel AC lines, adding stress to corresponding transmission paths including COI. As the results, the transfer area is subject to reactive deficiency. This deficiency contributes to lower voltage settlement in transfer area during the event and is aggravated by the exploration of COI transfer limit when northwestern units are powered up and Californian ones are recessed to further bring up the amount of power transmitted through COI intertie. Until one point, as shown in Fig. 6.1, the first swings of simulated voltage curves dip lower than 0.8 for more than 20 cycles, which constitutes a violation of WECC TPL standards and brings risk to the system. The most severe dip is observed at Bus 'MALIN', one of sending terminals of the COI intertie. The event of monopole DC loss lasts for 20 seconds and as indicated in above figures, at the end of 22s, this DC link is restored back to service and the voltages in transfer area shall return to their original settings after the device switching dynamics are damped out.

To mitigate the transient voltage dip and improve the rate of voltage recovery, the proposed control seeks to increase POI voltage settlement of plants electrically within or close to the transfer area. This has contributed to a different pre-event voltage distribution as depicted in Fig. 6.2 where extra reactive provision squeezed out form those plants can support transfer area nodal voltages during the DC loss and have the system live through the event without violation of security standards. A visualization of this snapshot on a Matlab-based WECC model shows the event-induced low voltage region is suppressed to invisible by the proposed control as elaborated in Fig. 6.3, where the left and right graph showing uncontrolled and controlled scenario respectively.

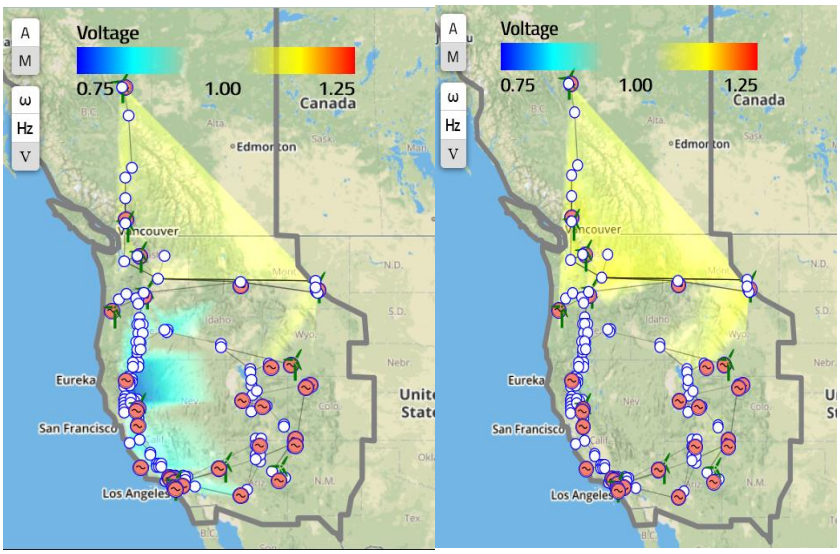

Fig. 6.3 Visualization of Proposed HVC on January Snapshot

The DC loss event majorly affects voltage in transfer area and does not have much influence in the far north. Therefore, the expanded yellow region in Fig. 6.3 indicates that northwestern and Montana units are considered electrically close to the transfer area and are assigned with a higher pre-event terminal voltage by the proposed control. Here the units located in northern California are not considered for terminal voltage adjustment as they are close to the receiving end of COI intertie and intended to cover the demand of local load centers.

6.2.2 Daily Scenario Analysis

With satisfactory outcome from single scenario application, this proposed HVC is put to operation for continuously 24 hours where its ability to handle variations of operating conditions is examined. 66 scenarios consecutively captured in January, the month with long period of high wind penetrations, are streamed in for the control to act on.

As off-nominal snapshots are involved here, secondary regulation loop is put into function to maintain the pilot bus voltage as close as to hourly computed references. Here by assuming that the secondary regulator successfully addresses the minor variations in the system and correct the plant POI voltages accordingly, the enhanced margin for every off-nominal snapshot are calculated with all the plant terminal voltages settled to the references computed from secondary OPF. The control performance is illustrated in Fig. 6.5 with the evolving system condition explained in Fig. 6.4.

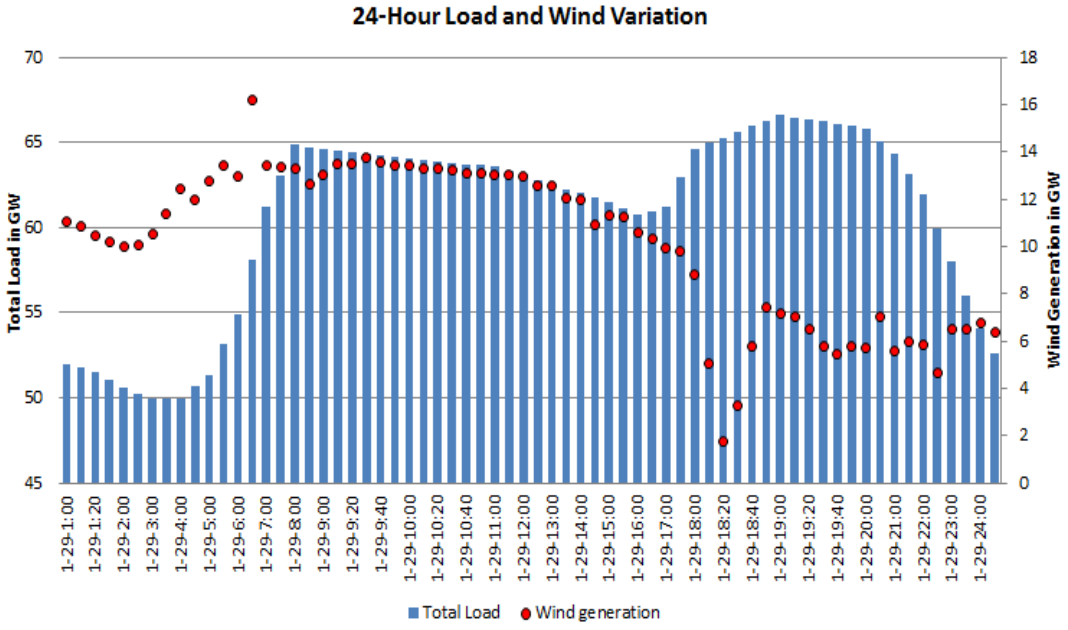

Fig. 6.4 Variation on Wind Generation and Loading Levels within 24 Hour

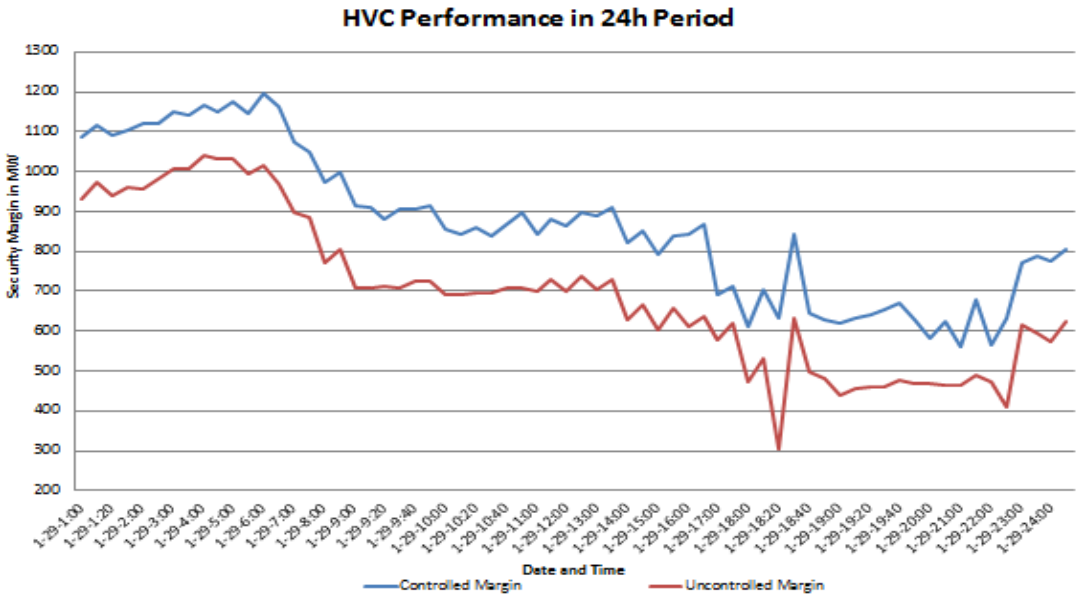

Fig. 6.5 Performance of the proposed HVC in 24 Hour Period

Fig. 6.4 and 6.5 suggest that no matter the variation in wind generation and loading level, the proposed HVC can always produce around 200MW of increase in system margin, which is a promising result that testified the capability in uncertainty management of the proposed control.

By further analysis of the reactive reserve in the 24-hour scenarios, it becomes noticeable that the source reserve is proportionally related to the security margin of voltage constrained cases, which is in concert with the intuitive interpretation of control performance on base cases. Here the source area corresponds to the sending area notified as yellow region in Fig. 6.3, The PV voltages in this region are regulated with higher set-points to force adequate reactive injections to system weak points during disturbances. The reactive reserve here is computed as the sum of difference between maximum output capability and the pre-event generation of all source area plants.

After excluding several snapshots whose margins are limited by angle instability, Fig. 6.6 illustrates the relationship between source reactive reserve and system security margin. It can be seen from Fig. 6.6 that the controlled margin is also proportionally related to the initial source reserve. This is because the reactive regulation is more of a regional action where inter-area transfer of reactive power is uncommon. Thus, it is unlikely that the available resources in other non-stressed region can be dispatched over long distance to support the weak parts of the grid, which explains the necessity of the source area to have enough reserve for the proposed control to function properly.

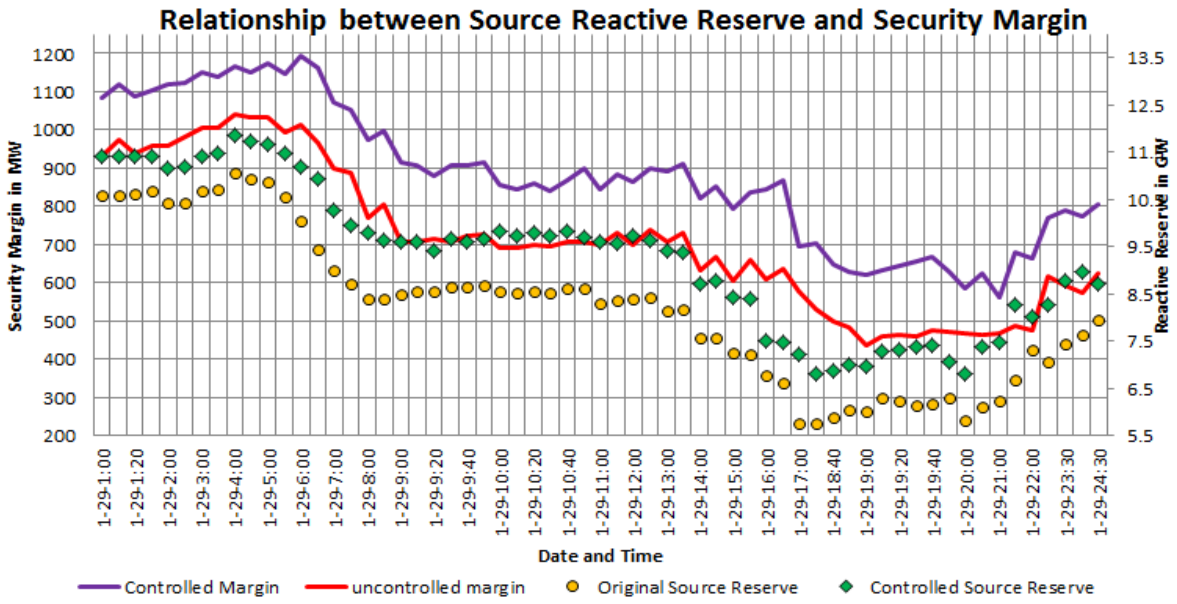

Fig. 6.6 Relationship between Source Reactive Reserve and Margin of Voltage Constrained Cases

As demonstrated earlier in this chapter, the reactive reserve in the system is closely related to system loading level and wind generation, which offers a more convenient way to explain how the operating conditions affect the function of the proposed control scheme. It is therefore important to study the HVC performance on yearly-round scenarios so that a general understanding of control robustness and feasibility region can be obtained.

6.2.3 Yearly Scenario Analysis

With one nominal snapshot captured for every hour and five off-nominal ones derived between the hour, there are in total 8784 scenarios developed for tertiary regulation and 43290 cases generated for secondary control. Those scenarios cover a wide range of operating conditions where the system total load grows from 43.7GW to 85GW and the wind outputs varies between 0.4GW to 14GW. Due to the deficiency in source area reserve, the control fails to function for cases with loading level higher than 76GW even with the help of back up devices. In addition, 24 scenarios with total load lower than 45.5 GW respond little to the control actions due to the overabundance of local reactive power, which push voltage to a high value that leaves little space for the proposed control to act. All uncontrollable snapshots turn out as rare segments in August and April and constitute less than 2.5% of all the yearly-round scenarios. Hence they do not impair the long-term effectiveness of the proposed HVC. For all controllable snapshots, to better illustrate the performance of the proposed HVC under different system conditions, a number of selected control results in terms of margin enhancement is displayed in Fig. 6.7.

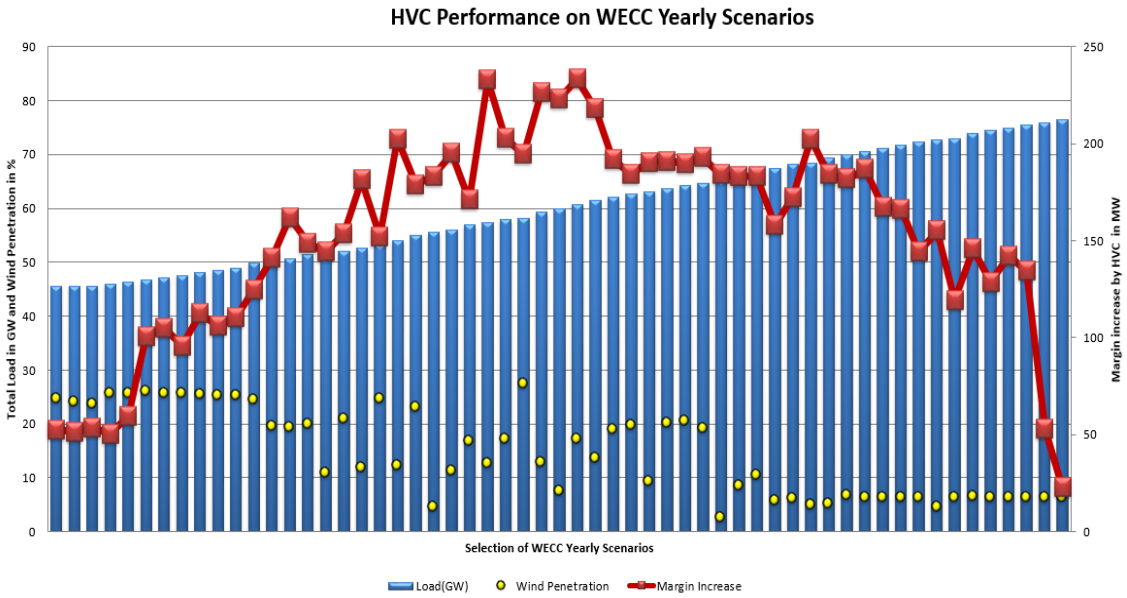

Fig. 6.7 HVC Performance on Selected Yearly-Round Scenarios

It is obvious in Fig. 6.7 that the proposed control achieves its maximum effect when the total load in the system is around 60GW-a medium value among all manageable loading levels. It is also noticed that the raise of loading level and increasing in wind penetration present to be detrimental to the HVC performance by suppressing the margin increase enabled by the control. Hence we deduce that there is are boundaries in terms of wind penetration and loading level outside which the proposed control cease to function without extra support. In order to approximately locate the boundaries, the HVC is performed in cases with limiting loading levels under different levels of wind penetration as depicted in Fig. 6.8.

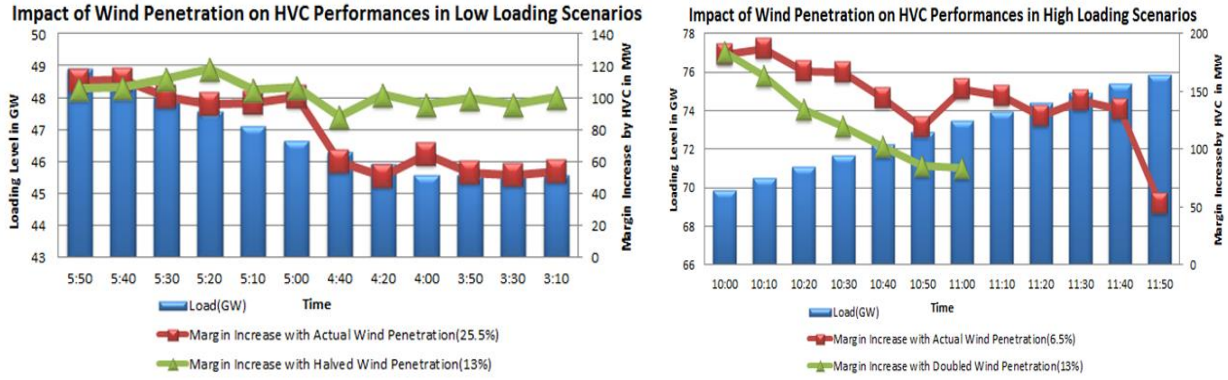

Fig. 6.8 Impact of Wind Penetration on HVC Performance with Low Loading Level

The left and right graph of Fig. 6.8 list a series of consecutive scenarios captured in April and August respectively. Those scenarios represent either lightly loaded or extremely stressed operating conditions. To

investigate the maximum reachability of the proposed control, control performance are evaluated with wind penetration are halved for April cases and doubled for August snapshots as illustrated by the green curves in above graphs. A comparison between the left and right graph of Fig. 8 further demonstrates the weakened control performances regarding to security margin improvement under extreme loading conditions. The influence of wind penetration grows larger as loading level inches closer to upper and lower boundaries of the control's reachability. As demonstrated by the green curve, 13% of wind penetration limits the upper loading bound of the HVC's feasibility region to 73GW but relax the lower loading bound to 44GW. With follow-on calculations, it is discovered that over 20% of wind penetration will result in further deduction in the maximum controllable loading level of the proposed HVC to lower than 67GW, which is almost 20GW lower than the maximum loading appeared in yearly round scenarios. The feasibility region of the proposed HVC in terms of wind penetration and loading condition is intuitively approximated in Fig. 6.9.

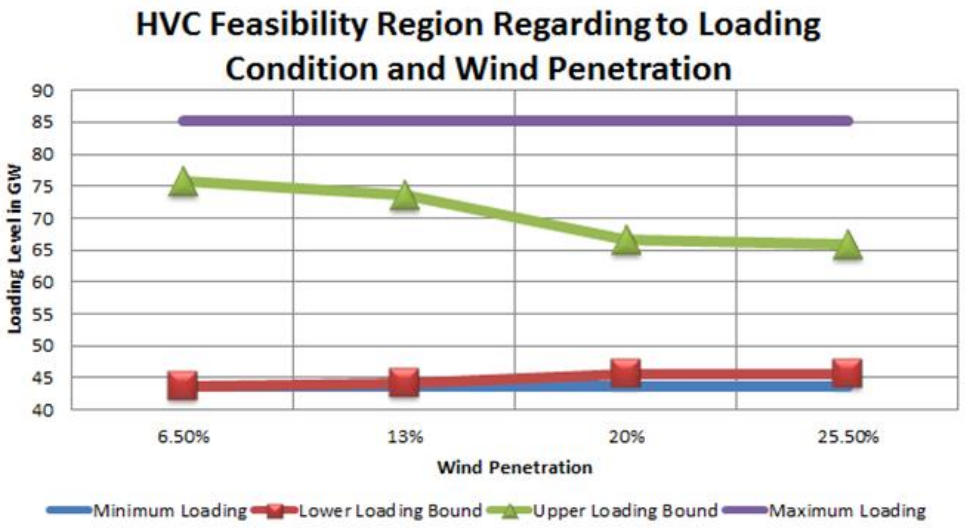

Fig. 6.9 Approximation of the Proposed HVC

It is clear to grasp from Fig. 6.9 that increase in wind penetration is more influential to HVC functioning under stressed system conditions. Therefore, measures to mitigate reactive deficiency are necessary for HVC implementation with simultaneous occurrence of high wind penetration and intensive loading level. Those measures include dynamic VAR compensation such as SVC and Static Synchronous Compensator (STATCOM) and integration of HVDC overlay network to mitigate transmission congestions and reduce losses. While the former is often used to resolve local reactive shortage and requires constant maintenance and upgrades, the latter, with the right kind of converter technology and application of converter regulation, can be a one-time solution to both regional and system wide reactive deficiency.

6.3 Chapter Summary

This chapter showed the effectiveness of the proposed HVC in managing a wide range of operating conditions with over 20% of wind penetration. The control results are interpreted via analysis of regulation actions and the feasibility region of the proposed control regarding to operation conditions is discussed. Since the voltage\VAR regulation initiated by the HVC requires sufficient reactive resources in order to function properly, the proposed control can only deliver satisfactory performances without simultaneously occurrence of high wind penetration and intensive loading. However, the uncontrollable cases only constitute approximately 2% of all yearly-round scenarios and emerge consecutively as rare segments in April and August. Therefore, they do not impair the overall robustness of the proposed scheme. Moreover, those uncontrollable cases can be covered extra switching actions from operators such as load curtailment and generation startup. For cases with higher wind integration, a HVDC overlay network is implemented in the next chapter to support HVC on cases with over 40% of wind penetration with the help of pre-event VAR injection. This studied wind penetration level has exceeded the expected level for 2050 US power grid.

7. Discussions on HVC with Ultra High Wind Penetration and HVDC Overlay

This chapter explores the operation mechanism of the proposed hierarchical voltage control with implementation of HVDC overlay. The DC overlay presented in this chapter is a 7-terminal loop network shown in Fig. 4.10. Since LCC converters are used, the DC terminals will consume reactive power in normal operation. The automatic tap changing of converter end transformer is hence utilized to reduce the reactive consumption of converters. As to accommodate the expectation of more than 35% of wind penetration in US grid proposed by DOE. A base case IV where wind output accounts for 43% of total generation is created to demonstrate the capability of HVC in managing grids with hybrid transmission and ultra-high wind penetration.

With approximately 600MW transferred by DC passage, the traffic congestion on COI intertie was relieved. Hence, aggravated reactive loss around COI area no longer contributes to undesirable voltage dip. The only factor that constrains the security margin of the system becomes the reactive capability of the power plants. As wind power consisting over 40% of total generation, the manageable reactive resources in the system are limited. Therefore, in order to successfully carry out the HVC and obtain satisfactory control performance, extra system support devices including fix shunts, synchronous condensers and back up generators are deployed to build base case IV. To ensure convenience in scenario capture and analysis, switching logics are also developed for those devices to coordinate with each other and adapt to evolving operating conditions. The proposed voltage control would then be executed on each scenarios captured consecutively over a period of time to validate its performance in securing the system with ultra high wind penetration and HVDC overlay.

This chapter will emphasis on the modeling of HVDC overlay as well as the system modifications introduced to realize the long term effectiveness of HVC regulation under over 40% of wind penetration. At last, the preliminary regulation results will be displayed and analyzed at the end of the chapter to give insights on future development of wide area voltage management with high renewable participation and hybrid transmission network.

7.1 Modeling of HVDC Overlay

7.1.1 Representation of the General Model

The HVDC overlay presented in this dissertation consist of line commutating converters only. Though previously determined as known parameters, the power transfer on each DC link varies a little angle

difference at bit due to transmission losses and converter participation factors. As the participation factors are the same for all the converters, the allocation of power flow on each link completely depends on DCPF [206] where the line impedance and the bus angle difference plays the major role. With branch impedance giving in Table 4.5 and 4.6, the active flow on each DC link can be calculated via (7-1)

$$P_{kj} = B_{kj}\left(\theta_k - \theta_j\right) \tag{7-1}$$

where B is the nodal admittance matrix. The calculation results are shown in Fig. 7.1.

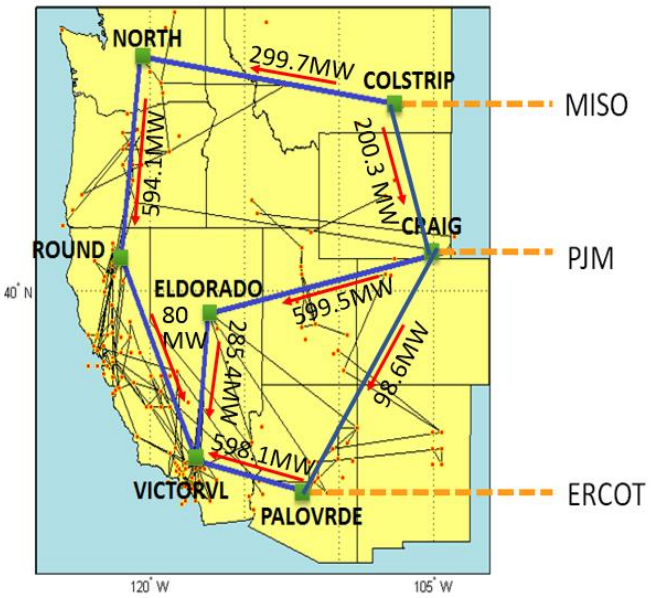

Fig. 7.1 Actual Power Transfer on the DC Links

The HVDC overlay as a stand alone network needs to maintain the balance on each node, namely the power import at each node shall equal to the sum of loss and export. Hence exchanging power with AC transmission is necessary. The DC overlay is exchanging power with the AC system as Table 7.1 lists.

Table 7.1 Power Exchanges between DC overlay and AC Interconnection

Station	COLSTRIP	NORTH	CRAIG	ROUND	VICTORVL	PALOVRDE	ELDORADO
Power Exchange	500 MW	300 MW	500 MW	500 MW	942 MW	500 MW	300 MW
Flow Direction	From AC	From AC	From AC	To AC	To AC	From AC	To AC

Table 7.1 suggests the DC overlay injects power from the north and southeast and feeds energy to load centers in and around California. Usually, for each station, the capability is selected the same as the predefined power exchange value, except for station VICTORVL, serving as the slack node of the DC network, the power going through it cannot be pre-defined as other stations. Thus, the capability of the slack station is round up to 1000 MW to ensure sufficient allowance for operating condition changes. Under abnormal operating condition such as current reversal and significant converter voltage dip, the whole HVDC is blocked [189]. This avoids excessive reactive loss due to the commutation failure and aggravation of the low voltage issue in the system. When the grid complication is resolved, the converters will regain control and the HVDC overlay will resume normal operation when the currents at all the converters are ramped back to a desired restart value. Here the ramping rate for current is given as three pu per second and the minimum current for DC restart is 30 amps as shown Fig. 7.2.

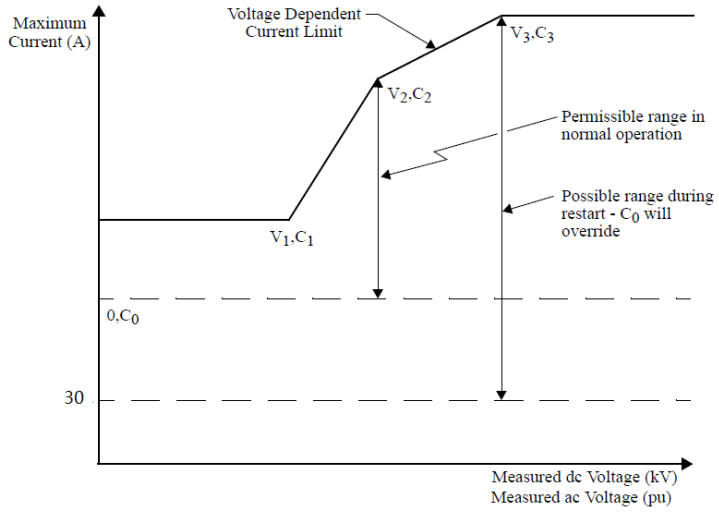

Fig. 7.2 Voltage Dependent Current Limit for HVDC Restart and Operation

As illustrated in Fig. 7.2, the DC current is limited at each stage of recovery. This ensures a smooth re-establishment of HVDC operation and meanwhile allows DC network to be operated at reduced order. This increases the adaptability of the HVDC link and the ability of the system to withstand disturbances. The voltage and current limits for restarting each DC converter is listed Table 7.2. Those limits shape the dynamic behavior of the DC overlay.

Table 7.2 Voltage/Current Limit for Each DC Link of the HVDC Overlay

Station	COLSTRIP	NORTH	CRAIG	ROUND	VICTORVL	PALOVRDE	ELDORADO
C_0 (Amps)	300	180	300	300	300	300	180
V_1 (kV)	200	200	200	200	200	200	200
V_2 (kV)	420	420	420	420	420	420	420
V_3 (kV)	500	500	500	500	500	500	500
C_1 (Amps)	675	405	675	675	1350	675	405
C_2 (Amps)	900	540	900	900	1800	900	540
C_3 (Amps)	1012.5	607.5	1012.5	1012.5	2025	1012.5	607.5

It can be seen in table 6.2 that the productions of V_3 and C_3 for each converter station are always greater than its maximum rating. This is to enable overloading capabilities for DC converters.

7.1.2 Representation of Automatic DC Tap Changing

In PSSE, the multi-terminal HVDC is modeled with DC transformers with tap changers. Once the transformer ratio is determined, the tap changer can adjust automatically during load flow analysis to achieve the desired DC voltage while keep commutating angle within limits. As the reactive power consumed by converter is computed as the product of outfeed power P_c and ψ_c, which is the phase angle between the AC voltage and fundamental AC current calculated by neglecting the commutation overlap via (7-3) to (7-5).

$$Q_c = P_c \tan\varphi_r \tag{7-2}$$

$$\varphi_r = \cos^{-1}\left(\frac{V_{cr}}{V_{cor}}\right) \tag{7-3}$$

$$V_{cor} = 1.35 V_c t_c tap_c \tag{7-4}$$

$$V_{cr} = V_{cor}\cos\alpha - \frac{3X_{cr}}{\pi} I_d \tag{7-5}$$

The V_c in (7-4) denotes the AC voltage of the converter, which aligns with V_{cor}. Since the adjustment of tap ratio would normally change the load flow convergence point, V_{cor} will be deviated from its last value and firing angle α will be adjusted to maintain constant V_{cr} when the DC power transfer is fixed. The deviation on V_{cor} modifies the value of $Q_{c,}$ which refers to the reactive power injected into the converter. Overall, when applying automatic DC tap adjustment, the optimum operating firing angles of rectifier can be located, and the reactive consumptions at each converter station will be changed accordingly.

In Matlab, where the HVC is launched on scenarios to re-dispatch plant POI voltages, the DC transformers are ignored during HVDC modeling [207]. Instead, the HVDC links are modeled as branches with dummy generators as shown in Fig. 7.3.

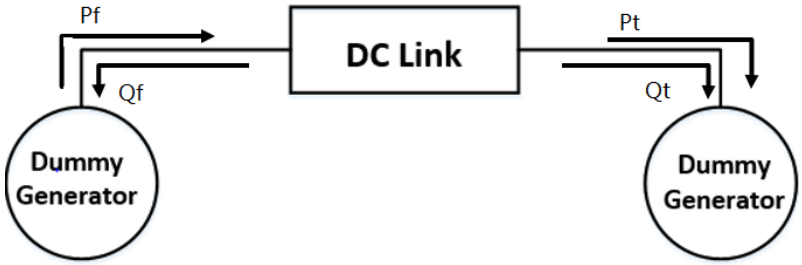

Fig. 7.3 Representation of HVDC Links in Matlab

In Fig. 6.3, P_f and P_t are active power flowing from the rectifier bus and flowing into the inverter bus with Q_f and Q_t denoting the reactive power injected into the converter AC buses. Since converters always consumes MVAR, Q_f and Q_t are written as negative in Matlab, a certain slack is given to the reactive consumptions in converter stations so that during control procedure the reactive power flowing into the HVDC overlay can be adjusted whenever the static voltage profile changes. This is to reach the same flexibility on HVDC regulation as in PSS/E, where the automatic tap changers modifies the reactive consumption of each station when necessary.

The active power loss of a HVDC link in Matlab, is linearly dependent on its power transfer as shown in (7-6)

$$p_{loss} = p_f - p_t = l_1 p_f + l_0 \tag{7-6}$$

Coefficients l_0 and l_1 are calibrated to make sure P_{loss} matches the load flow solution from PSS/E. As long as under normal operation, the power transfer on the overlay network would maintain the same, hence the representation of active flow on DC network is always accuracy in Matlab under steady state.

7.2 System Modification to Realize Ultra High Wind Penetration

In order to implement wind generation that accounts for 43% of the total system supply, new locations are chosen as wind farm sites with all their original thermal power replaced by wind energy. Meanwhile, wind generation is taking a higher share in the old wind farm sites. Therefore, extra reactive resources like back up units and synchronous condensers are utilized to ensure adequate reactive supply. To maintain the balance between reactive supply and demand for different scenarios, switching logics are deployed for synchronous condensers and shunt capacitors to act according to operating conditions.

7.2.1 Implementation of Ultra High Wind Penetration

Table 7.3 shows the details of wind farms in base case IV--a case created to for HVC validation with ultra-high wind penetration and hybrid transmission.

Table 7.3 Locations and Capacities of Wind Farms and Conventional Plants Connected in Parallel

Station	Wind Capacity	Wind output	conventional capacity	Conventional Output
CRAIG	2100 MW	1048 MW	0 MW	0 MW
FOURCORN	4500 MW	2160 MW	0 MW	0 MW
HAYDEN	4500 MW	2050 MW	0 MW	0 MW
SJUAN	1590MW	962 MW	0 MW	0 MW
PARDEE	3600 MW	2200 MW	0 MW	0 MW
NAUGHT	900 MW	445 MW	0 MW	0 MW
CORONADO	1350 MW	600 MW	365.5 MW	200 MW
CANAD	3000 MW	2124.16 MW	5552 MW	2326.84 MW
GMAIN	2100 MW	1300 MW	4754 MW	3180 MW
BRIDGER	1050 MW	700 MW	1019 MW	940 MW
MONTANA	2115 MW	1500 MW	2340 MW	1410 MW
DALLES	1710 MW	1178.6 MW	265 MW	122.8 MW
JOHN DAY	4800 MW	2369.42 MW	6301 MW	3121.6 MW
THE NORTH	3600 MW	3001.78 MW	8623MW	6858.22 MW
TEVATR2	1650MW	1068.56 MW	4731 MW	2398 MW
LITEHIPE	4200 MW	2100 MW	3726 MW	1095 MW
MOHAVE	2250 MW	1470 MW	424 MW	210 MW
Total G	45.015 GW	26.278 GW	37.836 GW	21.862 GW

The first six rows in the above table lists the details of the newly added wind farm sites. The total wind generation rounds up to 26GW in case IV. The integrated wind farms are all subject to the FERC regulation on large generator interconnection [17], which places a hard limit on the power factor at a wind plant POI. This contributes to the reduction in the reactive reserve of the system. Therefore, modifications are made in this case for easier load flow convergence and convenience in scenario development.

7.2.2 System Modifications

In order to provide sufficient reactive reserve, four more synchronous condensers with ±1500MVAR output capability were integrated in addition to the two units mentioned in section 4.1. As shown in Table 7.4, most of newly-added condensers are located in areas either with concentrated wind power like Canada or huge load centers like California. Two of them are interconnected to Montana and Northwest where long transmission lines are placed. This is to mitigate the voltage drop due to excessive reactive loss over long distance AC transmission.

Table 7.4 Location and Capability of Synchronous Condensers in Base Case IV

PV bus #	193	194	201	202	203	204
Location	Montana	PG&E	Canada	SCE	LDWP	Northwest
Capability in MVAR	±1500	±1500	±1500	±1500	±1500	±1500
Switchable	No	Yes	No	No	No	No

As listed in the above Table, condenser connected at Bus 194 is switchable. Hence, a switching logic is created for it to coordinate with local shunts and maintain acceptable areal voltage profile. The details of the switching logic is elaborated in Fig. 7.4.

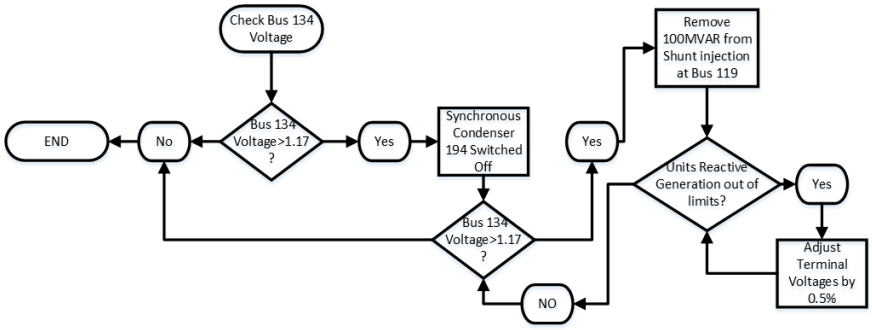

Fig. 7.4 An example of Condenser Switching Logics

Usually, a switchable condenser is turned off is during off-peak hours to avoid over voltage and switched back on during peak hours to provide system with extra reactive support. The reactive generation of local units are checked whenever there is a switching action to make sure none of the generators is exhausted in reactive reserve.

In addition to synchronous condensers, more dynamic VAR is introduced to base case IV by the back up units. The mechanism to decide number of online units and back up generation allocation is similar to what described by equations 5.1-5.5. However, with the back-up capacity doubled compared with what shown in Table 5.1, the maximum limit of the round-up ratio $\bar{q}$ between the number of back up units and on-duty units becomes 8 as listed in the following equations.

$$N = \frac{P\_dispatched}{S\_original} - 1 \geq 0 \tag{7-7}$$

$$C = \frac{S\_backup}{S\_original} \tag{7-8}$$

$$0 \leq \bar{q} = \frac{N}{C} \leq 8, \quad \bar{q} = 1,2 \cdots 8 \tag{7-9}$$

Where P^{disp} refers to the required generation from this plant for maintaining power balance and S^{back} is the capacity of each backup unit prepared for the plant.

7.3 Preliminary Control Results

When applying the proposed control together with the pre-event VAR injection scheme to the base case IV, a margin increase of 215 MW is found as shown in Table 7.5.

Table 7.5 HVC Performance on Base Cases with Ultra High Wind Penetration and HVDC

	Wind Penetration	Transmission	Original Margin (MW)	Controlled Margin (MW)	Margin Increase (MW)
II	12%	AC only	1478.2	1607.1	128.9
III	22%	AC only	1317.2	1405.1	87.9
IV	43%	AC and DC	1003.0	1218.0	215.0

This is a promising result for the effectiveness of the proposed HVC on a single snapshot. Twenty-five scenarios representing operating conditions throughout a working day in the summer are then generated to see if the proposed regulation scheme is adaptable to variations on system conditions. The detail of the captured scenarios are illustrated in Fig. 7.5.

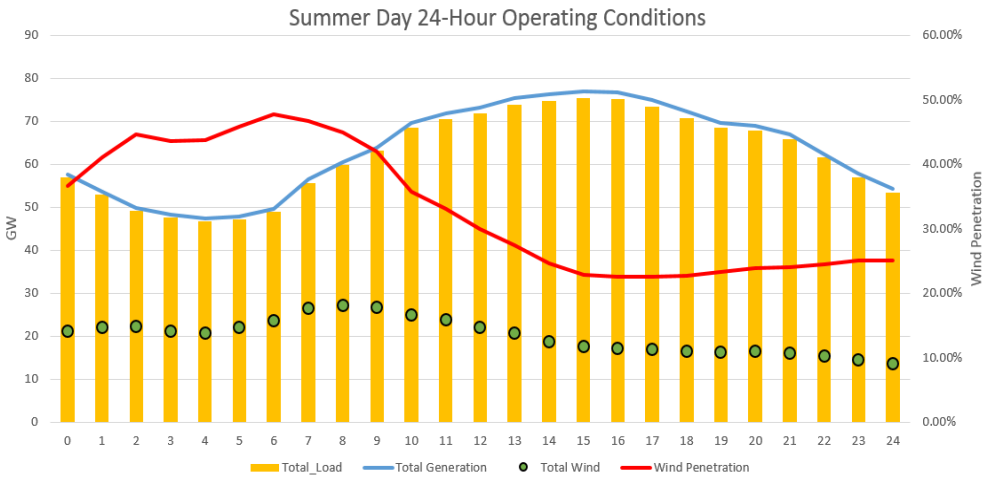

Fig. 7.5 24-hour Scenario Capture of WECC Test System

It can be seen from Fig. 7.5 that in the captured snapshots, the loading level range from 46GW to 76 GW, covering 98% of the yearly round scenarios as exempted in Chapter 6. The wind penetration go as high as 48%, almost doubled highest wind penetration level found in the cases studied in Chapter 6. This means the proposed HVC is now trying having its feasibility region expanded and managing cases under more extreme conditions. The following figure shows how well the proposed HVC can perform on those cases. The performances of the HVC here are evaluated by the increase in COI transfer capability.

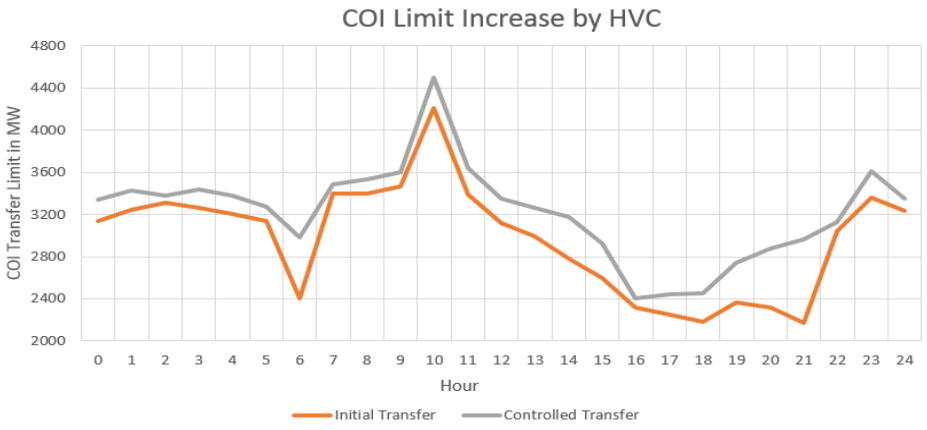

Fig. 7.6 COI Limit Increase by HVC on 24-Hour Scenarios

Fig. 7.6 validates the adaptability of the HVC and its ability to work with HVDC overlay in dealing with extreme operating conditions. However, when checking the security margin of the cases, it is obvious that some cases are captured with negative initial margin due to simultaneous occurrence of high loading level and high wind penetration. Some extra control actions such as Remedy Action Scheme (RAS) and load shedding may be necessary to bring those scenarios back to initial security. Nevertheless, they are outside of the dissertation's scope and therefore not elaborated in this chapter. Despite the initially insecure snapshots, the proposed HVC did bring up the security margin for all the cases captured along the day as shown in Fig. 7.7.

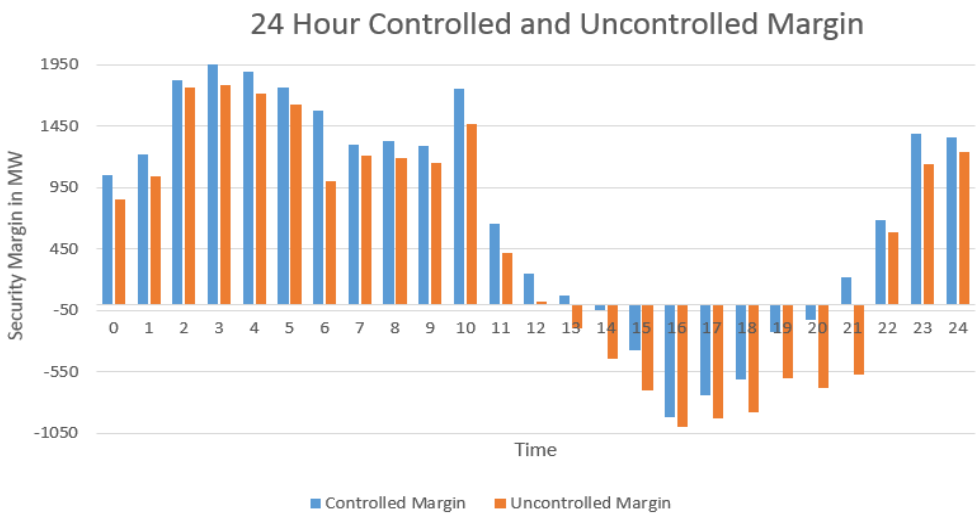

Fig. 7.7 Security Margin Change Enabled by the Proposed HVC with Ultra High Wind Penetration

For two of the initially insecure cases, the HVC was even able to restore the security by efficiently managing the reactive resources in the system. For rest of the cases with initial insecurity, the HVC was able to reduce the magnitude of negative margin, which indicates the HVC can help the system operators to amend the system under extremely stressed conditions. This again verifies the capability of the HVC to work with HVDC overlay and achieve satisfactory regulation performance under ultra-high wind penetration.

7.4 Chapter Summary

This chapter discussed how the proposed control scheme manage systems representing 2050 power grid where more than 35% of energy supply comes from wind generation. The preliminary study results prove that when working with HVDC overlay to resolve the congestion issue around COI intertie and with pre-event VAR injection to provide extra local reactive support, this propose control can adapt to operating

conditions with up to 48% of wind penetration. Hence, introduction of hybrid transmission and allocation of local reactive supports in coordination with the proposed HVC can be considered as an alternative to realize wide area voltage management for a system with extremely limited dynamic VAR resources. This finding provides reference for the development of regulation scheme for future power grids where HVDC transmissions and ultra-high renewable penetrations are to be massively placed into commission.

8. Conclusions

With the proposed control validated on the test system developed with equivalence to a real power grid in both parameter settings and real-time operating conditions, the dissertation notes the following observations.

- The test system derived from the WECC 179-bus model shows good equivalence with actual power grid data and is capable of modeling the future power network with a high level of renewables and HVDC transmission system. Hence, it is ready to serve as test-bed for research and academic uses involving contingency simulation and control algorithm validation for power grid in the next generation.
- The application of the proposed control on the test system is successful with all yearly-round scenarios solvable via application of direct interior-point ORPF and control effect boosted by adoption of sensitivity-based pilot bus selection. The direct IP ORPF avoided control failures and hence can serve as a baseline for online state estimation while the sensitivity-based pilot bus selection improved the control efficiency by focusing regulation on system weak parts.
- The PCA-based regression method designed for formulation of the dynamic constrained OPF successfully mapped system attributes to the target value with explicit expressions and negligible errors, which allowed the solution procedure of tertiary OPF and enhanced the accuracy of the proposed control. This proved to have great capability in pattern generalization and noise rejection, as well as potentials for fast execution. It is suitable to support future online dynamic security assessment and control.
- The proposed control guided by the PCA-based tertiary OPF proved effective in managing a wide range of operating conditions with over 20% of wind penetration. As incorporated regulation on wind farm reactive reference in the control loop, the proposed HVC makes the most use of the available reactive resources in the system where large portions of conventional units are replaced by wind turbines. Though its performances are still affected by reactive reserve in the system, the resulting uncontrollable snapshots are few and can be covered by the coordination with HVDC overlay.
- Coordinated with pre-event VAR injection, the proposed HVC proved effective in managing the system with HVDC overlay regardless of the initial security. This is due to the flexibility of hybrid transmission where the consumption of reactive power on converters can be adjusted according to system conditions. This has expanded the feasibility region of the proposed HVC as now it can manage systems with up to 48% wind penetration. This level of renewable level meets future

renewable targets and hence, the proposed control scheme provides an alternative for wide area voltage/VAR regulation for future grids with very high levels of wind penetration and flexible transmission.

Bibliography

[1] T. J. Price, "James Blyth—Britain's first modern wind power pioneer," *Wind engineering*, vol. 29, no. 3, pp. 191-200, 2005.

[2] R. a. M. B. Wiser, "2014 wind technologies market report," 2015.

[3] X. Lu, M. B. McElroy, and J. Kiviluoma, "Global potential for wind-generated electricity," *Proceedings of the National Academy of Sciences*, vol. 106, no. 27, pp. 10933-10938, 2009.

[4] W. E. Fundation. *U.S. Wind Industry Fast Facts*. Available: http://windenergyfoundation.org/about-wind-energy/us-wind-industry-fast-facts/

[5] Statista. (2015). *Total Electricity End Use in the U.S.from 1975 to 2015 (in billion kilowatt hours)*. Available: http://www.statista.com/statistics/201794/us-electricity-consumption-since-1975/

[6] E. Efficiency, "20% Wind Energy by 2030: Increasing Wind Energy's Contribution to US Electricity Supply," DOE/GO-102008-2567, US Department of Energy, May. http://www. nrel. gov/docs/fy08osti/41869. pdf2008.

[7] G. W. E. Council, "Global wind report: Annual market update 2011," *Global Wind Energy Council: Brussels, Belgium*, 2012.

[8] G. W. E. C. (GWEC), "Global Wind Statistics 2015," 2016.

[9] A. W. E. Association, "US Wind Industry Annual Market Report Year Ending 2015," *American Wind Energy Association*, 2015.

[10] D. o. E. (DOE), "Wind Vision: A New Era for Wind Power in the United States," April 2015 2015.

[11] H. Li and Z. Chen, "Overview of different wind generator systems and their comparisons," *IET Renewable Power Generation*, vol. 2, no. 2, pp. 123-138, 2008.

[12] E. H. Camm *et al.*, "Characteristics of wind turbine generators for wind power plants," in *2009 IEEE Power & Energy Society General Meeting*, 2009, pp. 1-5.

[13] A. D. Hansen and L. H. Hansen, "Market penetration of wind turbine concepts over the years," in *Proc. European Wind Energy Conference and Exhibition 2007*, 2007.

[14] A. D. Hansen and G. Michalke, "Fault ride-through capability of DFIG wind turbines," *Renewable energy*, vol. 32, no. 9, pp. 1594-1610, 2007.

[15] P. Tielens and D. Van Hertem, "Grid inertia and frequency control in power systems with high penetration of renewables," 2012.

[16] A. Ulbig, T. S. Borsche, and G. Andersson, "Impact of low rotational inertia on power system stability and operation," *IFAC Proceedings Volumes*, vol. 47, no. 3, pp. 7290-7297, 2014.

[17] *Standardization Large Generator Interconnection Agreement (LGIA)*, 2005.

[18] O. Peake, "The history of high voltage direct current transmission," *Australian Journal of Multi-disciplinary Engineering*, vol. 8, no. 1, pp. 47-55, 2010.

[19] R. Rudervall, J. Charpentier, and R. Sharma, "High voltage direct current (HVDC) transmission systems technology review paper," *Energy week*, vol. 2000, p. 2, 2000.

[20] Siemens. *HVDC Classic*. Available: http://www.energy.siemens.com/hq/en/power-transmission/hvdc/hvdc-classic.htm#content=Low%20Losses

[21] K. Meah and S. Ula, "Comparative evaluation of HVDC and HVAC transmission systems," in *Power Engineering Society General Meeting, 2007. IEEE*, 2007, pp. 1-5: IEEE.

[22] G. Tang, X. Luo, and X. Wei, "Multi-terminal HVDC and DC-grid technology," in *Zhongguo Dianji Gongcheng Xuebao(Proceedings of the Chinese Society of Electrical Engineering)*, 2013, vol. 33, no. 10, pp. 8-17: Chinese Society for Electrical Engineering.

[23] X. Chen, "Wind Power Integration Using Multi-terminal HVDC Technology," Doctor of Philosophy Dissertation, Power System and Its Automation, Huazhong University of Science & Technology, Wuhan P.R.China, 2012.

[24] X. Chen *et al.*, "Integrating wind farm to the grid using hybrid multiterminal HVDC technology," *IEEE Transactions on Industry Applications*, vol. 47, no. 2, pp. 965-972, 2011.

[25] A. Hammad, R. Minghetti, J.-P. Hasler, P.-A. Eicher, R. Bunch, and D. Goldsworthy, "Controls modelling and verification for the Pacific Intertie HVDC 4-terminal scheme," *IEEE transactions on power delivery*, vol. 8, no. 1, pp. 367-375, 1993.

[26] C. Thio, "Nelson River HVDC Bipole-Two Part I-System Aspects," *IEEE Transactions on Power Apparatus and Systems*, no. 1, pp. 165-173, 1979.

[27] V. C. Billon, J. Taisne, V. Arcidiacono, and F. Mazzoldi, "The Corsican tapping: from design to commissioning tests of the third terminal of the Sardinia-Corsica-Italy HVDC," *IEEE Transactions on Power Delivery*, vol. 4, no. 1, pp. 794-799, 1989.

[28] D. McCallum, G. Moreau, J. Primeau, and D. Soulier, "Multiterminal integration of the Nicolet converter station into the Quebec-New England phase II HVDC transmission system," in *INTERNATIONAL CONFERENCE ON LARGE HIGH VOLTAGE ELECTRIC SYSTEMS*, 1994, vol. 1, pp. 14-103.

[29] T. D. Corporation, "Shin-Shinano 3-Terminal Voltage Sourced Converter based Back to Back System (VSC-BTB)," 30613-1.

[30] H. Rao, "Architecture of Nan'ao multi-terminal VSC-HVDC system and its multi-functional control," *CSEE Journal of Power and Energy Systems*, vol. 1, no. 1, pp. 9-18, 2015.

[31] L. Yanan, J. Weiyong, Y. Shifeng, and Z. Xin, "System design of Zhoushan multi-terminal VSC-HVDC transmission project," *High Voltage Engineering*, vol. 40, no. 8, pp. 2490-2496, 2014.

[32] C. Barker *et al.*, "Multi-terminal operation of the South–West link HVDC scheme in Sweden," in *CIGRE Canada Conference, Montreal, Canada*, 2012.

[33] T. Hansen, "Tres Amigas technology holds promise for expanding renewable energy supply," *Electric Light & Power*, 2010.

[34] ABB. *North-East Agra Will Supply Electricity to Serve 90 Million People*. Available: http://new.abb.com/systems/hvdc/references/north-east-agra

[35] S. Cole *et al.*, "A European supergrid: present state and future challenges," in *Proc. Power Systems Computation Conf.(PSCC), Stockholm, Sweden*, 2011.

[36] D. Van Hertem and M. Ghandhari, "Multi-terminal VSC HVDC for the European supergrid: Obstacles," *Renewable and sustainable energy reviews*, vol. 14, no. 9, pp. 3156-3163, 2010.

[37] W. Zhang, Y. TANG, and N. ZENG, "Multi-Terminal HVDC Transmission Technologies and Its Application Prospects in China [J]," *Power System Technology*, vol. 9, pp. 1-6, 2010.

[38] O. Swaitti, "Assessing the impacts of increasing penetration of HVDC lines on power system reliability," Citeseer, 2007.

[39] Y. L. Yin Lei, Yalong Li, Yilu Liu,Kevin Tomsovic,Fei Wang, "A Preliminary Study of Building a Transmission Overlay for Regional US Power Grid," presented at the 2015 IEEE PES Power & Energy Society General Meeting, Denver,CO,USA, July 27th 2015, 2015.

[40] J. Paul, J. Leost, and J. Tesseron, "Survey of the secondary voltage control in France: present realization and investigations," *Power Systems, IEEE Transactions on*, vol. 2, no. 2, pp. 505-511, 1987.

[41] J. Paul, C. Corroyer, P. Jeannel, J. Tesseron, F. Maury, and A. Torra, "Improvements in the organization of secondary voltage control in France," *CIGRE Session Paris*, pp. 39-03, 1990.

[42] P. Marannino, F. Zanellini, M. Merlo, S. Corsi, M. Pozzi, and G. Dell'Olio, "Evaluation of load margins with respect to voltage collapse in presence of secondary and tertiary voltage regulation," *Bulk Power system Dynamics and Control–V*, pp. 26-31, 2001.

[43] E. Androulidakis and A. Alexandridis, "Primary Level and Secondary Level Coordinated Control of Power Systems."

[44] J. Thorp, M. Ilic-Spong, and M. Varghese, "Optimal secondary voltage-var control using pilot point information structure," in *Decision and Control, 1984. The 23rd IEEE Conference on*, 1984, pp. 462-466: IEEE.

[45] P. Lagonotte, J. Sabonnadiere, J. Leost, and J. Paul, "Structural analysis of the electrical system: application to secondary voltage control in France," *Power Systems, IEEE Transactions on*, vol. 4, no. 2, pp. 479-486, 1989.

[46] H. Lefebvre, D. Fragnier, J. Boussion, P. Mallet, and M. Bulot, "Secondary coordinated voltage control system: feedback of EDF," in *Power Engineering Society Summer Meeting, 2000. IEEE*, 2000, vol. 1, pp. 290-295: IEEE.

[47] R. E. Shanshan Liu, Navin Bhatt, Joe H. Chow, "Overview of Advanced Voltage Control," 2014.

[48] S. Engelhardt, I. Erlich, C. Feltes, J. Kretschmann, and F. Shewarega, "Reactive power capability of wind turbines based on doubly fed induction generators," *Energy Conversion, IEEE Transactions on,* vol. 26, no. 1, pp. 364-372, 2011.

[49] T. Lund, P. Sørensen, and J. Eek, "Reactive power capability of a wind turbine with doubly fed induction generator," *Wind energy,* vol. 10, no. 4, pp. 379-394, 2007.

[50] N. FERC, "Arizona—Southern California Outages on September 8, 2011: Causes and Recommendations," 2012.

[51] *System Performance TPL-001-WECC-RBP-2 Regional Business Practice* 2011.

[52] W. E. C. Council, "Guide to WECC/NERC Planning Standards ID: Voltage Support and Reactive Power," ed, 2006.

[53] J. L. Rueda and I. Erlich, "Impacts of large scale integration of wind power on power system small-signal stability," in *Electric Utility Deregulation and Restructuring and Power Technologies (DRPT), 2011 4th International Conference on*, 2011, pp. 673-681: IEEE.

[54] Y. Mishra, S. Mishra, M. Tripathy, N. Senroy, and Z. Dong, "Improving stability of a DFIG-based wind power system with tuned damping controller," *IEEE Transactions on Energy Conversion,* vol. 24, no. 3, pp. 650-660, 2009.

[55] C. Martinez, G. Joos, and B. Ooi, "Power system stabilizers in variable speed wind farms," in *2009 IEEE Power & Energy Society General Meeting*, 2009, pp. 1-7: IEEE.

[56] P. He, "Investigations on Impacts and Control Strategies of Power System Stability with Wind Power Integration," Doctor of Philosophy, Department of Electrical Engineering, Zhejiang University, 2014.

[57] S. Kincic *et al.*, "Bridging the gap between operation and planning models in WECC," in *Power and Energy Society General Meeting (PESGM), 2016*, 2016, pp. 1-5: IEEE.

[58] J. E. Price and J. Goodin, "Reduced network modeling of WECC as a market design prototype," in *Power and Energy Society General Meeting, 2011 IEEE*, 2011, pp. 1-6: IEEE.

[59] ERCOT. *Wind Power Production - Actual 5-minute averaged values*. Available: http://mis.ercot.com/misapp/GetReports.do?reportTypeId=13071&reportTitle=Wind%20Power%20Production%20-%20Actual%205-Minute%20Averaged%20Values%20&showHTMLView=&mimicKey

[60] F. F. Wu, K. Moslehi, and A. Bose, "Power system control centers: Past, present, and future," *Proceedings of the IEEE,* vol. 93, no. 11, pp. 1890-1908, 2005.

[61] W. Zhang, F. Li, and L. M. Tolbert, "Review of reactive power planning: objectives, constraints, and algorithms," *IEEE Transactions on Power Systems,* vol. 22, no. 4, pp. 2177-2186, 2007.

[62] P. Kundur, N. J. Balu, and M. G. Lauby, *Power system stability and control*. McGraw-hill New York, 1994.

[63] R. L. Hauth, *Static Reactive Power Compensators for High Voltage Power Systems*. General Electric Company, 1981.

[64] C. Report, "Static VAR Compensators," Paris1986.

[65] J. Piret, J. Antoine, M. Stubbe, and N. Janssens, "The study of a centralized voltage control method applicable to the Belgian system," in *INTERNATIONAL CONFERENCE ON LARGE HIGH VOLTAGE ELECTRIC SYSTEMS*, 1992, vol. 2, pp. 39-201.

[66] O. A. Mousavi and R. Cherkaoui, "Literature survey on fundamental issues of voltage and reactive power control," *Ecole Polytechnique Fédérale de Lausanne: Lausanne, Switzerland*, 2011.

[67] J. Van Hecke, N. Janssens, J. Deuse, and F. Promel, "Coordinated voltage control experience in Belgium," *CIGRE Session Report 38*, vol. 111, 2000.

[68] N. Hatziargyriou, H. Asano, R. Iravani, and C. Marnay, "Microgrids," *IEEE power and energy magazine*, vol. 5, no. 4, pp. 78-94, 2007.

[69] N. Janssens, "Tertiary and secondary voltage control for the Belgian HV system," in *International Practices in Reactive Power Control, IEE Colloquium on*, 1993, pp. 8/1-8/4: IET.

[70] S. Corsi, "The secondary voltage regulation in Italy," in *Power Engineering Society Summer Meeting, 2000. IEEE*, 2000, vol. 1, pp. 296-304: IEEE.

[71] T. V. Cutsem, "An overview of electric power systems," Introduction to Electric Power and Energy SystemsLiège, Belgium: University of Liège, 2015. [Online]. Available.

[72] S. Corsi, M. Pozzi, C. Sabelli, and A. Serrani, "The coordinated automatic voltage control of the Italian transmission Grid-part I: reasons of the choice and overview of the consolidated hierarchical system," *Power systems, IEEE Transactions on*, vol. 19, no. 4, pp. 1723-1732, 2004.

[73] S. Corsi, M. Pozzi, M. Sforna, and G. Dell'Olio, "The coordinated automatic voltage control of the Italian transmission Grid-part II: control apparatuses and field performance of the consolidated hierarchical system," *Power systems, IEEE Transactions on*, vol. 19, no. 4, pp. 1733-1741, 2004.

[74] H. Vu, P. Pruvot, C. Launay, and Y. Harmand, "An improved voltage control on large-scale power system," *IEEE transactions on power systems*, vol. 11, no. 3, pp. 1295-1303, 1996.

[75] J. Sancha, J. Fernandez, F. Martinez, and C. Salle, "Spanish practices in reactive power management and voltage control," in *International Practices in Reactive Power Control, IEE Colloquium on*, 1993, pp. 3/1-3/4: IET.

[76] J. Sancha, J. Fernandez, and J. Abarca, "Secondary voltage control: analysis, solutions and simulation results for the Spanish transmission system," *Power Systems, IEEE Transactions on*, vol. 11, no. 2, pp. 630-638, 1996.

[77] L. Layo, L. Martin, and M. Álvarez, "Final implementation of a multilevel strategy for voltage and reactive control in the Spanish electrical power system," in *Proc. PCI Conf, Glasgow, Scotland, UK*, 2000.

[78] E. L. Miguelez, F. M. E. Cerezo, and L. R. Rodriguez, "On the assignment of voltage control ancillary service of generators in Spain," *IEEE Transactions On Power Systems*, vol. 22, no. 1, pp. 367-375, 2007.

[79] S. Kincic *et al.*, "Impact of massive synchrophasor deployment on reliability coordination and reporting," in *2012 IEEE Power and Energy Society General Meeting*, 2012.

[80] B. Ceci. (2007) SCADA Alternatives for Remote Monitoring. *Pumps and Systems*. 3.

[81] Q.-L. Guo, H.-B. Sun, B.-M. Zhang, and W.-C. Wu, "Power network partitioning based on clustering analysis in Mvar control space," *Dianli Xitong Zidonghua(Autom. Electr. Power Syst.)*, vol. 29, no. 10, pp. 36-40, 2005.

[82] H. Jiawei and M. Kamber, "Data mining: concepts and techniques," *San Francisco, CA, itd: Morgan Kaufmann*, vol. 5, 2001.

[83] J.-L. Chandon and S. Pinson, *Analyse typologique: théories et applications*. Masson, 1981.

[84] H. Sun, Q. Guo, B. Zhang, W. Wu, and J. Tong, "Development and applications of system-wide automatic voltage control system in China," in *Power & Energy Society General Meeting, 2009. PES'09. IEEE*, 2009, pp. 1-5: IEEE.

[85] Q. Guo, H. Sun, J. Tong, M. Zhang, B. Wang, and B. Zhang, "Study of system-wide Automatic Voltage Control on PJM system," in *Power and Energy Society General Meeting, 2010 IEEE*, 2010, pp. 1-6: IEEE.

[86] Q. Guo, H. Sun, M. Zhang, J. Tong, B. Zhang, and B. Wang, "Optimal voltage control of PJM smart transmission grid: Study, implementation, and evaluation," *IEEE Transactions on Smart Grid*, vol. 4, no. 3, pp. 1665-1674, 2013.

[87] M. S. El-Moursi, "A novel line drop secondary voltage control algorithm for variable speed wind turbines," *Wind Energy*, vol. 13, no. 7, pp. 633-655, 2010.

[88] C. W. Taylor, "Line drop compensation, high side voltage control, secondary voltage control-why not control a generator like a static VAr compensator?," in *Power Engineering Society Summer Meeting, 2000. IEEE*, 2000, vol. 1, pp. 307-310: IEEE.

[89] F. Milano, C. A. Canizares, and M. Invernizzi, "Voltage stability constrained OPF market models considering N− 1 contingency criteria," *Electric Power Systems Research*, vol. 74, no. 1, pp. 27-36, 2005.

[90] K. Morison, L. Wang, and P. Kundur, "Power system security assessment," *IEEE Power and Energy Magazine*, vol. 2, no. 5, pp. 30-39, 2004.

[91] L. Wang and K. Morison, "Implementation of online security assessment," *IEEE Power and Energy Magazine,* vol. 4, no. 5, pp. 46-59, 2006.

[92] C. W. Taylor, "The future in on-line security assessment and wide-area stability control," in *Power Engineering Society Winter Meeting, 2000. IEEE*, 2000, vol. 1, pp. 78-83: IEEE.

[93] A. M. Lyapunov, "The general problem of the stability of motion," *International Journal of Control,* vol. 55, no. 3, pp. 531-534, 1992.

[94] A.-A. Fouad and T. Jianzhong, "Stability constrained optimal rescheduling of generation," *IEEE Transactions on Power Systems,* vol. 8, no. 1, pp. 105-112, 1993.

[95] J. STERLING, M. Pai, and P. Sauer, "A methodology of secure and optimal operation of a power system for dynamic contingencies," *Electric machines and power systems,* vol. 19, no. 5, pp. 639-655, 1991.

[96] K. Chandrashekhar and D. Hill, "Dynamic security dispatch: Basic formulation," *IEEE Transactions on Power Apparatus and Systems,* no. 7, pp. 2145-2154, 1983.

[97] A. H. El-Abiad and K. Nagappan, "Transient stability regions of multimachine power systems," *IEEE Transactions on Power Apparatus and Systems,* no. 2, pp. 169-179, 1966.

[98] N. Kakimoto, Y. Ohsawa, and M. Hayashi, "Transient stability analysis of electric power system via Lure-Type Lyapunov function, Parts I and II," *Trans. IEE of Japan,* vol. 98, no. 516, 1978.

[99] A. Llamas, "Assessment of direct methods in power system transient stability analysis for on-line applications," 1992.

[100] H.-D. Chiang, F. Wu, and P. Varaiya, "Foundations of direct methods for power system transient stability analysis," *IEEE Transactions on Circuits and systems,* vol. 34, no. 2, pp. 160-173, 1987.

[101] H.-D. Chiang, F. F. Wu, and P. P. Varaiya, "A BCU method for direct analysis of power system transient stability," *IEEE Transactions on Power Systems,* vol. 9, no. 3, pp. 1194-1208, 1994.

[102] T. J. Overbye and C. L. De Marco, "Voltage security enhancement using energy based sensitivities," *IEEE Transactions on Power Systems,* vol. 6, no. 3, pp. 1196-1202, 1991.

[103] E. De Tuglie, M. Dicorato, M. La Scala, and P. Scarpellini, "A corrective control for angle and voltage stability enhancement on the transient time-scale," *IEEE Transactions on Power Systems,* vol. 15, no. 4, pp. 1345-1353, 2000.

[104] M. La Scala, M. Trovato, and C. Antonelli, "On-line dynamic preventive control: an algorithm for transient security dispatch," *IEEE Transactions on Power Systems,* vol. 13, no. 2, pp. 601-610, 1998.

[105] D. Gan, R. J. Thomas, and R. D. Zimmerman, "Stability-constrained optimal power flow," *IEEE Transactions on Power Systems,* vol. 15, no. 2, pp. 535-540, 2000.

[106] Y. Xia, K. W. Chan, M. Liu, and J. Wu, "Calculation of available transfer capability with transient stability constraints," in *Electric Utility Deregulation, Restructuring and Power Technologies, 2004.(DRPT 2004). Proceedings of the 2004 IEEE International Conference on*, 2004, vol. 1, pp. 128-132: IEEE.

[107] L. Chen, Y. Taka, H. Okamoto, R. Tanabe, and A. Ono, "Optimal operation solutions of power systems with transient stability constraints," *IEEE Transactions on Circuits and Systems I: Fundamental Theory and Applications*, vol. 48, no. 3, pp. 327-339, 2001.

[108] T. B. Nguyen and M. Pai, "Dynamic security-constrained rescheduling of power systems using trajectory sensitivities," *IEEE Transactions on Power Systems*, vol. 18, no. 2, pp. 848-854, 2003.

[109] L. Mingbo, L. Yanhong, and K. Chan, "Transient stability constrained optimal power flow using trajectory sensitivities," *Proceedings of the CSUEPSA*, vol. 19, no. 6, pp. 24-29, 2007.

[110] K. Shubhanga and A. M. Kulkarni, "Determination of effectiveness of transient stability controls using reduced number of trajectory sensitivity computations," *IEEE Transactions on Power Systems*, vol. 19, no. 1, pp. 473-482, 2004.

[111] D. Fang, Y. Xiaodong, S. Jingqiang, Y. Shiqiang, and Z. Yao, "An optimal generation rescheduling approach for transient stability enhancement," *IEEE Transactions on Power systems*, vol. 22, no. 1, pp. 386-394, 2007.

[112] Y.-k. LI and M.-b. LIU, "Trajectory Sensitivity Method for Transient Stability Constrained Optimal Power Flow Under Multi-contingency Condition [J]," *Proceedings of the CSEE*, vol. 16, p. 008, 2009.

[113] A.-A. Fouad and V. Vittal, *Power system transient stability analysis using the transient energy function method*. Pearson Education, 1991.

[114] C. M. Bishop, "Pattern recognition," *Machine Learning*, vol. 128, 2006.

[115] S. R. Safavian and D. Landgrebe, "A survey of decision tree classifier methodology," 1990.

[116] Genc, Istemihan, et al. "Decision tree-based preventive and corrective control applications for dynamic security enhancement in power systems." *IEEE Transactions on Power Systems*, vol. 25, no. 3, 2010, pp 1611-1619

[117] B. Yegnanarayana, *Artificial neural networks*. PHI Learning Pvt. Ltd., 2009.

[118] A. Sittithumwat and K. Tomsovic, "Dynamic security margin estimation with preventive control using artificial neural networks," Washington State University, 2005.

[119] Q. Zhou, J. Davidson, and A. Fouad, "Application of artificial neural networks in power system security and vulnerability assessment," *IEEE transactions on power systems*, vol. 9, no. 1, pp. 525-532, 1994.

[120] A. Conejo, J. De la Fuente, and S. Goransson, "Comparison of alternative algorithms to select pilot buses for secondary voltage control in electric power networks," in *Electrotechnical Conference, 1994. Proceedings., 7th Mediterranean*, 1994, pp. 940-943: IEEE.

[121] V. Arcidiacono, "Automatic voltage and reactive power control in transmission systems," in *Proc. of*, 1983.

[122] C.-T. Lin, "Structural controllability," *IEEE Transactions on Automatic Control*, vol. 19, no. 3, pp. 201-208, 1974.

[123] J. Peschon, D. S. Piercy, W. F. Tinney, and O. J. Tveit, "Sensitivity in power systems," *IEEE Transactions on Power Apparatus and Systems*, no. 8, pp. 1687-1696, 1968.

[124] S. Singh, G. Raju, and A. Gupta, "Sensitivity based expert system for voltage control in power system," *International Journal of Electrical Power & Energy Systems*, vol. 15, no. 3, pp. 131-136, 1993.

[125] A. G. Expósito, J. M. Ramos, J. R. Macías, and Y. C. Salinas, "Sensitivity-based reactive power control for voltage profile improvement," *IEEE Transactions on Power Systems*, vol. 8, no. 3, pp. 937-945, 1993.

[126] H. Sun, B. Zhang, and N. Xiang, "Sensitivity analysis method with on-line applications to EMS," 1995.

[127] A. Conejo, T. Gomez, and J. De la Fuente, "Pilot-bus selection for secondary voltage control," *European Transactions on Electrical Power*, vol. 3, no. 5, pp. 359-366, 1993.

[128] A. Stankovic, M. Ilic, and D. Maratukulam, "Recent results in secondary voltage control of power systems," *IEEE transactions on power systems*, vol. 6, no. 1, pp. 94-101, 1991.

[129] M. Ilic-Spong, J. Christensen, and K. Eichorn, "Secondary voltage control using pilot point information," *IEEE Transactions on Power Systems*, vol. 3, no. 2, pp. 660-668, 1988.

[130] A. Conejo and M. Aguilar, "Secondary voltage control: Nonlinear selection of pilot buses, design of an optimal control law, and simulation results," *IEE Proceedings-Generation, Transmission and Distribution*, vol. 145, no. 1, pp. 77-81, 1998.

[131] H. Sun, B.-M. Zhang, and N. Xiang, "New sensitivity analysis method under quasi-steady-state for power systems," *PROCEEDINGS-CHINESE SOCIETY OF ELECTRICAL ENGINEERING*, vol. 19, pp. 9-13, 1999.

[132] R. Chen *et al.*, "Pilot bus selection in automatic voltage control," *Electric Power Automation Equipment*, vol. 32, no. 9, pp. 111-116, 2012.

[133] R. E. Larson, W. F. Tinney, and J. Peschon, "State estimation in power systems Part I: Theory and feasibility," *IEEE Transactions on Power Apparatus and Systems*, no. 3, pp. 345-352, 1970.

[134] S. Pajic and K. A. Clements, "Power system state estimation via globally convergent methods," *IEEE Transactions on Power Systems,* vol. 20, no. 4, pp. 1683-1689, 2005.

[135] S. Pajic and K. A. Clements, "Globally convergent state estimation via the trust region method," in *Power Tech Conference Proceedings, 2003 IEEE Bologna*, 2003, vol. 1, p. 6 pp. Vol. 1: IEEE.

[136] H. Sun, Q. Guo, B. Zhang, W. Wu, and J. Tong, "Development and applications of system-wide automatic voltage control system in China," in *2009 IEEE Power & Energy Society General Meeting*, 2009, pp. 1-5: IEEE.

[137] T. J. Overbye, "A power flow measure for unsolvable cases," *IEEE Transactions on Power Systems,* vol. 9, no. 3, pp. 1359-1365, 1994.

[138] T. J. Overbye, "Computation of a practical method to restore power flow solvability," *IEEE Transactions on Power Systems,* vol. 10, no. 1, pp. 280-287, 1995.

[139] I. Dobson and L. Lu, "New methods for computing a closest saddle node bifurcation and worst case load power margin for voltage collapse," *IEEE Transactions on Power Systems,* vol. 8, no. 3, pp. 905-913, 1993.

[140] S. Granville, "Optimal reactive dispatch through interior point methods," *IEEE Transactions on Power Systems,* vol. 9, no. 1, pp. 136-146, 1994.

[141] Z. Feng, V. Ajjarapu, and D. J. Maratukulam, "A comprehensive approach for preventive and corrective control to mitigate voltage collapse," *IEEE Transactions on Power Systems,* vol. 15, no. 2, pp. 791-797, 2000.

[142] I. A. Hiskens, "Non-uniqueness in reverse time of hybrid system trajectories," in *International Workshop on Hybrid Systems: Computation and Control*, 2005, pp. 339-353: Springer.

[143] Y. Susuki and T. Hikihara, "Predicting voltage instability of power system via hybrid system reachability analysis," in *2007 American Control Conference*, 2007, pp. 4166-4171: IEEE.

[144] E. A. Cross and I. M. Mitchell, "Level set methods for computing reachable sets of systems with differential algebraic equation dynamics," in *2008 American Control Conference*, 2008, pp. 2260-2265: IEEE.

[145] N. A. S. Initiative, "SynchroPhasor Technology Fact Sheet," 2014.

[146] A. Meliopoulos, V. Madani, D. Novosel, and G. Cokkinides, "Synchrophasor Measurement Accuracy Characterization, North American SynchroPhasor Initiative Performance & Standards Task Team," ed.

[147] J. Zhao *et al.*, "Impact of Measurement Error on Synchrophasor Applications," 2015.

[148] S. Kincic, H. Zhang, B. Thomas, and D. Davies, "Bridging the gap between operation and planning in WECC-A step toward dynamic assessment of system limits," in *Power & Energy Society General Meeting, 2015 IEEE*, 2015, pp. 1-25: IEEE.

[149] R. Patel, T. Bhatti, and D. Kothari, "MATLAB/Simulink-based transient stability analysis of a multimachine power system," *International Journal of Electrical Engineering Education,* vol. 39, no. 4, pp. 320-336, 2002.

[150] J. Ballance, B. Bhargava, and G. Rodriguez, "Use of synchronized phasor measurement system for enhancing AC-DC power system transmission reliability and capability," *CIGRE C1-210 Session,* 2004.

[151] A. Chakrabortty and T. R. Khan, "Graph-theoretic model reduction of oscillation propagation in spatially distributed power system networks," in *Decision and Control (CDC), 2012 IEEE 51st Annual Conference on*, 2012, pp. 438-443: IEEE.

[152] Y. L. Yidan Lu, Gefei Kou, Kevin Tomsovic and Yilu Liu "Development of Reduced WECC and EI Models for Education and Research," presented at the 2015 CURENT Annual Site Visit, Knoxville, Tennessee, USA, Oct. 2015, 2015.

[153] H. Oh, "A new network reduction methodology for power system planning studies," *IEEE Transactions on Power Systems*, vol. 25, no. 2, pp. 677-684, 2010.

[154] X. Cheng and T. J. Overbye, "PTDF-based power system equivalents," *Power Systems, IEEE Transactions on,* vol. 20, no. 4, pp. 1868-1876, 2005.

[155] J. H. Chow, *Power System Coherency and Model Reduction*. Springer, 2013.

[156] X. Liu, J. Shen, A. Philip, E. Viray, M. Jiang, and D. Leon, "External WECC model reduction in on-line network applications for Alberta power grid," in *Power and Energy Society General Meeting (PES), 2013 IEEE*, 2013, pp. 1-5: IEEE.

[157] N.-P. Yu, C.-C. Liu, and J. Price, "Evaluation of market rules using a multi-agent system method," *Power Systems, IEEE Transactions on,* vol. 25, no. 1, pp. 470-479, 2010.

[158] J. E. Price, "Benchmarking a reduced test-bed model of WECC region for unit commitment and flexible dispatch," in *Power and Energy Society General Meeting (PES), 2013 IEEE,* 2013, pp. 1-5: IEEE.

[159] K. Mei, S. M. Rovnyak, and C.-M. Ong, "Clustering-based dynamic event location using wide-area phasor measurements," *IEEE Transactions on Power Systems,* vol. 23, no. 2, pp. 673-679, 2008.

[160] R. d. Janeiro, "DC Multi-Infeed Study," Electric Power Research InstituteTR-104586, 1994.

[161] S. Rovnyak, C. Taylor, and J. Thorp, "Real-time transient stability prediction–possibilities for on-line automatic database generation and classifier training," in *Second IFAC Symposium on Control of Power Plants and Power Systems, Cancun, Mexico,* 1995.

[162] C. Zheng, V. Malbasa, and M. Kezunovic, "Regression tree for stability margin prediction using synchrophasor measurements," *IEEE Transactions on Power Systems,* vol. 28, no. 2, pp. 1978-1987, 2013.

[163] R. Chakkapalli and P. Poonpun, " SYSTEM OPERATING LIMIT STUDY REPORT," CAISO, folsom, CAJanuary 31,2012 2012, Available: http://www.wecc.biz/library/WECC%20Documents/Seasonal%20System%20Operating%20Limits/2012%20Spring%20SOLs/Study%20Group%20Reports/CAMX/2012%20Spring%20OSS%20Report%20-%20final.pdf.

[164] C. S. o. t. M. S. a. R. A.-H. T. F. M. o. WECC, "Node-Breaker White Paper " WECC January 22 2014.

[165] S. Malik, M. Vaiman, and M. Vaiman, "Implementation of ROSE for real-time voltage stability analysis at WECC RC," in *2014 IEEE PES T&D Conference and Exposition*, 2014, pp. 1-5: IEEE.

[166] E. Moursi, M. Shawky, G. Joos, and C. Abbey, "A secondary voltage control strategy for transmission level interconnection of wind generation," *Power Electronics, IEEE Transactions on*, vol. 23, no. 3, pp. 1178-1190, 2008.

[167] P. Frias, T. Gómez, and D. Soler, "Voltage control and reactive power support in the Spanish transmission network," in *MELECON 2006-2006 IEEE Mediterranean Electrotechnical Conference*, 2006, pp. 916-919: IEEE.

[168] I. Jolliffe, *Principal component analysis*. Wiley Online Library, 2002.

[169] G. Hu and R. Zhang, "Multivariate Data Analysis Method: Pure Algebraic Treatment," *Press of Nankai University, Tianjin*, 1990.

[170] X. Yu and X. Ren, "Multivariate statistical analysis," ed: China Statistics Press, Beijing, 1999.

[171] O. Richardot, A. Viciu, Y. Besanger, N. Hadjsaid, and C. Kiény, "Coordinated voltage control in distribution networks using distributed generation," in *Transmission and Distribution Conference and Exhibition, 2005/2006 IEEE PES*, 2006, pp. 1196-1201: IEEE.

[172] J. Nocedal and S. Wright, *Numerical optimization*. Springer Science & Business Media, 2006.

[173] R. Fletcher, *Practical methods of optimization*. John Wiley & Sons, 2013.

[174] P. E. Gill, W. Murray, and M. H. Wright, "Practical optimization," 1981.

[175] M. Powell, "Variable metric methods for constrained optimization," in *Mathematical programming the state of the art*: Springer, 1983, pp. 288-311.

[176] W. Hock and K. Schittkowski, "A comparative performance evaluation of 27 nonlinear programming codes," *Computing*, vol. 30, no. 4, pp. 335-358, 1983.

[177] D. J. Higham and N. J. Higham, *MATLAB guide*. Siam, 2005.

[178] P. E. Gill, W. Murray, M. A. Saunders, and M. H. Wright, "Procedures for optimization problems with a mixture of bounds and general linear constraints," *ACM Transactions on Mathematical Software (TOMS)*, vol. 10, no. 3, pp. 282-298, 1984.

[179] P. E. Gill, W. Murray, and M. H. Wright, *Numerical linear algebra and optimization*. Addison-Wesley Redwood City, CA, 1991.

[180] S.-P. Han, "A globally convergent method for nonlinear programming," *Journal of optimization theory and applications*, vol. 22, no. 3, pp. 297-309, 1977.

[181] M. J. Powell, "A fast algorithm for nonlinearly constrained optimization calculations," in *Numerical analysis*: Springer, 1978, pp. 144-157.

[182] I. MathWorks, *MATLAB: the language of technical computing. Desktop tools and development environment, version 7*. MathWorks, 2005.

[183] S. Maslennikov, B. Wang, Q. Zhang, and E. Litvinov, "A test cases library for methods locating the sources of sustained oscillations," in *Power and Energy Society General Meeting (PESGM), 2016*, 2016, pp. 1-5: IEEE.

[184] WECC. (2016). *Maps of the Western Interconnection*. Available: https://www.wecc.biz/SystemStabilityPlanning/Pages/Maps.aspx

[185] J. M. Fogarty and R. M. LeClair, "Converting Existing Synchronous Generators into Synchronous Condensers," *Power Engineering*, vol. 115, no. 10, pp. 28-28, 2011.

[186] N. Miller, "Low Carbon Grid Study: Discussion of Dynamic Performance Limitations in WECC," GE Energy Consulting2015.

[187] B. Ray, "FACTS technology application to retire aging transmission assets and address voltage stability related reliability challenges in San Francisco Bay Area," in *Transmission and Distribution Conference and Exposition, 2003 IEEE PES*, 2003, vol. 3, pp. 1113-1120: IEEE.

[188] A. E. Fitzgerald, C. Kingsley, S. D. Umans, and B. James, *Electric machinery*. McGraw-Hill New York, 2003.

[189] P. Siemens, "PSS/E 33.0 Program Application Guide," ed: May, 2011.

[190] G. J. Dudgeon, W. E. Leithead, A. Dysko, J. O'Reilly, and J. R. McDonald, "The effective role of AVR and PSS in power systems: frequency response analysis," *IEEE Transactions on Power Systems*, vol. 22, no. 4, pp. 1986-1994, 2007.

[191] P. Siemens, "PSS/E Model Library of PSS/E-32," Schenectady, NY, USA2009.

[192] A. S. Bazanella and C. Conceicao, "Transient stability improvement through excitation control," *International Journal of Robust and Nonlinear Control*, vol. 14, no. 9-10, pp. 891-910, 2004.

[193] D. Kosterev and D. Davies, "System model validation studies in WECC," in *IEEE PES general meeting*, 2010.

[194] D. N. Kosterev, C. W. Taylor, and W. A. Mittelstadt, "Model validation for the August 10, 1996 WSCC system outage," *Power Systems, IEEE Transactions on*, vol. 14, no. 3, pp. 967-979, 1999.

[195] Z. Huang, P. Du, D. Kosterev, and S. Yang, "Generator dynamic model validation and parameter calibration using phasor measurements at the point of connection," *Power Systems, IEEE Transactions on*, vol. 28, no. 2, pp. 1939-1949, 2013.

[196] Z. Huang, P. Du, D. Kosterev, and B. Yang, "Application of extended Kalman filter techniques for dynamic model parameter calibration," in *Power & Energy Society General Meeting, 2009. PES'09. IEEE*, 2009, pp. 1-8: IEEE.

[197] Y. Lei, "Wide-Area Synchrophasor Measurement Applications and Power System Dynamic Modeling," 2015.

[198] A. J. Cavallo, "High-capacity factor wind energy systems," *Journal of Solar Energy Engineering*, vol. 117, no. 2, pp. 137-143, 1995.

[199] U. Kılıç and K. Ayan, "Optimal power flow solution of two-terminal HVDC systems using genetic algorithm," *Electrical Engineering*, vol. 96, no. 1, pp. 65-77, 2014.

[200] E. W. Kimbark, *Direct current transmission*. John Wiley & Sons, 1971.

[201] NERC, "Power System Model Validation-A White Paper by the NERC Model Validation Task Force of the Transmission Issues Subcommittee," in "A White Paper by the NERC Model Validation Task Force of the Transmission Issues Subcommittee," NERC, Princeton NJ2010, Available: http://www.nerc.com/docs/pc/mvwg/MV%20White%20Paper_Final.pdf.

[202] P. Siemens, "Pss/e 30.2 program operational manual," *Volume II*, 2005.

[203] S. Granville, J. Mello, and A. Melo, "Application of interior point methods to power flow unsolvability," *IEEE Transactions on Power Systems*, vol. 11, no. 2, pp. 1096-1103, 1996.

[204] A.-R. A. Khatib, "Internet-based Wide Area Measurement Applications in Deregulated Power Systems," Doctor of Philosophy, Electrical and Computer Engineering, Virginia Polytechnic and State University 2002.

[205] M. R. Khaldi, "Sensitivity Matrices for Reactive Power Dispatch and Voltage Control of Large-Scale Power Systems," presented at the World Scentific and Engineering Academy and Society International Conference on Power System and Electromagnetic Compatibility Izmir,Turkey, 2004.

[206] B. Stott, J. Jardim, and O. Alsaç, "DC power flow revisited," *IEEE Transactions on Power Systems*, vol. 24, no. 3, pp. 1290-1300, 2009.

[207] R. Zimmerman and C. Murillo-Sánchez, "MATPOWER 5.0 b1 User's Manual. 2014," ed.

Vita

Yidan Lu received the B.S. degree from Zhejiang University, Hangzhou, China, in 2011. He received the M.Ss degree in 2014 and Ph.D. degree in 2017 at the Center for Ultra-wide-area Resilient Electric Energy Transmission Networks (CURENT), the University of Tennessee, Knoxville, TN, USA, both in electrical engineering.